Numerical Investigation of Pressure Recovery in an Induced Draught Air-Cooled Condenser for CSP Application

by

Gerhard Muller Bekker

Thesis presented in partial fulfilment of the requirements for the degree of Master of Engineering (Mechanical) in the Faculty of Engineering at Stellenbosch University

Supervisor: Prof. C. J. Meyer
Co-supervisor: Prof. S. J. van der Spuy

December 2019

Declaration

By submitting this thesis electronically, I declare that the entirety of the work contained therein is my own, original work, that I am the sole author thereof (save to the extent explicitly otherwise stated), that reproduction and publication thereof by Stellenbosch University will not infringe any third party rights and that I have not previously in its entirety or in part submitted it for obtaining any qualification.

Date: 26/08/2019 .....

Abstract

Numerical Investigation of Pressure Recovery in an Induced Draught Air-Cooled Condenser for CSP Application

G. M. Bekker

Department of Mechanical and Mechatronic Engineering,
University of Stellenbosch,
Private Bag X1, Matieland 7602, South Africa.

Thesis: MEng (Mech)

December 2019

The operating flow rate and static efficiency of the axial flow fan in an induced draught air-cooled condenser are increased. It is achieved through pressure recovery, which is the conversion of the outlet dynamic pressure loss to static pressure. Stators and diffusers can recover pressure. Different outlet configurations were investigated for the M-fan of Wilkinson *et al.* (2017). The aim was to find an arrangement that yields high pressure recoveries at both design and off-design operating conditions. Discharge stators, conical diffusers, annular diffusers, and combinations of these were tested.

The open-source computational fluid dynamics code, OpenFOAM, was used to simulate the different outlet configurations for the 24 ft (7.3152 m) diameter M-fan. Stators were designed for the design flow rate using an isolated aerofoil approach. The stators were modelled as stationary fans using the extended actuator disc model of Van der Spuy (2011). A constant diffuser length of one fan diameter was used. Parametric studies were performed at the design flow rate of 333 m^3/s using fixed inlet velocity profiles. Various combinations of diffuser wall angles were simulated to find the diffuser geometry that yields the highest pressure recovery.

A stator alone achieved a pressure recovery coefficient of $K_{\mathrm{rec}} = 0.313$. A conical diffuser with an included angle of ten degrees ($2\theta = 10°$) produced $K_{\mathrm{rec}} = 0.647$. After adding a stator at the inlet of a conical diffuser of included angle $2\theta = 16°$, a recovery of $K_{\mathrm{rec}} = 0.837$ was achieved. Annular diffusers performed better. With a stator at the outlet of a 22° equiangular annular diffuser, $K_{\mathrm{rec}} = 0.951$ was reported. A diffuser with a stator at its inlet, a cylindrical hub, and a casing half-wall angle of 14° delivered $K_{\mathrm{rec}} = 1.125$. The highest pressure recovery coefficient was obtained with an equiangular annular diffuser with 22° wall angles measured from the axial direction, i.e. $K_{\mathrm{rec}} = 1.134$.

The discharge configurations that produced the above results were also simulated at off-design flow rates. The annular diffusers with and without a stator at their inlets performed similarly near the design flow rate. However, at low off-design flow rates, the diffuser without a stator performed better. The equiangular diffuser with 22° half-wall angles converted the highest portion of dynamic pressure to static pressure at design and off-design flow rates. At the design flow rate, this diffuser increased the fan static pressure from 114.7 to 155.7 Pa (35.7 % relative increase) and the fan static efficiency from 59.4 to 80.7 % (21.3 % absolute increase). Assuming a system curve of the form $\Delta p_{\mathrm{sys}} = a\dot{V}^2$, this annular diffuser increased the volume flow rate through the M-fan by 6.3 %. At this new operating point, the static efficiency was 20.0 % (absolute) higher than at the initial design point.

Uittreksel

Numeriese Ondersoek van Drukherwinning in 'n Geïnduseerde Lugverkoelde Kondensor vir Gekonsentreerde Sonkrag Toepassing

"Numerical Investigation of Pressure Recovery in an Induced Draught Air-Cooled Condenser for CSP Application"

G. M. Bekker

Departement Meganiese en Megatroniese Ingenieurswese,
Universiteit van Stellenbosch,
Privaatsak X1, Matieland 7602, Suid Afrika.

Tesis: MIng (Meg)

Desember 2019

Die lugvloeitempo deur en statiese doeltreffendheid van die aksiaalwaaier in 'n geïnduseerde lugverkoelde kondensor word verhoog. Dit word bereik deur drukherwinning, wat die omskakeling van die uitlaat dinamiese drukverlies na statiese druk is. Stators en diffusors kan druk herwin. Verskillende uitlaatkonfigurasies is ondersoek vir die M-waaier van Wilkinson *et al.* (2017). Die doel was om 'n uitlaatkonfigurasie te vind wat hoë drukherwinnings vir beide ontwerps- en buite-ontwerpsbedryfstoestande lewer. Uitlaat stators, koniese diffusors, annulêre diffusors, en kombinasies hiervan is getoets.

Die oopbron berekeningsvloeidinamika sagteware, OpenFOAM, is gebruik om die verskillende uitlaatkonfigurasies vir die 24 ft (7.3152 m) diameter M-waaier te simuleer. Stators is ontwerp vir die ontwerpsvloeitempo met behulp van 'n individuele-lemprofiel-benadering. Die stators is gemodelleer as stilstaande waaiers met die verlengde aksieskyf model van Van der Spuy (2011). 'n Konstante diffusorlengte van een waaier deursnee is gebruik. Parametriese studies is uitgevoer by die ontwerpsvloeitempo van 333 m^3/s deur gebruik te maak van

vaste inlaatsnelheidsprofiele. Verskeie kombinasies van diffusoropenigshoeke is gesimuleer om die diffusor hoek te vind wat die hoogste drukherwinning lewer.

'n Stator op sy eie het 'n drukherwinningskoëffisiënt van $K_{\text{rec}} = 0.313$ behaal. 'n Koniese diffusor met 'n openingshoek van tien grade ($2\theta = 10°$) het $K_{\text{rec}} = 0.647$ gelewer. Nadat 'n stator by die inlaat van 'n koniese diffusor met 'n openingshoek van $2\theta = 16°$ toegevoeg is, is 'n koëffisiënt van $K_{\text{rec}} = 0.837$ behaal. Annulêre diffusors het beter presteer. Met 'n stator by die uitlaat van 'n 22° gelykhoekige annulêre diffusor, is $K_{\text{rec}} = 0.951$ gerapporteer. 'n Diffusor met 'n stator by sy inlaat, 'n silindriese naaf en 'n buitewandhoek van 14° (gemeet van die aksiale rigting) het $K_{\text{rec}} = 1.125$ gelewer. Die hoogste drukherwinningskoëffisiënt is gelewer deur 'n gelykhoekige annulêre diffusor met halfmuurhoeke van 22°. Die gerapporteerde waarde was $K_{\text{rec}} = 1.134$.

Die uitlaatkonfigurasies wat die bogenoemde resultate gelewer het, is ook by buite-ontwerpsvloeitempo's gesimuleer. Die annulêre diffusors met en sonder 'n stator by hul inlate het soortgelyk presteer naby die ontwerpsvloeitempo. By lae buite-ontwerpsvloeitempo's het die diffusor sonder 'n stator egter beter presteer. Die gelykhoekige diffusor met 22° halfmuurhoeke het die meeste dinamiese druk omgesit in statiese druk by ontwerps- en buite-ontwerpsvloeitempo's. By die ontwerpsvloeitempo het hierdie diffusor die statiese druk van die waaier van 114.7 tot 155.7 Pa verhoog (35.7 % relatiewe toename). Die statiese doeltreffendheid van die waaier het van 59.4 na 80.7 % verhoog (21.3 % absolute toename). As 'n stelselkromme van die vorm $\Delta p_{\text{sys}} = a\dot{V}^2$ aangeneem word, het hierdie annulêre diffusor die volumevloeitempo deur die M-fan vermeerder met 6.3 %. By hierdie nuwe bedryfspunt was die statiese doeltreffendheid 20.0 % (absoluut) hoër as by die aanvanklike ontwerpspunt.

Acknowledgements

I would like to express my sincere appreciation to the following groups and individuals:

- My supervisors, Professors Meyer and Van der Spuy. Prof. Meyer, thank you for organising access to the Lengau Supercomputer at the Centre for High-Performance Computing (CHPC) and for getting me onto HPC1 at Stellenbosch University. My study would have looked entirely different if it was not for this. Prof. van der Spuy, thank you for being approachable and for making time for your students. Thanks for your advice on different topics, for believing in me, and for the financial support in my final year. It was tough at times, and you really helped me through it. Both Profs, thanks for affirming me closer to the end of the project. I felt a bit like I disappointed you at times, but in the end, you were happy, and I am grateful you communicated that to me.
- The Centre of Renewable and Sustainable Energy Studies (CRSES) for funding my first two years.
- The Solar Thermal Energy Research Group (STERG) for partially funding my final year. A special thanks to Dr Matti Lubkoll for motivating me to apply for the bursary, even though my situation was somewhat uncertain.
- STERG for creating a productive and homely working environment. A special thanks to Dr Matti Lubkoll for being super passionate about the research group and for trying (by leading by example) to establish a culture of excellence. Also, thanks to Leigh van der Merwe for looking after us and keeping the discipline in the office.
- Dr Ruan Engelbrecht for helping me with OpenFOAM in general and implementing your actuator disc model.
- The computations for preliminary runs and the validation study were performed using the University of Stellenbosch's HPC1 (Rhasatsha): `http://www.sun.ac.za/hpc`.

- The computations for the different M-fan outlet configurations were performed using the Lengau Cluster of the Centre for High-Performance Computing: `https://www.chpc.ac.za`.

Verder is daar 'n paar persoonlike bedankings wat ek sal wil maak:

- Mum en Paps: Ma het 'n onvoorwaardelike liefde vir Ma se familie en vriende. As ek dink aan 'n meer tasbare voorbeeld vir die *agape* liefde wat Jesus vir sy volgeling en Vader het, dink ek aan Ma. Ons besef nie altyd die gewig van wat Ma alles vir ons doen nie, maar dit stop Ma nie om daarmee aan te hou nie. Dit is wonderlik! Paps, ek het baie respek vir Pa. Pa is vir my 'n voorbeeld van wat dit beteken om 'n man te wees. Dankie vir die raad wat Pa my gegee het oor die jare deur die verskillende fases van volwassewording. Pa is my bron van wysheid op hierdie aarde. Pa en Ma is ons kinders se grootste ondersteuners. Dankie dat julle so dikwels ons belange bo julle s'n plaas. Ek is flippen lief vir julle.

- Die Maats: Dylan, Ruan, Burger, Jandré, Lieben en Christoph. Julle manne speel 'n merkwaardige rol in my. Die impak van julle vriendskap sal blywend wees. Met julle hulp kon ek van my grootste struikelblokke in die lewe oorkom. Ek hoop ons sal kan kontak hou in die jare wat kom.

- Hemelse Vader, Jesus Christus en Die Heilige Gees: Vader, ek moes U amper weer vind oor die verloop van my Meesters. Ek het 'n Fariseer geword wat akademies oor U praat en redeneer met ander gelowiges oor wat reg en verkeerd is. Maar, ek het vergeet hoe lief U my het. Ek het gedink ek is lief vir U, maar my lewe het nie gewys dat my wil is om U hart bly te maak nie. Dit was nie noodwendig lekker nie, maar dankie dat U dit vir my kom wys het. Dankie dat U steeds maar net altyd daar was vir my en U hand oor my gehou het. Ek wil sê ek is flippen lief vir U, maar ek wil eerder vra dat U my sal lei en help om te leer en verstaan wat dit regtig beteken. Dit is 'n reuse voorreg om U kind te kan wees. Dankie vir U genade.

Dedications

Pa en Ma

Vir al die opofferinge
en deurlopende ondersteuning

Train up a child in the way he should go;
even when he is old he will not depart from it.
Proverbs 22:6

Die Maats

Vir al die goeie tye saam;
julle het help vorm aan my karakter

As iron sharpens iron,
so one man sharpens another.
Proverbs 27:17

God Drie Enig

Dankie vir die bogenoemde

Every good and perfect gift
is from above, . . .
James 1:17

Contents

List of Figures

List of Tables

Nomenclature

Abbreviations

2-D	Two-dimensional
3-D	Three-dimensional
ACC	Air-cooled condenser
ASM	Algebraic stress model
ADM	Actuator disc model
BSL	Baseline
CFD	Computational fluid dynamics
CSP	Concentrated solar power
DNS	Direct numerical simulation
EADM	Extended actuator disc model
EASM	Explicit algebraic stress model
ERCOFTAC	European Research Community on Flow, Turbulence and Combustion
IGV	Inlet guide vane
LC	Lien *et al.*'s (1996) cubic
LES	Large eddy simulation
LRR	Launder, Reece and Rodi (1975)
LS	Low speed; Launder and Sharma (1974)
NASA	National Aeronautics and Space Administration
OGV	Outlet guide vane
OpenFOAM	Open source field operation and manipulation
PDE	Partial differential equation
RANS	Reynolds-averaged Navier-Stokes
RNG	Renormalized group
RSM	Reynolds-stress model
SIMPLE	Semi-implicit method for pressure-linked equations
SSG	Speziale, Sarkar and Gatski (1991)
SST	Shear stress transport

VLES	Very large eddy simulation	

Roman Symbols

A	Area	$[\mathrm{m}^2]$
ΔA	Annulus area, $A_\mathrm{C} - A_\mathrm{H}$	$[\mathrm{m}^2]$
a	Variable	$[-]$
a_{ij}	Reynolds-stress anisotropy tensor, $\overline{u_i' u_j'} - \frac{2}{3} k \delta_{ij}$	$[\mathrm{m}^2/\mathrm{s}^2]$
AR	Area ratio, $A_\mathrm{difo}/A_\mathrm{difi}$	$[-]$
C_1, C_2	Closure coefficients, 1.4 and 0.3, respectively	$[-]$
C_D	Drag coefficient	$[-]$
C_L	Lift coefficient	$[-]$
C_L, C_η	Closure coefficients, 0.23 and 70, respectively	$[-]$
$C_L\sigma$	Blade loading factor, $2(\epsilon_3 - \epsilon_4)\cos\alpha_\mathrm{m}$	$[-]$
C_p	Static pressure recovery coefficient, $\frac{\Delta p_\mathrm{s}}{\rho U_{z1}^2/2}$	$[-]$
C_p^*	Locus of maximum pressure recovery coefficient for a given non-dimensional length	$[-]$
C_p^{**}	Locus of maximum pressure recovery coefficient for a given area ratio	$[-]$
$C_{\gamma 1}, C_{\gamma 2}$	Universal closure coefficients	$[-]$
$C_{\varepsilon 1}$	Closure coefficient, $1.4[1 + 0.05(k/\overline{v'^2})^{1/2}]$	$[-]$
$C_{\varepsilon 2}$	Closure coefficient, 1.9	$[-]$
C_μ	Closure coefficient, k-ε: 0.09, $\overline{v'^2}$-f: 0.22	$[-]$
c_h	Blade chord length	$[\mathrm{m}]$
D	Drag force	$[\mathrm{N}]$
D_{ij}	Diffusion tensor	$[\mathrm{m}^2/\mathrm{s}^3]$
d	Diameter	$[\mathrm{m}]$
F_r	Radial force	$[\mathrm{N}]$
f	Elliptic damping fucntion	$[1/\mathrm{s}]$
G	Non-dimensional pressure gradient	$[-]$
H	Height	$[\mathrm{m}]$
i	i^th-index	$[-]$
K	Static pressure gain/loss coefficient, $\frac{\Delta p_s}{\rho U_A^2/2}$	$[-]$
k	Turbulent kinetic energy per unit mass, $\frac{1}{2}(\overline{u_x'^2} + \overline{u_y'^2} + \overline{u_z'^2})$	$[\mathrm{m}^2/\mathrm{s}^2]$
L	Lift force	$[\mathrm{N}]$
l	Length	$[\mathrm{m}]$
ℓ_t	Trubulent length scale	$[\mathrm{m}]$

$\dot{m}$	Mass flow rate	$[\mathrm{kg/s}]$
N	Rotational speed; number of cells	$[\mathrm{rpm}, -]$
$\mathbf{n}$	Surface normal vector	$[-]$
n_b	Number of blades	$[-]$
P	Power consumption; mean static pressure	$[\mathrm{W}, \mathrm{Pa}]$
P_{ij}	Turbulent kinetic energy production tensor, $-\left(\tau_{ik}\frac{\partial U_j}{\partial x_k} + \tau_{jk}\frac{\partial U_i}{\partial x_k}\right)$	$[\mathrm{m^2/s^3}]$
P_k	Turbulent kinertic energy production, $-\overline{u_i' u_j'}\frac{\partial U_i}{\partial x_j}$	$[\mathrm{m^2/s^3}]$
p	Pressure; instantanious static pressure	$[\mathrm{Pa}]$
Q	Torque	$[\mathrm{N\,m}]$
R	Pipe radius, gas constant	$[\mathrm{m}, \mathrm{J/(kg\,K)}]$
Re_{c_h}	Blade chord Reynolds number, $u_\mathrm{m} c_h/\nu$	$[-]$
Re_d	Conical diffuser Reynolds number, $U_z d/\nu$	$[-]$
$Re_{\Delta d}$	Annular diffuser Reynolds number, $2U_z\Delta r/\nu$	$[-]$
Re_t	Turbulence Reynolds number, $k^{1/2}\ell_t/\nu$	$[-]$
r	Radius	$[\mathrm{m}]$
Δr	Annulus width, $r_\mathrm{C} - r_\mathrm{H}$	$[\mathrm{m}]$
S	Swirl intensity, $\frac{\int_0^R u_z u_\theta r^2 \mathrm{d}r}{R\int_0^R u_z^2 r \mathrm{d}r}$; magnitude of mean strain-rate tensor, $\sqrt{S_{ij}S_{ji}}$	$[-, 1/\mathrm{s}]$
S_{ij}	Mean strain-rate tensor, $\frac{1}{2}\left(\frac{\partial U_i}{\partial x_j} + \frac{\partial U_j}{\partial x_i}\right)$	$[1/\mathrm{s}]$
S_ϕ, S_γ	Source terms of ϕ and γ, respectively	$[-]$
s_{ij}	Instantanious strain-rate tensor, $\frac{1}{2}\left(\frac{\partial u_i}{\partial x_j} + \frac{\partial u_j}{\partial x_i}\right)$	$[1/\mathrm{s}]$
T	Temperature; thrust	$[\mathrm{K}, \mathrm{N}]$
t	Time	$[\mathrm{s}]$
U	Average velocity, $\dot{V}/A$	$[\mathrm{m/s}]$
U, V, W	Mean velocities along, normal, and tangential to the wall	$[\mathrm{m/s}]$
$\mathbf{U}$	Mean velocity in vector notation	$[\mathrm{m/s}]$
U_0	Mean inlet velocity	$[\mathrm{m/s}]$
U_i	Mean velocity in tensor notation	$[\mathrm{m/s}]$
u	Velocity magnitude; instantanious velocity	$[\mathrm{m/s}]$
$\mathbf{u}$	Instantaneous velocity in vector notation	$[\mathrm{m/s}]$
u_i	Instantanions velocity in tensor notation	$[\mathrm{m/s}]$
u_x, u_y, u_z	Velocities in Cartesian coordinates	$[\mathrm{m/s}]$
u_r, u_θ, u_z	Velocities in cylindrical coordinates	$[\mathrm{m/s}]$

u_τ	Friction velocity, $\sqrt{\tau_\mathrm{w}/\rho}$	$[\mathrm{m/s}]$
V	Volume	$[\mathrm{m}^3]$
$\dot{V}$	Volume flow rate	$[\mathrm{m}^3/\mathrm{s}]$
$\overline{v'^2}$	Turbulent stress normal to streamlines	$[\mathrm{m}^2/\mathrm{s}^2]$
ϑ_t	Turbulent velocity scale	$[\mathrm{m/s}]$
x, y, z	Directions along, normal, and tangential to the wall	$[-]$
$\mathbf{x}$	Position vector in vector notation	$[\mathrm{m}]$
x_i	Position vector in tensor notation	$[\mathrm{m}]$
x_h	Hub ratio	$[-]$
y	Normal distance from the wall	$[\mathrm{m}]$
y^+	Sublayer-scaled normal distance from the wall, $u_\tau y/\nu$	$[-]$

Greek Symbols

α	Absolute flow angle; closure cofficient, 0.52	$[\mathrm{deg}, -]$
α_att	Angle of attack	$[\mathrm{deg}]$
α_e	Kinetic energy flux correction factor, $\frac{\iint_A \rho(\mathbf{u}\cdot\mathbf{n})u^2 \mathrm{d}A}{\dot{m}U_A^2}$	$[-]$
β_1, β^*	Closure coefficients, 0.075 and 0.09, repsectively	$[-]$
Γ	Diffusion coefficient	$[-]$
γ	Blade angle measured from tangential plane; turbulence variable	$[\mathrm{deg}, -]$
Δ	Differential; axial thickness of actuator disc	$[-, \mathrm{m}]$
δ	Increment of quantity	$[-]$
δ_{ij}	Kronecker delta, $\delta_{ij} = 1$ if $i = j$ and $\delta_{ij} = 0$ if $i \neq j$	$[-]$
ε	Turbulence dissipation per unit mass	$[\mathrm{m}^2/\mathrm{s}^3]$
ε_{ij}	Turbulence dissipation tensor, $2\nu\overline{s'_{ij}s'_{ji}}$	$[\mathrm{m}^2/\mathrm{s}^3]$
ϵ	Swirl coefficient, u_θ/u_z	$[-]$
η	Efficiency	$[-]$
θ	Diffuser wall angle measured from the axial direction, i.e. half-wall angle; ACC apex angle	$[\mathrm{deg}]$
μ	Molecular viscosity	$[\mathrm{kg/(m\,s)}]$
μ_t	Eddy viscosity	$[\mathrm{kg/(m\,s)}]$
ν	Kinematic molecular viscosity, μ/ρ	$[\mathrm{m}^2/\mathrm{s}]$
ν_t	Kinematic eddy viscosity, μ_t/ρ	$[\mathrm{m}^2/\mathrm{s}]$
ξ	Blade stagger angle measured from axial direction, $\alpha_\mathrm{m} - \alpha_\mathrm{att}$	$[\mathrm{deg}]$

Π_{ij}	Pressure-strain correlation tensor	$[-]$
ρ	Density	$[\mathrm{kg/m^3}]$
σ	Blade solidity, $n_b c_h/2\pi r$	$[-]$
σ, σ^*	Closure coefficients, 0.5 and 0.5, repsectively	$[-]$
σ_{ij}	Instantaneous viscous-stress tensor, $2\mu s_{ij}$	$[\mathrm{N/m^2}]$
$\sigma_k, \sigma_\varepsilon$	Closure coefficients, 1.0 and 1.3, respectively	$[-]$
τ_{ij}	Specific Reynolds-stress tensor, $-\overline{u_i' u_j'}$	$[\mathrm{m^2/s^2}]$
τ_t	Turbulent time scale	$[\mathrm{s}]$
Φ	Mean arbitrary flow variable	$[-]$
ϕ	Instantaneous arbitrary flow variable	$[-]$
ω	Turbulent specific dissipation rate	$[1/\mathrm{s}]$

Subscripts

1	Upstream of fan rotor
2	Downstream of fan rotor
3	Upstream of stator
4	Downstream of stator
∞	Property of the far field; atmospheric conditions
A	Cross-sectional area
a	Air
C	Casing (outer walls)
d	Dynamic
des	Design point
dif	Diffuser
do	Downstream
dump	Dump (to represent the open atmosphere)
equiv	Equivalent
F	Fan
FC	Fan casing
F/dif	Fan-diffuser unit
FH	Fan hub
fr	Frontal
H	Hub (inner walls)
heθ	Inclined heat exchanger
hom	Homogeneous
i	Inlet
i	i^{th}-index

id	Ideal
m	Mean
max	Maximum
OGV	Outlet guide vane (or stator)
o	Outlet
op	Operating point
pl	Plenum chamber
r, θ, z	Cylindrical coordinate directions
rec	Recovery of dynamic to static pressure
root	Blade root
s	Static
stream	Streamline
sys	System
t	Total
ts	Tower support
up	Upstream
w	Wall
x, y, z	Cartesian coordinate directions
ϕ	Pertaining to arbitrary flow variable

Superscripts

$\bar{}$	Averaged quantity
$'$	Fluctuating quantity

Chapter 1

Introduction

1.1 Background

Concentrated solar power (CSP) plants are typically located in sunny, arid areas where the availability of water for wet-cooling systems is limited. Kröger (1994) predicted that diminishing cooling water supplies coupled with increased water costs, environmental considerations, and restrictive legislation would result in an increased reliance on ambient air as cooling medium. Despite air's poor cooling properties, it is always available, has no procurement costs, no disposal issues, nor significant impacts on the environment (Kröger, 1998).

Condensers that employ ambient air as a cooling medium are termed air-cooled condensers (ACCs). Moore *et al.* (2014) claim that ACCs can potentially reduce the water usage of a power plant by as much as 90 %. This reduction is especially significant for CSP plants. Moore *et al.* (2014) state that ACCs are in many cases the only feasible option for CSP application.

Air-cooled condensers are categorised in two broad categories that are based on the method used to create the required draught through the heat exchanger bundles. They are natural draught ACCs, where buoyancy effects are responsible for the induced draught through the bundles, and mechanical draught ACCs, where fans create the draught.

Mechanical draught ACCs most often employ axial flow fans since they generally require a relatively low pressure rise at a relatively high volume flow rate at operating conditions. Mechanical draught ACCs are subdivided into two categories: forced and induced draught ACCs. In the forced draught configuration, the fan creates a high pressure within the ACC, forcing air through the heat exchanger bundles. In the induced draught configuration, the fan creates a low pressure within the ACC to draw air through the heat exchanger bundles.

In a forced draught ACC, the fans are installed in the cooler inlet air stream below the finned tube condenser bundles. Kröger (1998: 1.2.1) explains that this results in lower fan power consumption for a given mass flow rate and lower fan blade temperature exposure compared to an induced draught configuration. Forced draught ACCs are also easier to maintain. As a result, the majority of ACCs are of the forced draught construction (Hall, 2012: 51).

Despite the disadvantages associated with induced draught ACCs, Monroe (1978) believes that they are more advantageous than forced draught systems. Induced draught ACCs provide a more uniform airflow distribution through the finned tube bundles than in forced draught ACCs. The higher discharge velocities associated with induced draught systems make them less susceptible to hot-plume recirculation and less sensitive to crosswinds. The heat exchangers are also not as exposed to the atmosphere as in forced draught systems, making them less sensitive to wind, solar radiation, and hailstorms. Hall (2012: 51) adds that the natural draught stack effect in induced draught systems is greater, making them more tolerant to fan-failures. According to Enexio (no date), lower overall plant heights are possible for induced draught systems. This reduces their visual impact, structural weight, construction periods, and capital investment costs.

Ultimately, the decision of using either a forced or induced draught configuration depends on the operating temperatures, fan accessibility, process specifications, ambient conditions, fouling, and other practical considerations (Kröger, 1998). The current study focusses on the induced draught construction.

1.2 Motivation

According to Moore *et al.* (2014), the high operating costs and reduced plant efficiencies associated with ACCs render them unattractive. There is a need for more efficient dry-cooling systems for CSP application. In the design of an effective ACC, Monroe (1978) and Kröger (1994) emphasise the importance of taking the entire fan system into account when computing the fan system efficiency. It will inevitably be lower than the efficiency reported under ideal and reproducible conditions.

While the high discharge velocities associated with induced draught ACCs aid in the avoidance of hot-plume recirculation and reduce sensitivity to wind effects, the kinetic energy at the fan exit that dissipates into the atmosphere is substantial. This wasted energy is seen as a loss by the fan system, reducing the fan total-to-static efficiency. An exhaust diffuser or a stator, or both, can be installed in an attempt to recover a portion of the lost kinetic energy at the outlet plane of the ACC. Walter *et al.* (2018) show that this will indeed increase the static efficiency of the fan system.

1.3 Research Objective

The current study investigates the potential for increasing the total-to-static efficiency of the fan system employed in an induced draught ACC by reducing the outlet kinetic energy loss. This reduction is achieved by a process termed pressure recovery, which is the conversion of kinetic energy to pressure energy. Pressure recovery also shifts the operating point to a higher volume flow rate, which allows for increased heat removal rates.

The fan under consideration in this study is the M-fan that was designed by Wilkinson (2017). Various fan discharge configurations were tested by means of numerical analysis. The investigation includes different conical and annular diffusers fitted with or without stators. The stators were either located between the fan exit and diffuser inlet, or at the diffuser outlet. The outcome of the study will indicate which outlet configuration produces the highest pressure recovery for the M-fan at both design and off-design conditions. It will also reveal how pressure recovery affects the operating point of the fan in terms of efficiency and volumetric flow rate.

1.4 Thesis Outline

The study commences with a literature review in Chapter 2 that provides research and insight into ACCs, axial flow fans, diffusers, and stators. Research on modelling strategies for flows in adverse pressure gradients and flows involving turbomachinery blading are also provided. Chapter 3 outlines an analytical investigation aimed at quantifying the potential gains in fan performance when minimising the outlet kinetic energy loss. It serves to identify the major contributing factors in pressure recovery. Details of numerical modelling strategies for blading, turbulence, and near-wall flows are given in Chapter 4.

Since experimental data are not available for validation purposes, a validation study on a similar test case was conducted prior to the M-fan simulations. The details of the validation study are outlined in Chapter 5. Chapter 6 presents the detailed numerical analysis of various outlet configurations for the M-fan. Parametric studies were conducted to find the configurations that provide the highest pressure recoveries at the design flow rate. The different configurations were then compared at off-design flow rates to see which configuration performs the best globally. These data were used to construct fan-diffuser characteristic curves. They illustrate how the operating point is affected by pressure recovery. Conclusions and recommendations are contained in the final chapter, Chapter 7.

Chapter 2

Literature Review

2.1 Introduction

This chapter covers literature that pertains to the current research project. It starts by providing background information on the design methodology that was followed to design the particular fan of interest, i.e. the M-fan. Thereafter, the concept of pressure recovery (or kinetic energy recovery) is introduced and its relevance to axial flow fans is made apparent. It is followed by sections that cover the two main methods of achieving pressure recovery, i.e. diffusion through diffusers or stators. Since the current project is a numerical investigation, the final section is dedicated to aspects of the modelling of flow in diffusers and stators. It includes the modelling of turbulence and near-wall treatment methods in diffusing flows as well as the modelling of turbomachinery blading. The main findings are summarised in the concluding section.

2.2 Axial Flow Fans in Air-Cooled Condensers

As outlined in Chapter 1, air-cooled condensers (ACCs) can be used instead of wet-cooling systems to save water in the condensing process of a steam power plant. ACCs typically employ axial flow fans since they require relatively high volume flow rates and low pressure rises at operating conditions. Bruneau (1994) developed an axial flow fan design methodology for ACC application. However, Wilkinson *et al.* (2017) claim that his method produces excessive chord lengths and blade twists at the hub when applied to modern ACC fans. That is because modern ACCs operate at higher flow rates with lower pressure rise requirements.

An article by Von Backström *et al.* (1996) describes the minimisation of the exit kinetic energy loss of an axial flow fan by optimising the outlet velocity distribution. Although they only managed to decrease the outlet kinetic energy

flux by 1.8 % compared to free-vortex fans, Van der Spuy (1997: 7) noticed that the resulting exit velocity distribution could lead to a 50 % reduction in blade twist. Wilkinson *et al.* (2017), therefore, adopted this method to calculate the outlet velocity distribution of the M-fan in order to alleviate the problem of excessive blade twist at the hub.

2.3 Pressure Recovery

Monroe (1978) explains that the total pressure delivered by an axial flow fan comprises of two components: the static pressure that works against the sum of the system losses, and the dynamic (or velocity) pressure that is a loss associated with accelerating the stagnant surrounding air to the design velocity. Walter *et al.* (2018) theoretically estimated the static efficiency increase of an axial flow fan when reducing the dynamic pressure loss. They compared the performance of three discharge configurations at a typical design point. These included a rotor-only unit, a rotor-stator unit, and a rotor-stator unit fitted with an annular exhaust diffuser. The diffuser length was equal to the fan diameter.

A stator eliminates the circumferential component of the dynamic pressure loss. A diffuser reduces the axial and circumferential components of the dynamic pressure loss. That is because, in an expanding duct, the conservation of mass and angular momentum dictate the reduction in axial and circumferential velocity, respectively. Walter *et al.*'s (2018) study reveals that the fan unit benefits considerably from the addition of a stator and a diffuser. The efficiency ratio, $\eta_{\mathrm{Fs}}/\eta_{\mathrm{Ft}}$, at the selected design point is 7 % higher for the rotor-stator unit compared to the rotor-only unit. Adding an annular diffuser to the rotor-stator unit increases the efficiency ratio by a further 20 %. The static efficiency of the rotor-only unit can, therefore, be increased by 27 % at this particular design point.

2.4 Diffusers

A subsonic diffuser is a geometrically simple device, i.e. an expanding duct. Its purpose is to convert dynamic pressure to static pressure—a process termed static pressure recovery. An effective diffuser converts a high percentage of kinetic energy to pressure energy within a given length or area ratio (Blevins, 1984: 144). The adverse pressure gradient in a diffuser decelerates the flow, which thickens the boundary layer. If the pressure gradient is excessive, the flow will separate from the walls, reducing the effective flow area in the diffuser. This is known as diffuser stall and is usually associated with reduced performance. Therefore, although a seemingly simple flow device, the length and expansion angle of a diffuser should be selected with care: A divergence angle that is too

shallow for a specified area ratio will result in a lengthy unit with high skin friction losses; an excessive divergence angle will result in even greater losses due to diffuser stall (Dixon and Hall, 2014: 271–272).

Wallis (1983: 89–90) provides charts with recommended included angles for two-dimensional, conical, and annular diffusers with converging or diverging hubs. The conical diffuser data were collected from McDonald and Fox (1966) and the annular diffuser data from Wallis (1975) and Shepherd (1974), respectively. No tailpipe was present in any of these experimental studies. A tailpipe is a cylindrical extension that can be added to the outlet of a diffuser to facilitate large scale mixing. It improves the uniformity of the discharge velocity profile distribution, which increases pressure recovery (Miller, 1978).

2.4.1 Diffuser performance evaluation

Sovran and Klomp (1967: 274–276) explain the difficulties associated with measuring diffuser performance, especially in the presence of swirl. Usually, diffuser performance is associated with static pressure recovery. A relative measure of the pressure producing capability of a diffuser is to compare the measured pressure rise with an "ideal" pressure rise. Assuming a zero total pressure loss, Blevins (1984: 144) shows that the ideal diffuser pressure rise for non-uniform axial inlet flow is given by

$$\left.\frac{p_{\mathrm{so,id}} - p_{\mathrm{si}}}{\rho U_{z\mathrm{i}}^2/2}\right|_{\text{non-uniform}} = \alpha_{e\mathrm{i}} - \alpha_{e\mathrm{o}}\left(\frac{A_{\mathrm{i}}}{A_{\mathrm{o}}}\right)^2, \tag{2.1}$$

where p_{s} is static pressure, ρ is density, U_z is the mean axial velocity, α_e is the kinetic energy correction factor, and A denotes cross-sectional area. The "i" and "o" subscripts refer to inlet and outlet conditions, respectively, and "id" denotes ideal conditions.

Sovran and Klomp (1967: 275) argue that this non-uniform definition for diffuser performance is inconvenient since it requires information about the inlet and outlet velocity profiles. Therefore, a more convenient, yet less meaningful, pressure recovery coefficient is defined based on uniform axial flow conditions. It relates the actual pressure rise to the highest possible pressure rise, viz.,

$$C_p = \frac{p_{\mathrm{so}} - p_{\mathrm{si}}}{\rho U_{z\mathrm{i}}^2/2}. \tag{2.2}$$

The overall diffuser effectiveness relates the actual pressure rise to the pressure rise achievable from the same geometry at the same flow rate while assuming ideal uniform flow conditions, viz.,

$$\eta_{\mathrm{dif}} = \frac{p_{\mathrm{so}} - p_{\mathrm{si}}}{p_{\mathrm{so,id}} - p_{\mathrm{si}}} = \frac{(p_{\mathrm{so}} - p_{\mathrm{si}})/(\rho U_{z\mathrm{i}}^2/2)}{(p_{\mathrm{so,id}} - p_{\mathrm{si}})/(\rho U_{z\mathrm{i}}^2/2)} = \frac{C_p}{C_{p,\mathrm{id}}}. \tag{2.3}$$

The ideal pressure recovery coefficient is the same as Eq. (2.1), but for uniform flow (i.e., $\alpha_{ei} = \alpha_{eo} = 1$):

$$C_{p,\mathrm{id}} = 1 - (A_\mathrm{i}/A_\mathrm{o})^2. \tag{2.4}$$

In practice, C_p and η_dif will generally be smaller than $C_{p,\mathrm{id}}$ and unity, respectively. However, if the inlet velocity profile is peaked and the outlet profile nearly uniform, it is possible for C_p to exceed the ideal value and η_dif to exceed unity (Sovran and Klomp, 1967: 276; Blevins, 1984: 148).

According to Wallis (1983: 91), diffuser effectiveness data above 0.90 for two-dimensional, conical, and annular diffusers with thin inlet boundary layers and no tailpipes have been reported—near the theoretical maximum of 0.94. For thick inlet boundary layers, peak effectiveness is normally higher than 0.80. Flow asymmetry or non-uniformity will reduce the performance further. Wallis (1983: 92) and Eck (1973: 277) recommend using a conservative diffuser effectiveness of 0.80 for diffusers with symmetrical inlet flow conditions and near-optimum geometries. However, Kröger (1998: 6.4.9) states that since the velocity distributions at the fan and diffuser outlets are not uniform, this estimate can only give approximate performance characteristics. If possible, the fan and diffuser should be tested together to obtain fan-diffuser performance characteristics that are fit for design purposes.

Diffuser performance is generally a function of its geometry, Reynolds number, and flow conditions at the inlet and outlet. Of these, diffuser geometry has the most significant impact on performance (Blevins, 1984: 149–151). Sovran and Klomp (1967: 291) compared the optimum performance lines for annular, conical, and two-dimensional diffusers. They found that the area ratio and non-dimensional length are the dominant factors influencing optimum diffuser geometry, regardless of diffuser type.

Even though it is often impractical to account for non-uniform effects, Sovran and Klomp (1967: 292–293) concede that the performance of optimum or near-optimum diffuser geometries is heavily influenced by it. They adopted the definition of mass-averaged total pressure to predict diffuser performance for non-uniform flow. Substituting

$$p_\mathrm{so} - p_\mathrm{si} = \left(\alpha_{ei}\rho U_{z\mathrm{i}}^2/2 - \alpha_{eo}\rho U_{z\mathrm{o}}^2/2\right) - (p_\mathrm{ti} - p_\mathrm{to}) \tag{2.5}$$

into Eq. (2.3) and simplifying yields

$$\eta_\mathrm{dif} = \frac{\alpha_{ei} - \alpha_{eo}(A_\mathrm{i}/A_\mathrm{o})^2}{1 - (A_\mathrm{i}/A_\mathrm{o})^2} - \frac{K_\mathrm{dif}}{1 - (A_\mathrm{i}/A_\mathrm{o})^2}, \tag{2.6}$$

where the diffuser loss coefficient is defined as

$$K_\mathrm{dif} = \frac{p_\mathrm{ti} - p_\mathrm{to}}{\rho U_{z\mathrm{i}}^2/2}. \tag{2.7}$$

Equation (2.6) illustrates that effectiveness values can decrease as a result of distortion of the velocity profile (i.e., $\alpha_{eo} > \alpha_{ei}$) or losses (i.e., $K_{\text{dif}} > 0$). According to Sovran and Klomp (1967: 293–296), the first term in Eq. (2.6) represents the reduction in effectiveness due to *insufficient* diffusion, whereas the second term represents losses due to viscous effects, hence *inefficient* diffusion. They showed that diffuser effectiveness primarily decreases due to velocity profile distortions. They thus concluded that the problem with most diffusers is insufficient rather than inefficient diffusion.

With the importance of the velocity profile made apparent, Sovran and Klomp (1967: 296) continue to explain the reason for profile distortion encountered in diffusers: The pressure and velocity changes along any streamline of an incompressible flow are related by

$$\mathrm{d}u_{\text{stream}} = \frac{(\mathrm{d}p_{\text{t}} - \mathrm{d}p_{\text{s}})}{\rho u_{\text{stream}}}. \tag{2.8}$$

In the absence of losses (i.e., $\mathrm{d}p_{\text{t}} = 0$), this equation indicates that the change in velocity along a streamline is inversely proportional to the local velocity. In diffusing flows (i.e., $\mathrm{d}p_{\text{s}} > 0$), the velocity will decrease and it will decrease more in areas where the local velocity is low. Velocity differences will thus increase in the flow direction, distorting the velocity profile. Miller (1978: 36) confirms this. He states that the velocity near the walls rapidly decreases at the initial sections of the diffuser, while the core flow is essentially unaffected.

Peters (1934) states that the uniform definitions for diffuser performance given by Eqs. (2.2) to (2.4) are inadequate for arbitrary kinetic energy distributions. Since the purpose of a diffuser is to convert kinetic energy into potential energy, he defined a mass-averaged efficiency giving the ratio of actual pressure energy rise to kinetic energy decline, viz.,

$$\bar{\eta}_{\text{dif}} = \frac{1/A_{\text{o}} \iint p_{\text{so}} u_{z\text{o}} \,\mathrm{d}A_{\text{o}} - 1/A_{\text{i}} \iint p_{\text{si}} u_{z\text{i}} \,\mathrm{d}A_{\text{i}}}{\frac{1}{2}\rho\big[1/A_{\text{i}} \iint u_{\text{i}}^2 u_{z\text{i}} \,\mathrm{d}A_{\text{i}} - 1/A_{\text{o}} \iint u_{\text{o}}^2 u_{z\text{o}} \,\mathrm{d}A_{\text{o}}\big]}, \tag{2.9}$$

where u is the velocity magnitude. McDonald *et al.* (1971) followed the same rationale to formulate an area-averaged definition for diffuser performance with swirling (or non-uniform) inlet flow, viz.,

$$\overline{C_p} = \frac{1/A_{\text{o}} \iint p_{\text{so}} \,\mathrm{d}A_{\text{o}} - 1/A_{\text{i}} \iint p_{\text{si}} \,\mathrm{d}A_{\text{i}}}{\frac{1}{2}\rho(1/A_{\text{i}}) \iint u_{\text{i}}^2 \,\mathrm{d}A_{\text{i}}}. \tag{2.10}$$

Note that the denominators in Eqs. (2.9) and (2.10) include the kinetic energy contained in both the swirling and axial components.

2.4.2 Conical diffusers

The performance of a conical diffuser is a function of its geometry, Reynolds number, and the inlet and outlet velocity profiles. The data of Miller (1978)

suggest that pressure recoveries with thick inlet boundary layers are five to 15 % lower compared to thin inlet boundary layers. Similarly, diffuser performance declines with decreasing Reynolds number (due to increased boundary layer thickness). McDonald and Fox (1966) found that for inlet Reynolds numbers above 7.5×10^4 the inlet boundary layer becomes fully turbulent. Diffuser performance then becomes independent of Reynolds number.

A performance chart for conical diffusers with free discharges is given in Fig. 2.1. The area ratio is equal to the diffuser outlet area over its inlet area, or $AR = (d_o/d_i)^2$. The length ratio is equal to the diffuser length, l_{dif}, divided by its inlet radius, r_i. The dashed C_p^*-line represents the locus of points that coincide with the area ratios producing the maximum static pressure recovery for a given non-dimensional length; the C_p^{**}-line represents the locus of points that coincide with the non-dimensional length producing the maximum static pressure recovery for a given area ratio.

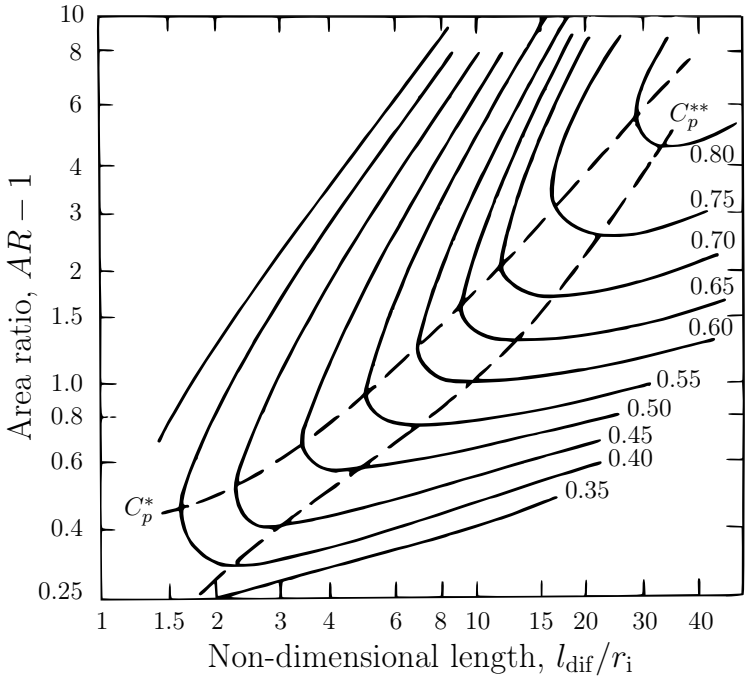

Figure 2.1: Static pressure recovery coefficient for conical diffusers with a thin inlet boundary layer and $Re_{d_i} > 7.5 \times 10^4$ (McDonald and Fox, 1966)

According to Miller (1978: 41), diffusers that fall in the region to the right of the C_p^{**}-line are stable, but unnecessary long. Above the C_p^*-line, steady-state stall develops and diffuser performance is poor. Most practical diffusers are within the region between the C_p^* and C_p^{**} lines. Here the outlet flow distribution becomes very non-uniform with areas of stall and pressure fluctuations. Wallis (1983: 86) also states that diffusers designed for maximum pressure recovery within a given length are characterised by a small degree of periodic separation.

However, McDonald and Fox (1966) and Blevins (1984: 151) state that this is only true for two-dimensional diffusers. McDonald and Fox (1966) showed that the C_p^*-line always lies above the line of first appreciable stall for two-dimensional diffusers. This means that a degree of stall will be present in optimum two-dimensional diffusers. For conical diffusers, however, they found that the C_p^*-line lies below the line of first appreciable stall. Optimum conical diffusers will thus be stable and free from stall.

According to Kröger (1998: 6.4.9), a practical conical diffuser downstream of an axial flow fan usually lies within the $12^\circ \leq 2\theta \leq 17^\circ$ range. Eck (1973: 279) argues that it is impossible to state exact rules for diffusion angles. Half-angles may vary as wide as 5° to 20° depending on the Reynolds number and turbulence quantities, even though the narrower range of 7° to 9° is often envisaged.

2.4.3 Annular diffusers

Four parameters are required to describe the geometry of a straight-walled annular diffuser: inner and outer wall angles, inlet radius ratio, and non-dimensional length. Two more parameters are thus required than in the case of conical diffusers. This complicates the generalisation of performance characteristics for annular diffusers.

Sovran and Klomp (1967: 285) experimented with over a hundred diffuser geometries in search of optimum-geometry lines that are useful for design application. The experiments were conducted at low Mach numbers, high Reynolds numbers, and with thin turbulent inlet boundary layers. They performed all experiments with non-swirling inlet conditions and free discharge outlet conditions.

In an attempt to find C_p^* and C_p^{**} lines for annular diffusers, Sovran and Klomp (1967: 286–287) plotted pressure recovery versus area ratio at fixed non-dimensional lengths, and pressure recovery versus non-dimensional length at fixed area ratios. Combining the results, they generated the performance chart shown in Fig. 2.2. The area ratio is given by

$$AR = \left(r_{\mathrm{Co}}^2 - r_{\mathrm{Ho}}^2\right) / \left(r_{\mathrm{Ci}}^2 - r_{\mathrm{Hi}}^2\right), \tag{2.11}$$

where r_{C} is the radius to the outer casing wall and r_{H} is the radius to the inner hub wall. The length ratio is equal to the diffuser length, l_{dif}, divided by the annular width at the diffuser inlet, i.e. $\Delta r_{\mathrm{i}} = r_{\mathrm{Ci}} - r_{\mathrm{Hi}}$. From the experiments, they observed that the optimum geometry at fixed wall length (i.e., the C_p^*-line) is essentially independent of the combination of wall angles and inlet radius ratio. Subsequently, they concluded that the performance of annular diffusers of widely differing geometries could be expressed in terms of a length and area ratio.

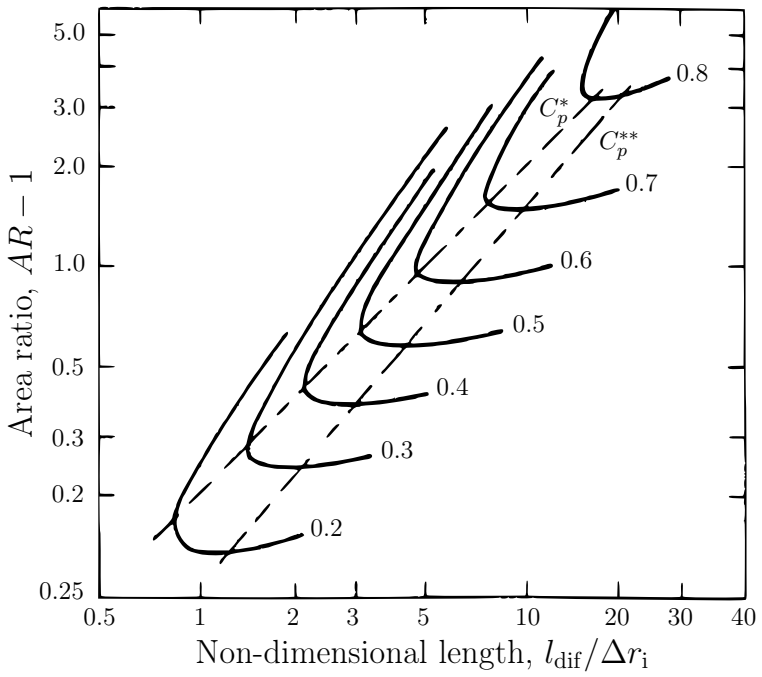

Figure 2.2: Static pressure recovery coefficient for annular diffusers with a thin inlet boundary layer and $Re_{\Delta d} = 6.0 \times 10^5$ (Sovran and Klomp, 1967: 289)

However, Wallis (1975) established that the optimum design solution of Sovran and Klomp (1967) does not cover all annular diffuser geometries. Russell and Wallis (1969) found that inner, rather than outer, wall geometry plays a more significant role in diffuser performance. Subsequently, Kneen (1970) and Wallis (1975) tested multiple centre bodies with conical and cylindrical sections. There was no substantial difference in diffuser performance between the different conical hub geometries and whether they were streamlined or not. However, performance dropped sharply when no centre body was present. Reverse flow persisted for about a single duct diameter downstream of the bluff termination, resulting in unsteady diffuser flow due to large-scale turbulence at the diffuser inlet. A centre body thus generally improves diffuser performance. The problem of centre body separation, however, remained unsolved.

In an attempted to transport momentum towards the centre body, Wallis (1975) tested swirl vanes and a ring aerofoil. The swirl vanes were relatively ineffective. The ring aerofoil suppressed flow separation from the inner and outer walls, but separation from the ring aerofoil itself resulted in poor performance. Promising, but limited, results were obtained using expanding centre bodies. Therefore, Shepherd (1974) did a continuation of this work, focussing on expanding centre bodies. He experimentally studied the effects of different wall angle combinations on the performance of divergent centre body annular diffusers downstream of an axial flow fan. In exhaust application, he found that divergent centre bodies yield shorter diffusers than convergent centre bodies for a specified

performance. Moreover, diffusers with divergent centre bodies are less sensitive to the adverse effects of inlet swirl.

Shepherd (1974) postulated that there is an analogous conical diffuser for any annular diffuser that would suffer the same losses with equivalent inlet conditions. They are considered analogous if their area ratios are equal and their wall angles are related by

$$\tan\theta = \frac{\tan\theta_{\mathrm{C}} - x_h \tan\theta_{\mathrm{H}}}{1 + x_h}, \tag{2.12}$$

where θ is the half-wall angle of the conical diffuser (i.e., the angle measured from the axial), θ_{H} and θ_{C} are the inner hub and outer casing half-wall angles of the annular diffuser, and x_h is the inlet radius ratio of the annular diffuser.

For a given performance, the area ratio that corresponds to a specified length ratio can be selected from conical diffuser performance charts (as contained in Fig. 2.1). With the area and length ratios known, provided that inlet swirl is moderate, Shepherd (1974) demonstrated that the wall angle combination that will yield the shortest annular diffuser for the specified performance is given by

$$\tan\theta_{\mathrm{C}} = \frac{\sqrt{AR} - 1}{l_{\mathrm{dif}}/r_{\mathrm{Ci}}}, \tag{2.13a}$$

$$\tan\theta_{\mathrm{H}} = x_h \tan\theta_{\mathrm{C}}. \tag{2.13b}$$

Adkins (1983) had a similar idea to correlate data for optimal conical diffusers to annular diffusers. He achieved this using a non-dimensional pressure gradient correlating parameter, G. He postulated that an annular diffuser with the same values of G along its length as the optimal conical diffuser of the same area ratio would also be optimised to produce the maximum pressure recovery within the available length. Such annular diffusers will generally have at least one curved wall. Sherras (1980) performed experiments on two sets of annular diffusers with constant inlet radius ratios and cylindrical centre bodies. Each set had three diffusers: one designed following Adkins (1983), and the others had slightly smaller and larger area ratios, respectively. For both sets, the Adkins (1983) diffuser gave the highest pressure recovery.

Since there are relatively little design data for annular diffusers, Miller (1978: 174) advocates the use of conical diffuser data, provided that the divergence angle from the axial is smaller than 20°. The non-dimensional length for conical diffusers, $l_{\mathrm{dif}}/r_{\mathrm{i}}$, should then be replaced by the non-dimensional length for annular diffusers, $l_{\mathrm{dif}}/\Delta r_{\mathrm{i}}$, (see Figs. 2.1 and 2.2). Note that optimal annular diffusers are generally stable and free from stall (Blevins, 1984: 153).

2.4.4 Inlet flow distortion

Inlet flow conditions greatly influence diffuser performance. After Russell and Wallis (1969) established that the hub geometry is more important than the casing geometry, Wright *et al.* (1970) found that annular diffuser performance is even more sensitive to inlet flow conditions. Johnston (1953) reported that flow non-uniformity and asymmetry at the inlet of annular diffusers decrease its performance, especially those with larger wall angles.

Hill *et al.* (1963) found that pressure gradients heavily influence the decay of wakes produced by flow obstructions: The wake-type distortions caused by upstream blading or struts could lead to diffuser stall if the pressure gradient is large enough. Raj and Lakshminarayana (1973) found that flow properties across the wake downstream of a cascade of aerofoils were asymmetrical up to three-quarters of the chord length. Sufficient axial clearance is, therefore, required between upstream blading and a diffuser.

2.4.5 Inlet swirl effects

Rotational flow at the inlet of a diffuser can be beneficial for its performance (Wallis, 1983: 106). The swirling flow will be accompanied by outward radial flow due to a radial pressure imbalance. The radial flow increases the axial velocity near the diffuser wall due to mass conservation. This energises the near-wall flow, which suppresses flow separation. Consequently, swirling flows can accommodate larger divergence angles. According to Miller (1971: 84), wide-angled diffusers with free discharge outlet conditions having half-wall angles larger than six degrees and area ratios larger than two, benefit the most from swirl. Wallis (1983), on the other hand, states that the benefits of swirl are scant and often countered by the losses associated with it—such as a higher outlet dynamic pressure loss. He concedes that it is generally accepted that swirl angles up to ten degrees may prove beneficial. However, rotor-only axial flow fans usually have larger outlet swirl angles.

Some of the earliest work on swirling flow in conical diffusers was done by Peters (1934). He reported an increase in diffuser efficiency for increased levels of swirl. However, McDonald *et al.* (1971) pointed out that it is unclear whether the efficiency increase was due to increased swirl or due to decreased inlet boundary layer thickness. Srinath (1968), referenced in McDonald *et al.* (1971), reported beneficial effects from swirl for equiangular annular diffusers with fully developed inlet flow. He found maximum pressure recovery with a swirl angle equal to the total divergence angle of the annular walls. The swirl angle was essentially constant across the diffuser inlet.

McDonald *et al.* (1971) performed experiments to determine the effect of a forced-vortex (or solid-body) inlet swirling flow on the performance of conical diffusers. They used 24 different diffusers with total divergence angles within the range of 4.0° to 31.2°. Moderate levels of swirl had no marked effect on unstalled diffusers under axial flow conditions. However, swirl significantly improved the performance of the diffusers that normally would have stalled. The geometry of optimum diffusers with inlet swirl is different from those with axial inflow: The line of optimum performance for fixed length ratios (i.e., the C_p^*-line) shifts to the left. Figure 2.3 illustrates this. Consequently, with the appropriate level of swirl, a shorter diffuser can be used to give the same performance.

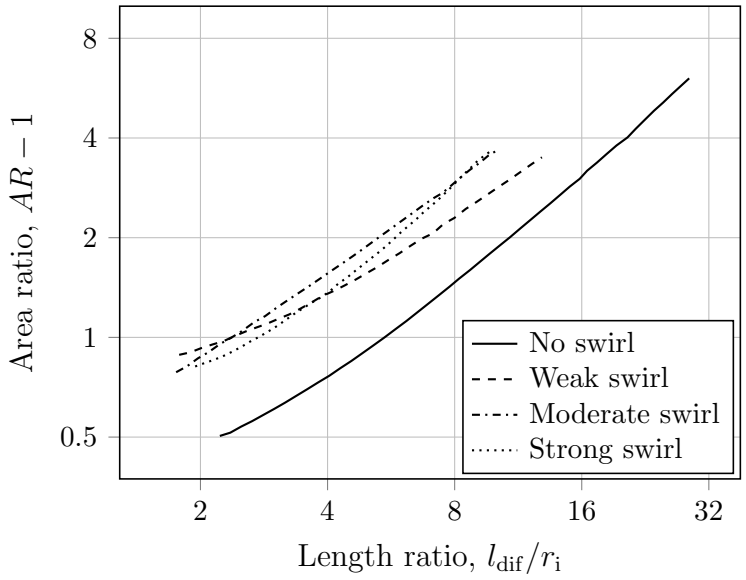

Figure 2.3: Effect of inlet swirl on the line of optimum performance at constant length ratios for conical diffusers (McDonald *et al.*, 1971)

Furthermore, McDonald *et al.* (1971) found that the performance of diffusers that benefit from swirl increases with swirl up to a point whereafter it starts to deteriorate. Pressure recovery as a function of swirl thus has a maximum rather than an asymptotic behaviour. Excessive swirl generates a stagnation bubble at the diffuser centreline, which decreases the effective flow area and thus performance. Harvey (1962) gave the criterion that if the angular momentum exceeds the axial momentum, a stagnation bubble will form. Since swirl angles tend to increase through a diffuser, the stagnation bubble is expected to start forming at the diffuser exit and move towards the inlet as swirl increases. So (1967) observed this flow behaviour in a conical diffuser with an included angle of 6° and an area ratio of 2.94. McDonald *et al.* (1971) added that the Harvey (1962) criterion holds only approximately for real swirl distributions.

Neve and Wirasinghe (1978) did comprehensive tests on conical diffusers with total divergence angles of 10°, 20° and 30°—all having area ratios of four. They introduced three levels of forced-vortex swirl intensities at the diffuser inlets. Improvements were only observed for the 20° and 30° diffusers, which would have suffered from flow separation with axial inlet flow conditions. They ascribe this improvement to the beneficial redistribution of the axial velocity profiles: The kinetic energy flux factor, α_e, in the downstream sections of the diffusers with inlet swirl was smaller compared to the ones without inlet swirl.

Senoo *et al.* (1978) studied the influence of swirl on conical diffuser performance using diffusers with divergence angles of 8°, 12°, 16°, 20° and 30°. The area ratio of all of them was slightly larger than four. They used a Rankin-vortex inlet swirl distribution. This distribution has a free-vortex outer part with uniform axial velocity and a forced-vortex inner part where the axial velocity is zero. They used a non-dimensional parameter, S, to quantify the swirl intensity. It is the ratio of angular momentum to axial momentum passing through a pipe section of radius R, viz.,

$$S = \frac{\int_0^R u_z u_\theta r^2 \,\mathrm{d}r}{R \int_0^R u_z^2 r \,\mathrm{d}r}. \tag{2.14}$$

With higher swirl intensities, the centreline axial velocity decreases and the velocity profile becomes more distorted. The axial pressure gradient near the centre is also considerably larger than near the wall. Shear forces balance these pressure forces acting on the core. The effect of the shear is to rapidly increase the radius of the forced-vortex core in the streamwise direction. The stronger the swirl, the larger the core becomes. Moderate levels of swirl can, therefore, improve the uniformity of the axial velocity profile and thus improve diffuser performance. Excessive swirl, however, forms a large forced-vortex core with low axial velocity. The effective cross-sectional area then decreases and diffuser performance is adversely affected. Senoo *et al.* (1978) concluded that there is an optimum diffuser opening angle with a corresponding optimum inlet swirl intensity. In their case, the $2\theta = 8°$ diffuser produced the highest pressure recovery for all levels of swirl. The optimum inlet swirl intensity was in the order of $S_\mathrm{i} = 0.10$ to 0.12. Reverse flow started at the centre when $S_\mathrm{i} = 0.18$.

Okhio *et al.* (1983) experimentally investigated the effect of swirl on wide angled conical diffusers. They used Rankin-vortex inlet swirl distributions with intensities of 0, 0.034, 0.055 and 0.854. A single diffuser with a total divergence angle of 16.5° and an area ratio of 4.4 was used. They also found that swirl improves diffuser performance up to a point after which it starts to deteriorate. Swirl increases the velocity near the wall and decreases it near the centre. With $S_\mathrm{i} = 0.854$, no separation from the wall was observed, but a recirculating core was present. The best results where achieved with $S_\mathrm{i} = 0.055$.

Kumar and Kumar (1980) experimented with swirling flows in annular diffusers with diverging centre bodies. Inlet swirl increased the overall static pressure recovery, especially for shorter and otherwise stalled diffusers. The largest portion of pressure recovery occurs at the initial stages of the diffuser, after which it flattens off. Swirl significantly reduces the chances of stall at the casing but shifts it to the hub. Moreover, they found that the optimum level of swirl is specific to a particular diffuser geometry.

Singh *et al.* (1994) did experimental work on the effect of forced-vortex inlet swirl on wide-angled annular diffusers with equal hub and casing wall angles. They tested three diffusers with wall angles of 20°, 25° and 30°—each at three maximum swirl angles of 12°, 17° and 25°. Swirl improved the pressure recovery in all the diffusers. The 30° diffuser with the highest degree of swirl gave the highest pressure recovery.

Mohan *et al.* (1998) performed a computational study to determine the best performance for a set of annular diffusers with and without inlet swirl. They tested three annular diffusers with area ratios of three under different levels of inlet swirl. The diffusers had equivalent cone angles of 12.5°, 15° and 17.5°. Singh *et al.* (2006) define the equivalent cone angle as

$$\theta_{\text{equiv}} = \arctan\left(\frac{d_{\text{equiv,o}} - d_{\text{equiv,i}}}{2l_{\text{dif}}}\right), \tag{2.15}$$

where $d_{\text{equiv,i}}$ and $d_{\text{equiv,o}}$ are the diameters of the equivalent circular areas at the diffuser inlet and outlet, respectively. As in agreement with other studies, Mohan *et al.* (1998) found that the pressure recovery increases with swirl up to a point whereafter it deteriorates. With insufficient swirl, the velocity profile is skewed towards the hub and separation is expected to start at the casing. With excessive swirl, it becomes skewed towards the casing and separation is likely to start at the hub. The shorter and wider the diffuser, the more swirl is needed to improve its performance and the more sensitive it becomes to the correct level of swirl. Note that this study employed the standard k-ε turbulence model with an upwind differencing scheme. These are not expected to yield accurate results for such complex flows. Nevertheless, the overarching trends are insightful and agree with literature.

Arora and Pathak (2009) numerically investigated the effect of swirl in annular diffusers. These diffusers had four different geometrical configurations but the same equivalent angle of ten degrees and an area ratio of two. The first had a cylindrical hub with a diverging casing and the second had equiangular diverging walls. The third diffuser had a diverging hub and casing of unequal angles. The fourth had a converging hub and diverging casing. Experimental inlet velocity profiles with and without swirl were used for the analysis. They tested the standard, realisable and RNG k-ε turbulence models. The RNG

variant agreed the closest with experimental data. They concluded that for all the diffusers except the one with the converging hub, pressure recovery improved with the addition of swirl up to 17° and then started to deteriorate. Any level of swirl reduced the performance of the diffuser with the converging hub. The diffuser with equiangular walls produced the highest pressure recovery.

Singh *et al.* (2006) performed a similar numerical investigation on the same four types of annular diffusers as tested by Arora and Pathak (2009), but with a constant area ratio of three, an axial length of 300 mm, and an equivalent cone angle of 15°. They found that the equiangular diffuser performed the best with swirling inlet flow. With stronger levels of inlet swirl, it and the unequal diverging hub and casing diffuser performed better than the diffusers with straight and converging hubs. The performance of the diffusers with straight and converging hubs was highly sensitive to inlet swirl. The diffuser with the converging hub performed the worst when swirl was introduced.

2.4.6 Diffuser performance enhancement

Short diffusers with large area ratios are often desired due to space limitations and cost advantages. This can be achieved by inserting vanes into a wide-angled diffuser, which reduces the included angles of the individual passes. However, the manufacturing difficulties and costs associated with conical vanes for conical diffusers have restricted its use in practice (Wallis, 1983: 96).

A tailpipe can convert excess dynamic pressure to static pressure by large-scale mixing (Miller, 1978: 37). For axial flow fan application, diffusion also takes place in a tailpipe since the annular area at the fan, due to the hub, increases to the area of the duct (Eck, 1973: 276). Depending on the inlet conditions and area ratio, a tailpipe of two to six outlet diameters can be added to an optimum diffuser for a small increase in pressure recovery (Wallis, 1983: 89). According to Miller (1978: 41), the tailpipe length is typically around four diameters.

Diffuser performance can be improved by removing the low-energy fluid near walls or re-energising the near-wall flow. It is very effective, but often impractical (Miller, 1978: 39). An upstream fan, however, can act as a vortex generator to help bring high-energy flow towards the walls to energise the near-wall flow.

2.5 Stators

Three main configurations are commonly encountered in axial flow fan applications: rotor-only units, prerotator-rotor units (rotor with inlet guide vanes), or rotor-stator units (rotor with outlet guide vanes). According to Wallis (1983: 303–304), induced draught ACC fans are usually rotor-only units because pressure rise requirements are relatively low. However, swirl energy is a loss

in fan systems that are devoid of stators (Wallis, 1983: 260). He, therefore, believes that increasing power costs will force fan industries to consider the use of stators. McKenzie (1997: 24) advocates for the use of a stator if the flow angle at the rotor outlet is larger than 15° and smaller than 45°.

According to Eck (1973: 231), outlet guide vanes (OGVs) are more common than inlet guide vanes (IGVs). OGVs turn the flow exiting the fan rotor towards the axial direction, decreasing the absolute velocity. Consequently, the static pressure rises in both the rotor and OGVs (whereas it drops in IGVs). Moreover, the velocities encountered by the blade passages are lower than in prerotator-rotor units, which implies reduced drag losses. Therefore, properly designed rotor-stator units are potentially more efficient than rotor-only and prerotator-rotor units (Wallis, 1983: 304). However, since flow straightening is a process of diffusion, OGVs are more susceptible to stall than IGVs. Smaller turning angles are thus possible, which is why Wallis (1983: 183) recommends a maximum swirl coefficient of 1.1 for OGVs as opposed to 1.4 for IGVs.

If the axial clearance between rotor and stator blades is too small, the pressure and velocity fields surrounding the blades interfere. Howell (1945) studied axial compressors and reported no change in load characteristics for axial clearances of $^1/_6$ to one chord length. Below $^1/_6$ chord, the stage pressure and temperature rise increased. Wallis (1983: 291) recommends straightener vanes to be located at least half a rotor blade chord length downstream of the blade trailing edge to minimise interference noise. The number of rotor and stator blades must also be unequal and have no common factor. In addition, the product of the number of stator blades and the rotational speed of the rotor should not coincide with a natural frequency of the rotor blades.

Marks and Weske (1934) designed and tested an axial flow fan intended for relatively high pressure duties. Their study aimed to investigate how the number of stator blades and axial clearance between it and the rotor affect fan performance and noise levels. The fan had three blades, a diameter of 0.49 m, a hub-to-tip ratio of 0.5, and a tip clearance of 25 mm. They performed efficiency tests with zero, five and ten stator blades whilst keeping the axial clearance between the rotor and stator constant at 35 mm. The static pressure at the point of maximum efficiency rose as the number of stator blades increased. At 3000 rpm, the total efficiency increased from 70 % with no stator blades to 79 % and 81 % with five and ten blades, respectively. However, increasing the number of stator blades results in steeper efficiency curves, making the fan unit more sensitive to off-design conditions. Thereafter, they varied the axial clearance between the fan and stator from 9.5 mm to 44.5 mm. It had a significant impact on the noisiness of the fan. Peak efficiency was reported with a clearance of 25 mm, but the noise was unacceptably loud. As a compromise, a clearance of 35 mm was adopted.

Terzis *et al.* (2012) experimentally investigated the effect of downstream guide vanes on the heat removal capability and performance characteristics of a small axial cooling fan. It had seven rotor blades with a hub-to-tip ratio of 0.4 followed by nine guide vanes. Pressure recovery was achieved with the guide vanes, resulting in a static efficiency increase in the order of ten per cent at a given mass flow rate and rotational speed. The inclusion of guide vanes did not alter the velocity triangles at the rotor nor the fan power consumption.

Munisamy *et al.* (2015) aimed to improve the efficiency of an axial flow fan using fixed guide vanes. A 12 bladed, 1.25 m diameter fan with a pitch angle of 30°, a hub-to-tip ratio of 0.28, and a tip clearance of 7 mm was used in the experimental investigation. The flow straightener had 13 vanes with a constant thickness of 3 mm and 40° inlet angle. The chord length was 300 mm followed by a 600 mm straight section to straighten the flow further. After adding the guide vanes, the total efficiency increased by 5.12 % and the power consumption decreased by 5.32 % near the design flow rate.

2.6 Numerical Considerations

The present study focusses on the flow downstream of a large axial flow fan. The aim is to reduce the outlet dynamic pressure loss using a stator, or a diffuser, or both. The problem at hand thus involves turbulent swirling flow that is exposed to an adverse pressure gradient, which may cause flow separation. Lee *et al.* (2012) state that such flows are amongst the most challenging flows to compute with turbulence models. Closure models that employ the Boussinesq approximation are generally unreliable for separated flows (Wilcox, 1998: 323). The law of the wall is also not always applicable near solid boundaries, especially when separation is expected (Wilcox, 1998: 174). According to Stewart *et al.* (2013), opposing pressure gradients may cause asymmetries or disturbances in both computational and experimental data, making such flows particularly challenging to validate. There are thus challenges involved in simulating and validating flows of this nature. The subsections to follow illustrate how these challenges have been dealt with in the literature.

2.6.1 Modelling non-swirling turbulent flows under adverse pressure gradients

The results of Lai *et al.* (1989) indicate that the k-ε turbulence model with wall functions and a low-Reynolds-number variant of Chien (1982) are incapable of computing the complex flow features in a 8° conical diffuser. Patel *et al.* (1985) tested various low-Reynolds-number models on various flow scenarios. They found that the model of Launder and Sharma (1974) performed reasonably well overall. However, Patel *et al.* (1985) argued that the *ad hoc* damping functions

used in most low-Reynolds-number turbulence models lack sound physical basis. Durbin (1991) found it unattractive to use a fundamentally incorrect model, and then correct it using arbitrary damping functions. He, therefore, developed a turbulence model that can deal with near-wall turbulence without the use of exponential damping functions or wall functions. It requires the solution of the ordinary k and ε equations, with additional equations for the turbulent stress normal to streamlines, $\overline{v'^2}$, and an elliptic damping function, f. Durbin (1995) tested the $\overline{v'^2}$-f model for turbulent separated flows over a backwards-facing step, in a planar diffuser, and around a triangular cylinder. These are representative of large separation, smooth separation, and unsteady vortex shedding. Although the original model was developed for attached and mildly separated flows, good agreement with experimental data is reported.

Apsley and Leschziner (1999) did a numerical study on turbulence modelling for non-swirling, separated flow in the asymmetric plane diffuser of Obi *et al.* (1993). They tested isotropic linear and hybrid two-equation eddy-viscosity models as well as anisotropic non-linear eddy-viscosity and stress-transport models. Consideration was given to the modelling of the near-wall flow. The study demonstrates the difficulty involved in turbulence modelling for such a simple yet non-trivial flow. Based on the agreement with experimental data, no class of turbulence model clearly outperformed the others.

Apsley and Leschziner (1999) concluded that standard linear eddy-viscosity models that do not have strain- or vorticity-dependent corrections fail to represent the flow in the Obi *et al.* (1993) diffuser. This diffuser is characterised by a strong adverse pressure gradient that provokes separation. The SST k-ω model predicted the general evolution of the diffuser flow but suffered from premature separation. For the non-linear models, Apsley and Leschziner (1999) found that it is the strain-dependent eddy-viscosity coefficient, and not the anisotropic terms, that is responsible for the improved response to the positive pressure gradient. However, none of these models predicted the correct amount of reverse flow. Despite stress-transport models' resting most firmly on fundamental foundations, owing to the difficulty in modelling the pressure-strain term, it does not guarantee better performance than simpler closures. The modelling of the near-wall asymptotic behaviour in low-Reynolds-number models also proved problematic since the high-Reynolds-number models with wall functions outperformed the low-Reynolds-number variants.

Iaccarino (2001) also performed simulations on the Obi *et al.* (1993) diffuser using different software packages and turbulence models. He focussed on the low-Reynolds k-ε model of Launder and Sharma (1974) and the four-equation $\overline{v'^2}$-f model of Durbin (1991). The agreement with experimental and LES data using the $\overline{v'^2}$-f model was impressive. On the other hand, the k-ε model did not predict separation at all and agreement with measured data was unacceptable.

El-Behery and Hamed (2011) did a comparative study on the performance of turbulence models using the Obi *et al.* (1993) diffuser. They tested the standard k-ε model of Launder and Spalding (1974), the low-Reynolds k-ε model of Launder and Sharma (1974), the standard k-ω model of Wilcox (1998), the SST k-ω model of Menter (1994), a Reynolds-stress model (RSM), and the $\overline{v'^2}$-f model of Durbin (1991) with the adaptions of Lien and Kalitzin (2001) for improved stability. The standard k-ε and RSMs employed the non-equilibrium wall functions of Kim and Choudhury (1995) that are sensitised to pressure gradients. The results obtained with the $\overline{v'^2}$-f model agreed the best with experimental data, followed by the standard and SST k-ω models. The standard and low-Reynolds k-ε models performed very poorly. In comparison to the better performing models, the RSM performed unexpectedly poor.

2.6.2 Modelling swirling turbulent flows under adverse pressure gradients

Armfield and Fletcher (1989) as well as Cho and Fletcher (1991) used algebraic stress models (ASMs) and k-ε turbulence models to compute the flow in a 8° diffuser without swirl and a 20° diffuser with swirl. The ASMs outperformed the k-ε models in the swirling and non-swirling cases. The standard k-ε model predicted the mean flow poorly. However, the near-wall Reynolds-stress and turbulent kinetic energy profiles were captured unsatisfactorily by both models. Near the exit of the diffusers, turbulence quantities were overpredicted for the non-swirling case and underpredicted for the swirling case.

Armfield *et al.* (1990) used an ASM and a k-ε turbulence model with the two-layer wall function of Chieng and Launder (1980) to compute turbulent swirling flow in conical diffusers. They simulated the solid-body rotation swirl case of Clausen *et al.* (1993) and the free-vortex case of Senoo *et al.* (1978). The ASM gave slightly better results, but it was less stable. They found that a two-layer, rather than a single-layer, wall function was necessary to accurately predict the level, location and axial variation of the near-wall peak in turbulence quantities of the forced-vortex swirl. The near-wall peak in turbulence is also substantially different from that encountered in non-swirling or free-vortex inlet swirling flows. A solid-body rotation inlet swirl produces higher axial near-wall velocities and lower centreline velocities compared to a free-vortex inlet swirl distribution. The radial gradients of the near-wall turbulence quantities are also much more pronounced with a forced-vortex inlet swirl distribution.

The experimental study of the swirling boundary layer developing in a conical diffuser of Clausen *et al.* (1993) became known as the ERCOFTAC conical diffuser test case and is commonly used for validation purposes. Several two-dimensional computations on this diffuser are available in Rodi *et al.* (1995). Gyllenram and Nilsson (2006) performed three-dimensional transient

simulations on the ERCOFTAC diffuser using very large eddy simulation (VLES). This method is a compromise between large eddy simulation (LES) and traditional statistical turbulence models based on the Reynolds-averaged Navier-Stokes (RANS) equations. LES often requires prohibitively large computational meshes, and RANS turbulence models are often incapable of distinguishing between large and small scale turbulence or unsteadiness. VLES applies a filter to the RANS turbulence model instead of the instantaneous conservation equations, as in LES. The purpose of the filter is to limit the influence of the RANS model on the unsteady mean flow. VLES thus allows for much coarser grids than LES. Gyllenram and Nilsson (2006) showed that this filtering technique could substantially improve the results of the low-Reynolds-number k-ω turbulence model. However, if the filter width is too narrow, the near-wall asymptotic behaviour of the turbulence model is not captured correctly and results deteriorate; if it is too large, the large-scale unsteadiness is not resolved. Moreover, results are sensitive to the filter width and are grid-dependent.

Bonous (2008) performed a thorough investigation on the ERCOFTAC conical diffuser using the open-source computational fluid dynamics (CFD) package, OpenFOAM. The effects of domain geometry, discretisation practices, pressure equation linear solvers, turbulence models, and boundary conditions were considered. Solutions were found to be sensitive to the specified inlet turbulence quantities and the order of the discretisation scheme. Results were insensitive to the linear solver and cross-sectional grid topology. However, Bonous (2008) only tested the standard k-ε and SST k-ω turbulence models with wall functions. More insight into the turbulence modelling and near-wall treatment is needed.

Dhiman *et al.* (2011) used ANSYS FLUENT 12.1 to test the performance of different turbulence models in conical diffusers with and without inlet swirl. They tested five turbulence models using steady-state simulations: the standard, realisable, renormalised group (RNG) k-ε, SST k-ω, and an RSM. To capture the near-wall flow, they used the enhanced wall treatment two-layer zonal model offered by FLUENT. It requires $y^+ \sim 1$ for the wall-adjacent cells. The standard k-ε model and RSM agreed the closest with the experimental data of Clausen *et al.* (1993), while the SST k-ω and RNG k-ε deviated the furthest. Interestingly, they reported improvements as high as 60 % for the streamwise velocity profiles near the centreline of the diffuser using a three-dimensional domain compared to a two-dimensional axisymmetric domain. They believed that the axisymmetric constraint might have eliminated physical aspects of the problem. Nevertheless, Dhiman *et al.* (2011) conceded that there is room for improvement. The turbulence models were incapable of capturing the details of the swirling flow in the diffuser.

Gatski and Speziale (1993) argue that the stress-strain relationship in traditional ASMs is not explicit in complex flows, resulting in numerical stiffness problems. They derived an explicit algebraic Reynolds-stress model (EASM) based on the SSG second-order closure model of Speziale, Sarkar and Gatski (1991) and applied it to non-trivial, two-dimensional turbulent flows involving shear and rotation. The results compared favourably with experimental and LES data. Furthermore, the EASM outperformed the standard k-ε model by some margin. From *et al.* (2017) used an extension of the EASM, based on the work of Wallin and Johansson (2000), to model the swirling flow in the ERCOFTAC conical diffuser. From *et al.* (2017) used the k-ω baseline (BSL-$k\omega$) model proposed by Menter (1994) to complete the two-equation EASM. The resulting BSL-$k\omega$-EASM accurately simulated the turbulent swirling flow throughout the ERCOFTAC conical diffuser. The agreement with experimental data for both near-wall and core-flow profiles was exceptional.

2.6.3 Modelling near-wall flows

Kim *et al.* (2005) made a comparison of near-wall treatment methods using different high-Reynolds-number turbulence models for flow over a backwards-facing step. They tested standard wall functions, non-equilibrium wall functions and a two-layer model with six different turbulence models. The standard wall functions are based on the proposal of Launder and Spalding (1974). The non-equilibrium wall functions of Kim and Choudhury (1995) are pressure-gradient sensitised to improve upon the accuracy of the standard wall functions. In the two-layer model, the computational domain is subdivided into a viscosity affected region and a fully turbulent region. The viscosity affected region employs the one-equation model of Wolfshtein (1969), and the fully turbulent region employs the k-ε or RSM models. The study reveals that the combination of the near-wall treatment and turbulence model affects results. Results obtained with the non-equilibrium wall functions together with the RNG and realisable k-ε models agreed the closest with the measured reattachment length, skin-friction, and static pressure coefficient. The two-layer method, combined with any turbulence model, provided physical velocity vectors. However, despite the computational expense, its results compared poorly with measurements.

Kalitzin *et al.* (2004) developed adaptive wall functions for RANS turbulence models. They are adaptive in that they do not restrict the location of the first grid point between the wall and log-layer. The motivations behind the development of adaptive wall functions are the potential gain in computational efficiency due to smaller grid sizes and aspect ratios in the near-wall cells. It also improves meshing flexibility. Standard wall functions require the first grid point above the wall to lie within the logarithmic layer, but practical meshes often violate this. If some wall-adjacent nodes fall within the viscous sublayer, log-layer wall functions generally provide unacceptable results.

The adaptive wall functions of Kalitzin *et al.* (2004) were derived for zero pressure gradient flow over a flat plate and were tested for y^+ equal to 0.11, 1.1, 2.5, 5, 11, 25, and 111. The correct profiles where obtained, but the largest errors were encountered for $5 < y^+ < 11$, which is in the buffer layer. They also tested the ability of the wall functions to capture pressure gradient driven separation and reattachment. Even though the wall functions do not account for pressure gradient and convection effects, they remain usable in the recirculation region. For the Spalart-Allmaras and k-ω models, the skin friction in the recirculation region was not sensitive to the height of the first cell centre above the wall. However, the $\overline{v'^2}$-f model showed significant sensitivity. Liu (2016) provides an in-depth description of how the wall functions of Kalitzin *et al.* (2004) are implemented in OpenFOAM.

2.6.4 Modelling turbomachinery blading

Meyer and Kröger (2001) point out that although many CFD codes include features to handle rotating blades, there are drawbacks in terms of meshing complexities and computational intensiveness. There is thus a need for a model that can accurately and efficiently simulate the effect of turbomachinery blading on a flow field.

Bredell (2005: 27–28) lists several axial flow fan models along with their advantages and disadvantages: the constant velocity, constant static pressure (or pressure jump), and varying static pressure fan models. They are simple to implement, but they provide purely axial discharge velocity profiles. The actuator disc model uses blade element (or isolated aerofoil) data to introduce momentum source terms into the flow field on the plane where the blades are located. These sources represent the effects blades would have on the flow field. This model renders realistic three-dimensional simulations that provide the pressure rise and power consumption corresponding to the flow rate through the fan. It also gives a reasonable representation of the flow field in the vicinity of the fan, i.e. axial and circumferential velocity profiles. Another strategy is to model the blades as solid rotating surfaces. This method is the most accurate but requires enormous computational resources.

Thiart and Von Backström (1993) developed an actuator disc model (ADM). It was successfully implemented in multiple studies simulating axial flow fans: Duvenhage *et al.* (1996), Meyer (2005) and Bredell *et al.* (2006) used the ADM to investigate the effect of inlet flow distortion on forced draught ACCs. Their results are consistent with the experimental measurements of Salta and Kröger (1995). Van Rooyen and Kröger (2008) simulated the effect of wind on the performance of a 30-fan ACC. Hotchkiss *et al.* (2006) used the ADM to study the effect of cross-flow on axial flow fan performance. Their results follow the measurements of Stinnes and Von Backström (2002). Meyer and

Kröger (2001) simulated the B2-fan with various blade setting angles. Their fan characteristics and velocity profiles compare well with the experimental data of Bruneau (1994) and Stinnes (1998). However, the downstream radial velocity profile is not well captured due to the inability of the model to account for radial forces. The fan power consumption is also slightly underpredicted due to the model's incapability of accounting for tip-clearance losses.

As a result of the ADM's inability to account for radial forces, it performs poorly at low flow rates where radial flow is present. Van der Spuy (2011), therefore, developed the extended actuator disc model (EADM) to compensate for this shortcoming. It augments the lift and drag characteristics of the selected blade profile at low flow rates. Himmelskamp (1947) determined that the lift characteristics of a rotating blade increase in the presence of radial flow. To model this phenomenon, Gur and Rosen (2005) extended the linear portion of the lift coefficient versus angle of attack characteristic curve of the particular aerofoil at low flow rates. Van der Spuy (2011) identified that stall occurs in the vicinity of the fan hub at low flow rates, which decreases the effect observed by Himmelskamp (1947). The EADM thus applies the model of Gur and Rosen (2005), but only above a specified radius ratio. The appropriate radius ratio is determined iteratively by comparing numerical results to experimental measurements and usually is around 0.5. Van der Spuy (2011: 64–65) simulated the performance characteristics for three different fans and demonstrated that the EADM outperforms the ADM at low flow rates. However, at very low flow rates, the EADM still underpredicts fan performance.

Thiart and Von Backström (1993) as well as Meyer and Kröger (2001) used the standard k-ε turbulence model with the ADM. Van der Spuy (2011) used the realisable k-ε model as it generally performs better than the standard version. Shih *et al.* (1995) demonstrated that the realisable k-ε model outperforms the standard k-ε model in several benchmark flows, which included rotating homogeneous shear flows and separated flows.

2.7 Conclusions

A brief history of different axial flow fan design methods for ACC application is provided in Section 2.2. Section 2.3 provides an introduction to pressure recovery, demonstrating its significance to axial flow fans. Walter *et al.* (2018) showed that outlet guide vanes together with an annular diffuser could increase the static efficiency of an axial flow fan by as much as 27 %. Section 2.4 highlights the difficulties involved in assessing diffuser performance, especially if swirl is present. It is often more practical to use simpler, yet less meaningful, definitions for diffuser performance. The absolute value of such performance parameters are not necessarily of importance; rather, it is useful to compare

the relative performance of different diffusers. It was also shown that diffuser performance generally suffers more from velocity profile distortion than viscous friction losses. The section further considers the performance of conical and annular diffusers as well as the influence inlet flow distortions, especially that of swirl, have on them. Increasing swirl intensities tend to increase the performance of otherwise stalled diffusers up to a point whereafter performance decays. Finally, diffuser performance enhancement methods are discussed, but they are found to be of academic value only. Miller (1978: 41), for example, states that the length of an effective tailpipe is typically four times the outlet diameter of the discharge diffuser. For large fans, such a tailpipe would be impractically long. Section 2.5 contains research on stators which further demonstrated that stators can aid axial flow fan performance.

The final section, Section 2.6, highlights challenges involved with simulating flows under adverse pressure gradients: Stewart *et al.* (2013) explain why it is challenging to validate flows with opposing pressure gradients; Wilcox (1998) warns against the use of turbulence models that employ the Boussinesq approximation or wall functions for separated flows. There is a trend in the research contained in Subsections 2.6.1 and 2.6.2 which illustrates the inadequacy of k-ε based turbulence models to compute the flow in diffusers—whether using standard, non-equilibrium, or two-layer wall functions, or even low-Reynolds-number corrections. Dhiman *et al.* (2011) are an exception: They obtained fair results for turbulent swirling flow in a diffuser using the standard k-ε model with a two-layer wall function. The $\overline{v'^2}$-f model is also based on the k-ε model, but good results were reported using it. Generally, better agreement with experimental data was obtained using k-ω based models rather than k-ε based models. There was no advantage in using Reynolds-stress models compared to simpler models. Therefore, based on the literature, discussions on turbulence modelling in the balance of this thesis will focus more on the k-ω and $\overline{v'^2}$-f turbulence models. Subsection 2.6.3 signifies the importance of the combination of turbulence model and near-wall treatment method. The final subsection, Subsection 2.6.4, presents different modelling strategies for axial flow fans. It focusses on the actuator disc and extended actuator disc models.

From the literature survey, it is evident that much research is available on forced draught air-cooled condensers. Comparatively, little information is available on induced draught systems. The effect of pressure recovery on the performance of axial flow fans has been studied, but only theoretically. The actuator disc model has been applied successfully to model axial flow fans; however, it has not yet been used to simulate a stator. The current study investigates pressure recovery for an induced draught fan arrangement. Pressure recovery will be achieved through various discharge configurations, which include combinations of stator blade rows, conical diffusers, and annular diffusers. Stator blade rows will be simulated using the extended actuator disc model.

Chapter 3

Analytical Investigation

3.1 Introduction

This chapter contains the specifications of the axial flow fan under consideration in the current study. The draught equation for an induced draught air-cooled condenser is given and manipulated into a form that clearly shows how the dynamic pressure loss can be converted to useful static pressure. The conversion of dynamic pressure to static pressure is termed pressure recovery. It is represented by a new dimensionless coefficient, K_{rec}. Thereafter, the various parameters affecting pressure recovery are scrutinised. It includes the effects of the kinetic energy profile correction factors at the fan and diffuser outlets, the diffuser area ratio, and the diffuser loss coefficient. The concluding section summarises the findings.

3.2 Fan System Specifications

Wilkinson *et al.* (2017) designed a large diameter, low pressure rise, rotor-only fan for a forced draught ACC. It is known as the M-fan. Its design specifications and performance characteristics are contained in Appendix A. Wilkinson *et al.* (2017) followed a similar design approach to Bruneau (1994) but used a different method to calculate the vortex distribution. The latter was done in accordance with the work of Von Backström *et al.* (1996), which aims to optimise the outlet velocity profile so that the discharge kinetic energy loss is minimised.

Wilkinson *et al.* (2017) evaluated the fan numerically using a three-dimensional periodic fan model with zero tip clearance. This model gave a fan static pressure rise of 114.7 Pa at the design flow rate of 333 m^3/s while consuming 64.24 kW of power. The static efficiency at the design point is thus 59.4 %, which is essentially equal to the design target of 60 %. However, Wilkinson *et al.* (2018) performed experiments on a scaled version of the M-fan and found that it does

not meet the desired static pressure or efficiency targets with the design blade setting angle of 34°. With a reduced tip gap and larger blade setting angle, however, the M-fan is suited for its intended application.

3.3 Draught Equation

The draught equation of an ACC is a mechanical energy relation that equates the mechanical energy supplied to the air by an axial flow fan to the energy dissipated through the ACC (Meyer and Kröger, 1998). Pressure changes due to devices encountered in the ACC are expressed as a dimensionless pressure loss or gain coefficient, given by

$$K = \frac{\Delta p}{\rho U_A^2/2}, \tag{3.1}$$

where Δp is the pressure loss or rise across the device, ρ is density, and U_A is the average velocity based on a characteristic cross-sectional area.

Kröger (1998: 8.1.8) derived the draught equation for an induced draught ACC fitted with an exhaust diffuser. Following the same approach, the draught equation for the V-frame induced draught system in Fig. 3.1 is deduced, i.e.,

$$\begin{aligned}
&p_{\mathrm{a1}}\left[\{1-0.00975(H_7-H_4)/T_{\mathrm{a4}}\}^{3.5}-\{1-0.00975(H_7-H_4)/T_{\mathrm{a1}}\}^{3.5}\right]\\
&=K_{\mathrm{ts}}(\dot{m}_{\mathrm{a}}/A_2)^2/(2\rho_{\mathrm{a1}})+K_{\mathrm{he\theta}}(\dot{m}_{\mathrm{a}}/A_{\mathrm{fr}})^2/(2\rho_{\mathrm{a34}})\\
&+K_{\mathrm{pl}}(\dot{m}_{\mathrm{a}}/A_{\mathrm{FC}})^2/(2\rho_{\mathrm{a4}})+K_{\mathrm{up}}(\dot{m}_{\mathrm{a}}/\Delta A_{\mathrm{F}})^2/(2\rho_{\mathrm{a4}})\\
&-(K_{\mathrm{Fs}}+\alpha_{e\mathrm{FC}})(\dot{m}_{\mathrm{a}}/A_{\mathrm{FC}})^2/(2\rho_{\mathrm{a4}})+K_{\mathrm{do}}(\dot{m}_{\mathrm{a}}/\Delta A_{\mathrm{F}})^2/(2\rho_{\mathrm{a4}})\\
&+K_{\mathrm{dif}}(\dot{m}_{\mathrm{a}}/A_{\mathrm{FC}})^2/(2\rho_{\mathrm{a4}})+\alpha_{e7}(\dot{m}_{\mathrm{a}}/A_7)^2/(2\rho_{\mathrm{a4}}).
\end{aligned} \tag{3.2}$$

The respective loss coefficients are the following: K_{ts} for the tower supports, $K_{\mathrm{he\theta}}$ for the slanted heat exchanger, K_{pl} for the plenum chamber, K_{up} and K_{do} for the fan upstream and downstream losses, and K_{dif} for the diffuser. K_{Fs} is the fan static pressure rise coefficient. The kinetic energy flux factors at the fan and diffuser outlets are $\alpha_{e\mathrm{FC}}$ and α_{e7}, respectively. A_{FC} is the total area of the fan casing, ΔA_{F} is the annular area between the fan casing and hub, and A_{fr} is the frontal area of the heat exchanger. It is assumed that $H_4 \approx H_3$, $\rho_{\mathrm{a2}} \approx \rho_{\mathrm{a1}}$, $\rho_{\mathrm{a7}} \approx \rho_{\mathrm{a6}} \approx \rho_{\mathrm{a5}} \approx \rho_{\mathrm{a4}}$, and $\rho_{\mathrm{a34}} \approx 2p_{\mathrm{a1}}/[R(T_{\mathrm{a3}}+T_{\mathrm{a4}})]$.

Kröger (1998) then simplified Eq. (3.2) by assuming $\alpha_{e7} \approx \alpha_{e\mathrm{FC}}$ for a short diffuser. However, Sovran and Klomp (1967: 293–296), Miller (1971: 79), and Blevins (1984: 145) agree that diffuser performance is heavily affected by these inlet and outlet kinetic energy correction terms (see Subsection 2.4.1). Kröger's (1998) simplification will, therefore, not be made in the currant analysis.

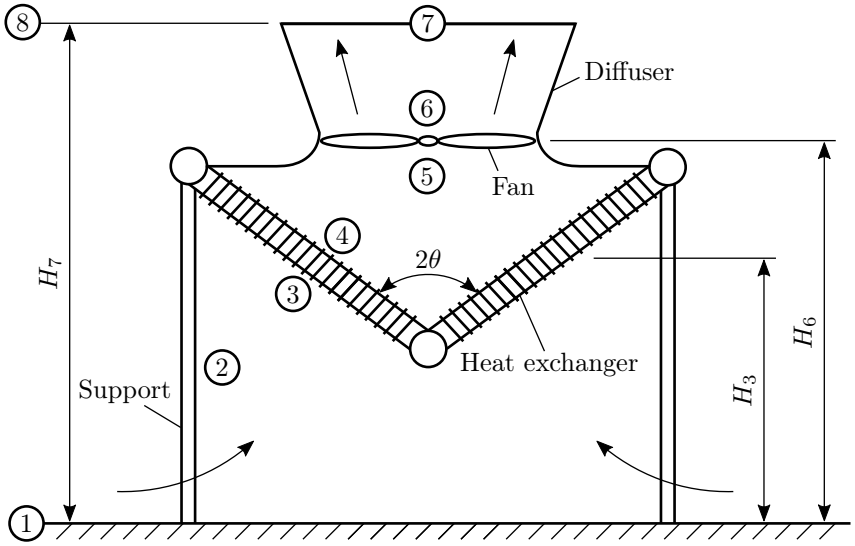

Figure 3.1: V-frame induced draught air-cooled condenser

Neglecting buoyancy effects and collecting the system losses in a single term, Eq. (3.2) can be written in a form that equates the total pressure supplied to the total pressure dissipated through the ACC, i.e.,

$$\Delta p_{\mathrm{Fs}} + \alpha_{e\mathrm{FC}} \rho U_{\mathrm{FC}}^2/2 = \Delta p_{\mathrm{sys}} + K_{\mathrm{dif}} \rho U_{\mathrm{FC}}^2/2 + \alpha_{e\mathrm{difo}} \rho U_{\mathrm{difo}}^2/2, \tag{3.3}$$

where Δp_{Fs} denotes the fan static pressure rise and U_{FC} the mean velocity through the fan casing. The sum of the total pressure losses in the ACC, excluding that of the diffuser and the discharge kinetic energy loss, is represented by Δp_{sys}. The excluded terms are given by the last two terms, where $\alpha_{e\mathrm{difo}}$ is the kinetic energy flux factor at the diffuser outlet and U_{difo} the mean discharge velocity. The diffuser and outlet dynamic pressure losses are intentionally excluded from Δp_{sys} since they influence pressure recovery.

In reality, $\alpha_{e\mathrm{FC}}$, K_{dif} and $\alpha_{e\mathrm{difo}}$ are unknown and impractical to measure. Kröger (1998: 8.1.9), therefore, argued that it is useful to have the performance characteristics of the fan-diffuser unit. Four terms in Eq. (3.3) can then be replaced by

$$\Delta p_{\mathrm{F/difs}} = \Delta p_{\mathrm{Fs}} + \alpha_{e\mathrm{FC}} \rho U_{\mathrm{FC}}^2/2 - K_{\mathrm{dif}} \rho U_{\mathrm{FC}}^2/2 - \alpha_{e\mathrm{difo}} \rho U_{\mathrm{difo}}^2/2, \tag{3.4}$$

in which case the draught equation becomes

$$\Delta p_{\mathrm{F/difs}} = \Delta p_{\mathrm{sys}}. \tag{3.5}$$

3.4 Pressure Recovery

Pressure recovery refers to the reduction of the outlet dynamic pressure loss by converting a portion of it to static pressure. Recovery can be achieved with the aid of a diffuser, a stator, or both. A diffuser will reduce both the axial and circumferential kinetic energy components due to the conservation of mass and angular momentum, respectively. A stator will only reduce the circumferential component as it removes the swirl.

As mentioned earlier, $\alpha_{e\mathrm{FC}}$, K_{dif} and $\alpha_{e\mathrm{difo}}$ are usually not known. In order to distinguish between Δp_{Fs} and $\Delta p_{\mathrm{F/difs}}$, a dimensionless coefficient, K_{rec}, is introduced. It represents the kinetic energy at the fan outlet that is recovered within the discharge diffuser or stator. Pressure recovery increases the amount of energy available to the airstream, making $\Delta p_{\mathrm{F/difs}} > \Delta p_{\mathrm{Fs}}$. This concept is taken from Meyer and Kröger (1998) who introduced K_{rec} to represent the kinetic energy recovered within the plenum chamber of a forced draught ACC. In this study, the pressure recovery coefficient is defined as

$$\begin{aligned} K_{\mathrm{rec}} &= \frac{\alpha_{e\mathrm{FC}}\rho U_{\mathrm{FC}}^2/2 - \alpha_{e\mathrm{difo}}\rho U_{\mathrm{difo}}^2/2 - K_{\mathrm{dif}}\rho U_{\mathrm{FC}}^2/2}{\rho U_{\mathrm{FC}}^2/2} \\ &= \alpha_{e\mathrm{FC}} - \alpha_{e\mathrm{difo}}(A_{\mathrm{FC}}/A_{\mathrm{difo}})^2 - K_{\mathrm{dif}}, \end{aligned} \tag{3.6}$$

Substituting Eq. (3.6) into Eq. (3.3) yields the following form of the draught equation that can be used to determine the operating point of the ACC, i.e.,

$$\Delta p_{\mathrm{Fs}} + K_{\mathrm{rec}}\rho U_{\mathrm{FC}}^2/2 = \Delta p_{\mathrm{sys}}. \tag{3.7}$$

The theoretical maximum operating point would occur if $K_{\mathrm{rec}} = \alpha_{e\mathrm{FC}}$, in which case the available pressure would be equal to the fan total-to-total pressure rise, i.e. $\Delta p_{\mathrm{Ft}} = \Delta p_{\mathrm{Fs}} + \alpha_{e\mathrm{FC}}\rho U_{\mathrm{FC}}^2/2$. However, $\alpha_{e\mathrm{difo}} \geq 1$ as dictated by continuity, A_{difo} is limited by diffuser stall, and $K_{\mathrm{dif}} > 0$ due to viscous losses. The available pressure will, therefore, lie somewhere between the extremes of the total-to-static and total-to-total pressures, as depicted in Fig. 3.2.

Figure 3.2 illustrates that the result of pressure recovery is to shift the operating point to a higher volume flow rate compared to the initial design point. This poses various options for the ACC designer, i.e. operate at the new higher flow rate or adjust the fan to return to the initial design point. The former will possibly allow for a smaller overall plant structure size since higher heat removal rates are possible at higher airflow rates; the latter potentially allows for a smaller fan, or a fan rotating at a reduced speed, or a reduced blade setting angle. However, Eq. (3.6) shows that pressure recovery is a function of various parameters. It can, therefore, not be assumed that the amount of pressure recovery will remain constant if adjustments are made to the fan, which complicates the prediction of the final system operating point.

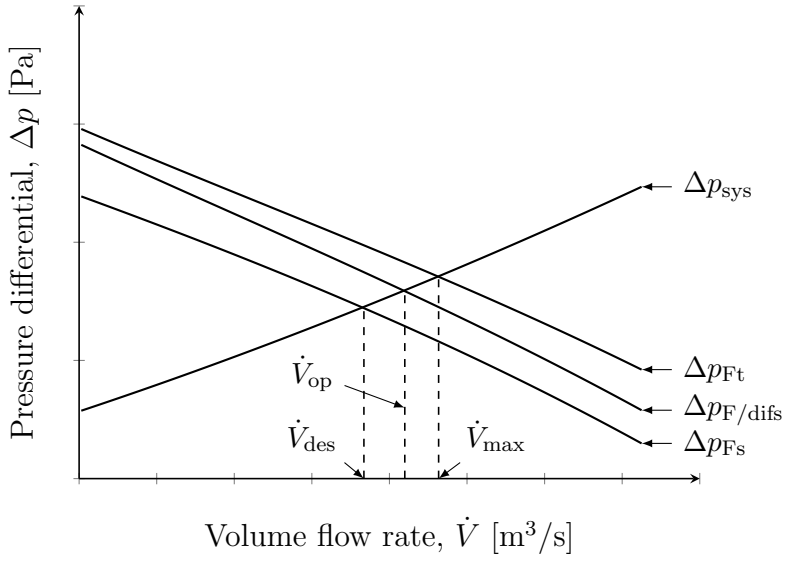

Figure 3.2: Effect of pressure recovery on fan pressure characteristics

The fan power characteristic curve is usually relatively flat and is not expected to change much with the addition of a diffuser or stator. Terzis *et al.* (2012), for example, found that the specific fan power, $P_{\mathrm{F}}/\dot{V}$, remained unchanged whether outlet guide vanes were present or not. The efficiency at which the system will operate, $\eta_{\mathrm{F/difs}}$, will thus also lie somewhere between the total-to-static and total-to-total efficiencies, as illustrated in Fig. 3.3.

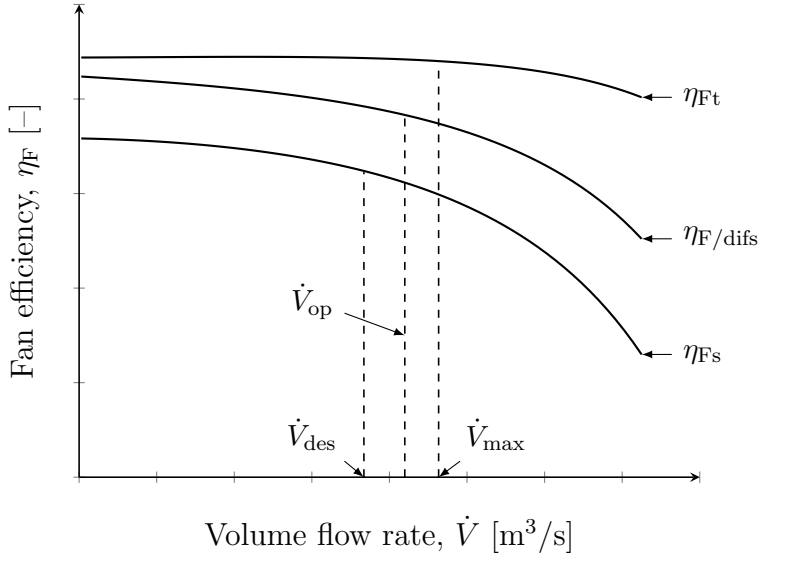

Figure 3.3: Effect of pressure recovery on fan efficiency characteristics

3.5 Parameters Affecting Pressure Recovery

This section inspects how the various parameters in Eq. (3.6) influence pressure recovery. These include the kinetic energy correction factors at the fan and diffuser outlets, the area ratio of the diffuser, and the total pressure loss coefficient of the diffuser.

3.5.1 Fan outlet kinetic energy factor

As defined in BS 848 (2007: 14), the kinetic energy correction factor is a dimensionless coefficient equal to the time-averaged flux of kinetic energy through a section, divided by the mean kinetic energy through that section:

$$\alpha_e = \frac{\iint_A \rho(\mathbf{u}\cdot\mathbf{n})u^2 \,\mathrm{d}A}{\dot{m}U_A^2}, \tag{3.8}$$

where u is the local velocity magnitude, $\mathbf{u}$ the velocity vector, $\mathbf{n}$ the surface normal vector, and $U_A = \dot{V}/A$ the mean velocity through that particular section. The minimum kinetic energy flux would occur if the velocity were perfectly uniform across the specified section, in which case α_e would be equal to unity. The effect of velocity non-uniformity is to make α_e greater than unity.

Meyer and Kröger (2004) state that the kinetic energy factor at the fan outlet can be as high as three. An assumption of unity is thus inadequate to describe the relationship between the fan pressure rise characteristics and the system losses in an arbitrary fan system. Furthermore, the kinetic energy factor at the fan outlet is a function of the volume flow rate. Meyer (2000: G.11) calculated $\alpha_{e\mathrm{FC}}$ from numerical results using the following expression:

$$\alpha_{e\mathrm{FC}} = \frac{1}{U_{\mathrm{FC}}^3 A_{\mathrm{FC}}} \sum_{i=1}^{N} u_{zi}\big(u_{xi}^2 + u_{yi}^2 + u_{zi}^2\big)A_i, \tag{3.9}$$

where u_{xi}, u_{yi} and u_{zi} are the Cartesian components of the velocity vector at the i^{th} cell out of N cells at the fan outlet. In a similar manner, Eq. (3.8) can be expressed in cylindrical coordinates as

$$\alpha_{e\mathrm{FC}} = \frac{1}{U_{\mathrm{FC}}^3 A_{\mathrm{FC}}} \iint_{A_{\mathrm{FC}}} u_z\big(u_z^2 + u_\theta^2 + u_r^2\big)\,\mathrm{d}A_{\mathrm{FC}}\,, \tag{3.10}$$

where $U_{\mathrm{FC}} = \dot{V}/A_{\mathrm{FC}}$ and u_z, u_θ, and u_r are the local axial, circumferential and radial velocity components, respectively. Following Nilsson and Davidson (2001) and Andersson (2009: 23), the kinetic energy factor can be decomposed into components, i.e. an axial component

$$\alpha_{e\mathrm{FC}z} = \frac{1}{U_{\mathrm{FC}}^3 A_{\mathrm{FC}}} \iint_{A_{\mathrm{FC}}} u_z^3 \,\mathrm{d}A_{\mathrm{FC}}\,, \tag{3.11a}$$

a circumferential component

$$\alpha_{e\mathrm{FC}\theta} = \frac{1}{U_{\mathrm{FC}}^3 A_{\mathrm{FC}}} \iint_{A_{\mathrm{FC}}} u_z u_\theta^2 \, \mathrm{d}A_{\mathrm{FC}} \,, \tag{3.11b}$$

and a radial component

$$\alpha_{e\mathrm{FC}r} = \frac{1}{U_{\mathrm{FC}}^3 A_{\mathrm{FC}}} \iint_{A_{\mathrm{FC}}} u_z u_r^2 \, \mathrm{d}A_{\mathrm{FC}} \,. \tag{3.11c}$$

It is thus clear that

$$\alpha_{e\mathrm{FC}} = \alpha_{e\mathrm{FC}z} + \alpha_{e\mathrm{FC}\theta} + \alpha_{e\mathrm{FC}r}. \tag{3.12}$$

The minimum value for $\alpha_{e\mathrm{FC}z}$ is equal to unity due to continuity. For $\alpha_{e\mathrm{FC}\theta}$ and $\alpha_{e\mathrm{FC}r}$, the minimum is zero. The radial component is generally negligibly small at the outlet of near free-vortex fans.

The kinetic energy factor at the fan outlet is fixed for a specified operating point. The larger it is, the more potential there is for pressure recovery. Figure 3.4 presents the kinetic energy profile correction factor at the exit of the M-fan as a function of volume flow rate and Fig. 3.5 shows its axial and circumferential components. The radial component is negligibly small and hence not shown. At the design point (i.e., $\dot{V} = 333\,\mathrm{m}^3/\mathrm{s}$), $\alpha_{e\mathrm{FC}} \approx 1.454$, $\alpha_{e\mathrm{FC}z} \approx 1.198$ and $\alpha_{e\mathrm{FC}\theta} \approx 0.256$. There is thus slightly more potential for pressure recovery in the circumferential component than in the axial component.

3.5.2 Diffuser outlet kinetic energy factor

In order to maximise pressure recovery for a given area ratio, $\alpha_{e\mathrm{difo}}$ should be as small as possible. The theoretical minimum for $\alpha_{e\mathrm{difo}}$ is unity, which would be the case if the flow at the outlet is perfectly uniform without any swirl or radial flow. Kröger (1998: 2.3.1) states that $\alpha_e \approx 1$ is approximately true for fully developed axial turbulent flow in a pipe. Since a stator can be used to remove swirl, another case to consider is one where $\alpha_{e\mathrm{difo}} \approx \alpha_{e\mathrm{FC}} - \alpha_{e\mathrm{FC}\theta} \approx \alpha_{e\mathrm{FC}z}$.

Figure 3.6 illustrates how $\alpha_{e\mathrm{difo}}$ influences the characteristics of the M-fan. The first is the ideal case where $\alpha_{e\mathrm{difo}} \approx 1$. The second is the case where the swirl is removed so that $\alpha_{e\mathrm{difo}} \approx \alpha_{e\mathrm{FC}z}$. In both cases, the area ratio, AR, and diffuser loss coefficient, K_{dif}, are set equal to unity and zero, respectively. This essentially means that no diffuser is present and that the losses in the stator are insignificant. A system curve of the form $\Delta p_{\mathrm{sys}} = a\dot{V}^2$ is included in Fig. 3.6a (and later in Fig. 3.7a). It passes through the origin and the design point of $\dot{V} = 333\,\mathrm{m}^3/\mathrm{s}$ and $\Delta p_{\mathrm{Fs}} = 114.7\,\mathrm{Pa}$. The system curve serves to illustrate how pressure recovery shifts the operating point of the fan system.

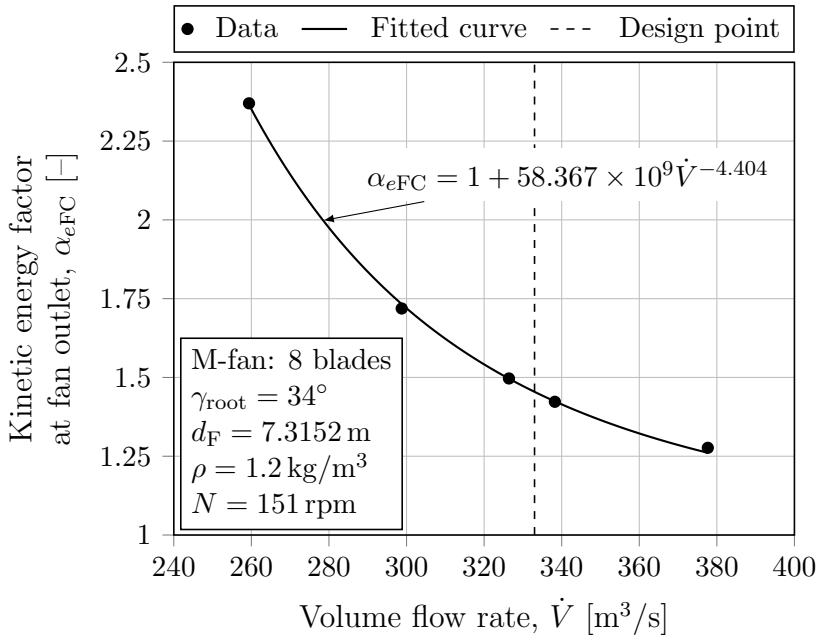

Figure 3.4: Kinetic energy factor at the M-fan outlet

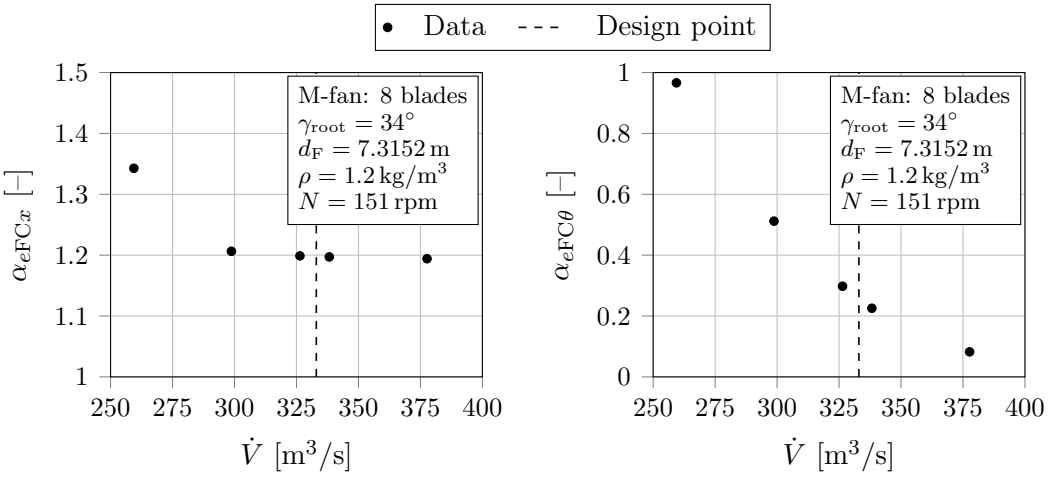

(a) Axial component (b) Circumferential component

Figure 3.5: Components of the kinetic energy factor at the M-fan outlet

At the design flow rate in Fig. 3.6, the pressures are 132.4 and 124.7 Pa for $\alpha_{e\mathrm{difo}} \approx 1$ and $\alpha_{e\mathrm{difo}} \approx \alpha_{e\mathrm{FC}z}$, respectively. The efficiencies are 68.5 and 64.6 %, respectively. The new operating flow rates are 340.6 m³/s for $\alpha_{e\mathrm{difo}} \approx 1$ and 337.2 m³/s for $\alpha_{e\mathrm{difo}} \approx \alpha_{e\mathrm{FC}z}$. At these new flow rates, the pressures are 120.2 and 117.9 Pa, respectively; the efficiencies are 65.9 and 63.0 %, respectively. The operating flow rate for $\alpha_{e\mathrm{difo}} \approx 1$ is thus 2.3 % higher than the design flow rate and the operating pressure is 4.8 % higher than the design fan static

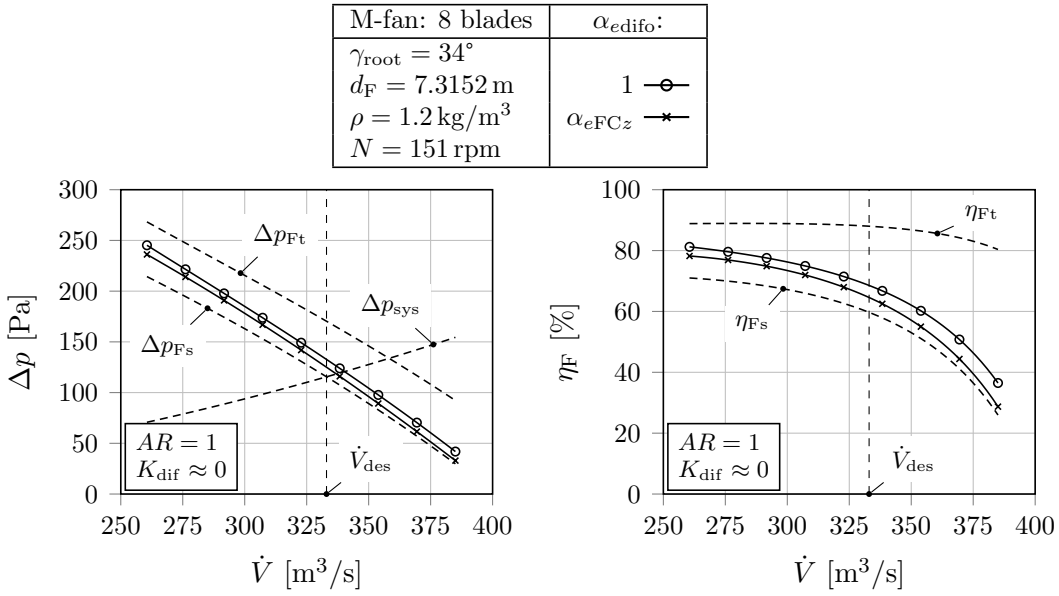

(a) Pressure characteristics (b) Efficiency characteristics

Figure 3.6: Effect of α_{edifo} on the M-fan characteristics (fan total-to-static characteristics from Wilkinson *et al.* (2018))

pressure. The efficiency at the operating point is 6.5 % (absolute) higher than the design fan static efficiency of 59.4 %, reported by Wilkinson *et al.* (2017). For $\alpha_{edifo} \approx \alpha_{eFCz}$, the operating flow rate is 1.3 % higher, the operating pressure is 2.8 % higher, and the operating efficiency is 3.6 % (absolute) higher than they are at the design point.

3.5.3 Diffuser area ratio

For maximum pressure recovery within a specified length, the area ratio should be as large as possible while avoiding flow separation. This is the classic challenge with diffuser selection: An excessive area ratio for a specified length results in flow separation and unacceptable losses; however, increasing the length to obtain a specified area ratio may result in excessive frictional losses and impractically lengthy units. The area ratio and diffuser loss coefficient are thus closely related since K_{dif} accounts for frictional and separation losses. Nevertheless, to illustrate the effect of near-optimum diffuser area ratios on the system characteristics, the outlet kinetic energy factor and diffuser loss coefficient are fixed at $\alpha_{edifo} \approx \alpha_{eFC}$ and $K_{dif} \approx 0.2$, respectively. The former assumption follows from Kröger (1998: 8.1.8) for short diffusers. However, in reality the zero-slip condition at the diffuser wall tends to peak the exit profile so that $\alpha_{edifo} > \alpha_{eFC}$ (Blevins, 1984: 145). The selected diffuser loss coefficient is recommended by Wallis (1983: 92) for optimum diffuser geometries (the following subsection elaborates on this recommendation).

It was decided to set the diffuser length equal to the fan diameter, i.e. $l_{\text{dif}} = 7.3152\,\text{m}$. From Fig. 2.1 on page 9 at a length ratio of $l_{\text{dif}}/r_{\text{i}} = 2$, practical conical diffusers lie within the approximate range of $1.3 \lesssim AR \lesssim 1.45$. However, Fig. 2.3 on page 14 illustrates that the upper limit can be as high as 1.8 when swirl is present. The annular width between the fan hub and casing is $\Delta r_{\text{i}} = 2.6$. From Fig. 2.2 on page 11 at a length ratio of $l_{\text{dif}}/\Delta r_{\text{i}} = 2.82$, practical annular diffusers lie within the approximate range of $1.3 \lesssim AR \lesssim 1.5$. The area ratios for Fig. 3.7 were thus selected to fall within the range of $1.3 \leq AR \leq 1.8$.

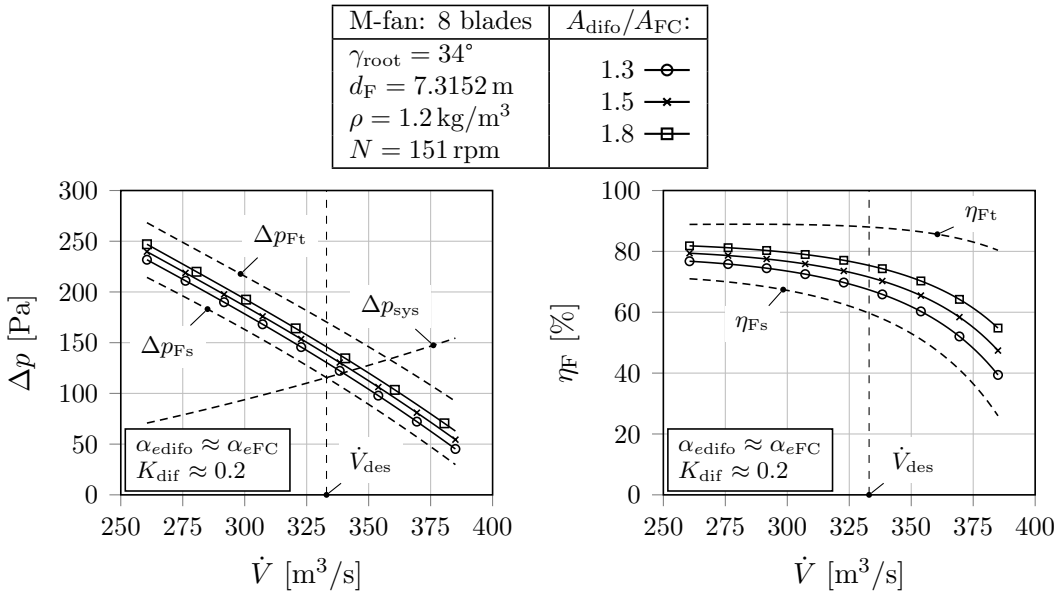

(a) Pressure characteristics (b) Efficiency characteristics

Figure 3.7: Effect of $A_{\text{difo}}/A_{\text{FC}}$ on the M-fan characteristics (fan total-to-static characteristics from Wilkinson *et al.* (2018))

At the design point in Fig. 3.7a, the pressures are 130.1, 138.2 and 145.6 Pa for area ratios of 1.3, 1.5 and 1.8, respectively. Figure 3.7b illustrates that the efficiency at the design point is sensitive to the area ratio since an area ratio as small as 1.3 results in an absolute efficiency increase of 8.0 % over the reported fan static efficiency of 59.4 % (Wilkinson *et al.*, 2017). The efficiencies for area ratios of 1.5 and 1.8 are 71.5 and 75.4 %, respectively. The operating flow rates shifted to 339.9, 343.6 and 347.0 m^3/s for the respective area ratios. The efficiencies at these operating flow rates are 65.4, 68.8 and 72.3 % for the listed area ratios, respectively.

3.5.4 Diffuser loss coefficient

The diffuser loss coefficient represents the non-dimensional loss in total pressure across the diffuser. According to Wallis (1983: 91), diffuser effectiveness data

above 0.9 for two-dimensional, conical, and annular diffusers with thin inlet boundary layers and no tailpipes have been reported. For thicker inlet boundary layers, peak effectiveness values in excess of 0.8 are normally reported. Flow asymmetry or non-uniformity further reduce diffuser performance. Therefore, Wallis (1983: 92) and Eck (1973: 277) recommend a conservative diffuser effectiveness value of 0.8 (or $K_{\text{dif}} = 0.2$) for diffusers with symmetrical inlet flow conditions and optimum geometries.

It was not considered meaningful to look at a case where K_{dif} is varied while the area ratio and kinetic energy factor are held constant. The diffuser loss coefficient is very much a function of its area ratio. For example, it could be argued that $K_{\text{dif}} = 0$ implies the absence of a diffuser, which means the area ratio is one and $\alpha_{\text{edifo}} \approx \alpha_{e\text{FC}}$. In this case, the pressure recovery coefficient, K_{rec}, would be equal to zero (see Eq. (3.6)). Another way of looking at it is to say that $K_{\text{dif}} = \alpha_{e\text{FC}}$, which corresponds to a free jet discharge with an infinite area ratio. This also makes K_{rec} equal to zero. The diffuser loss coefficient will thus lie between the limits of zero and $\alpha_{e\text{FC}}$ depending on its area ratio. However, from Eq. (3.6) it is obvious that K_{dif} reduces pressure recovery and should, therefore, be kept to a minimum.

3.6 Conclusions

A brief overview of Wilkinson *et al.*'s (2017) M-fan is provided in Section 3.2. At the design flow rate of $333\,\text{m}^3/\text{s}$, the fan yields a static pressure rise of 114.7 Pa at a static efficiency of 59.4 % while consuming energy at a rate of 64.24 kW. Section 3.3 presents the draught equation for an induced draught air-cooled condenser. It is simplified in Section 3.4 by introducing a non-dimensional pressure recovery coefficient to illustrate the effect of pressure recovery on the draught equation. This recovery coefficient consists of four parameters: the fan exit kinetic energy factor, the diffuser discharge kinetic energy factor, the diffuser area ratio, and the diffuser loss coefficient. The effects of these parameters on the performance of the M-fan are evaluated in Section 3.5: Subsection 3.5.1 demonstrates that the convention of assuming $\alpha_{e\text{FC}} \approx 1$ at the fan outlet is overly simplistic—at the M-fan design point, $\alpha_{e\text{FC}} \approx 1.45$. If a stator removes the swirl at the design point, the fan efficiency will increase by about 5 % (see Subsection 3.5.2). Subsection 3.5.3 illustrates that a diffuser with an area ratio of 1.5 and a loss coefficient of 0.2 may increase the flow rate through the fan by 3 %. At this new operating point, the static efficiency is 9 % higher than the efficiency at the original design flow rate. Lastly, consideration is given to the diffuser loss coefficient in Subsection 3.5.4.

Chapter 4

Modelling Strategies

4.1 Introduction

This chapter focusses on modelling strategies to represent the effects of turbulence and turbomachinery blading on the mean flow. As a start, the conservation laws that govern all fluid flows are presented. The closure problem is illustrated when these equations are averaged. This leads to the broad topic of turbulence modelling. Finally, the modelling equations for the actuator disc model that was introduced in Subsection 2.6.4 are presented.

4.2 Governing Equations

Conservation laws govern fluid motion. The equations representing these laws can be written in the form of a general transport equation, viz.,

$$\frac{\partial \rho\phi}{\partial t} + \boldsymbol{\nabla} \cdot (\rho\phi\mathbf{u}) = \boldsymbol{\nabla} \cdot (\Gamma_\phi \boldsymbol{\nabla}\phi) + S_\phi, \tag{4.1}$$

where ϕ represents an arbitrary flow variable, Γ_ϕ a diffusion coefficient, and S_ϕ any sources or sinks that affect the quantity ϕ. For turbulent flows, ϕ can be decomposed into a mean and fluctuating component, i.e. $\phi(\mathbf{x}, t) = \Phi(\mathbf{x}) + \phi'(\mathbf{x}, t)$. Inserting this into Eq. (4.1) and taking the time average yields the general time-averaged transport equation for the quantity ϕ, viz.,

$$\frac{\partial \rho\Phi}{\partial t} + \boldsymbol{\nabla} \cdot \left(\rho\mathbf{U}\Phi + \rho\overline{\mathbf{u}'\phi'}\right) = \boldsymbol{\nabla} \cdot (\Gamma_\phi \boldsymbol{\nabla}\Phi) + S_\phi. \tag{4.2}$$

4.2.1 Instantaneous conservation equations

The continuity and momentum equations for incompressible Newtonian fluids are presented in Wilcox (1998: 35), viz.,

$$\frac{\partial u_i}{\partial x_i} = 0, \tag{4.3}$$

$$\rho\frac{\partial u_i}{\partial t} + \rho u_j\frac{\partial u_i}{\partial x_j} = -\frac{\partial p}{\partial x_i} + \frac{\partial \sigma_{ji}}{\partial x_j}, \tag{4.4}$$

where u_i and x_i are velocity and position vectors, and σ_{ij} is the viscous-stress tensor. In a Newtonian fluid, the viscous stresses are proportional to the rate of deformation. The unknown viscous-stress tensor can, therefore, be expressed in terms of the local strain rate, i.e.,

$$\sigma_{ij} = 2\mu s_{ij}, \tag{4.5}$$

where s_{ij} is the strain-rate tensor, given by

$$s_{ij} = \frac{1}{2}\left(\frac{\partial u_i}{\partial x_j} + \frac{\partial u_j}{\partial x_i}\right). \tag{4.6}$$

Equations (4.3) and (4.4) along with the energy equation, exhibit a system of partial differential equations (PDEs) that entirely describe any flow field. With the equations of state and the Newtonian model given by Eq. (4.5), this system is mathematically closed. That is, the system can be solved without modelling any other flow variables. This approach is referred to as direct numerical simulation (DNS), which resolves the mean flow and turbulent fluctuations. However, the spatial grid spacing and time scale must be small enough to capture Kolmogorov length scales and the period of the fastest fluctuations, respectively. DNS requires tremendous computational resources and is presently not viable for practical application.

4.2.2 Averaged conservation equations

Turbulent flows consist of random fluctuations of various flow properties. A statistical approach introduced by Reynolds (1895) is adopted to establish the effects of turbulence on the mean flow. All flow quantities are expressed as the sum of mean and fluctuating components, i.e. $\phi = \Phi + \phi'$. Inserting this into the instantaneous conservation equations and averaging it yields the Reynolds-averaged Navier-Stokes (RANS) equations, viz.,

$$\frac{\partial U_i}{\partial x_i} = 0, \tag{4.7}$$

$$\rho\frac{\partial U_i}{\partial t} + \rho U_j\frac{\partial U_i}{\partial x_j} = -\frac{\partial P}{\partial x_i} + \frac{\partial}{\partial x_j}\big(2\mu S_{ji} - \rho\overline{u_j' u_i'}\big). \tag{4.8}$$

Owing to the non-linearity of the Navier-Stokes equation, the averaging process generates the quantity $-\rho\overline{u_i' u_j'}$. It is termed the Reynolds-stress tensor and is denoted by $\rho\tau_{ij}$. This tensor is symmetric with six independent components that are unknown. With three velocity components, pressure and six Reynolds

stresses, there are ten unknowns but only four PDEs resulting from Eqs. (4.7) and (4.8). This is known as the closure problem. In order to obtain a closed system of equations, additional equations are needed to relate the Reynolds-stress tensor with quantities of the mean flow. The process of obtaining such closure equations is termed turbulence modelling.

4.3 Turbulence Modelling

There is a multitude of closure theories aimed at correlating Reynolds stresses with mean flow properties. The field of turbulence modelling is vast and too extensive to cover here. Only a brief overview is provided. Attention is given to the models that proved promising in past studies involving flows with positive pressure gradients. Subsections 2.6.1 and 2.6.2 in the literature survey revealed that k-ε based two-equation turbulence models generally produce unsatisfactory results for swirling and non-swirling diffuser flows. Better results were reported with k-ω based models and the $\overline{v'^2}$-f model. Fair results were obtained with Reynolds-stress models (RSMs), but not good enough to warrant their usage.

Wilcox (1998: 23) lists the four primary categories of turbulence models, namely algebraic (or zero-equation) models, one-equation models, two-equation models, and stress-transport models. Even though zero- and one-equation models provide economic computations, they are not popular since their performance is generally inferior to more sophisticated models. However, the model of Spalart and Allmaras (1992) often provides satisfactory results for boundary layers and external aerodynamics. Since sufficient computational capacity was available for the current project, attention is given to more sophisticated eddy-viscosity models and stress-transport models.

4.3.1 Linear eddy-viscosity models

The majority of turbulence models are based on linear turbulent-viscosity models that assume proportionality between Reynolds stresses and mean rates of deformation. This assumption is known as the Boussinesq approximation, which reads

$$\tau_{ij} = -\overline{u_i' u_j'} = 2\nu_t S_{ij} - \frac{2}{3} k \delta_{ij}, \tag{4.9}$$

where ν_t is the turbulent viscosity (or eddy viscosity), S_{ij} the mean strain-rate tensor, k the turbulent kinetic energy per unit mass, and δ_{ij} the Kronecker delta ($\delta_{ij} = 1$ if $i = j$ and $\delta_{ij} = 0$ if $i \neq j$). After substituting Eq. (4.9) into Eq. (4.8), it is evident that the Boussinesq approximation, in essence, means that the vortices in turbulent flow enable more effective mixing, which is synonymous to an increased diffusion coefficient (Holzmann, 2017: 86).

The turbulent viscosity, ν_t, is unknown and depends on details of the flow field. Turbulence models using the eddy-viscosity approach thus no longer need to determine the Reynolds stresses, but rather the eddy-viscosity. From dimensional analysis, the kinematic turbulent viscosity ν_t (m^2/s) can be written in terms of a turbulent velocity scale ϑ_t (m/s), length scale ℓ_t (m), or time scale τ_t (s):

$$\nu_t = C_\mu \vartheta_t \ell_t = C_\mu \vartheta_t^2 \tau_t = C_\mu \ell_t^2 / \tau_t, \tag{4.10}$$

where C_μ is a dimensionless closure coefficient that can be constant ($C_\mu \approx 0.09$) or variable. Owing to the limitations of constant-coefficient turbulence models, more recent models tend to use strain-rate or vorticity dependent coefficients. The velocity, length and time scales in Eq. (4.10) are also unknown. They can, however, be estimated from known mean flow quantities using transport equations for turbulent quantities.

4.3.1.1 The *k*-ω model

Wilcox (1998: 119–122) provides the history of the k-ω model. The paper of Wilcox (1988) demonstrates that conventional k-ε and k-ω^2 formulations are generally inaccurate for boundary layers exposed to adverse pressure gradients and that wall functions tend to mask the shortcomings of these models. He postulated a two-equation model that is capable of accurately predicting boundary layer properties in adverse pressure gradients. Moreover, the model's closure coefficients require no viscous damping functions nor wall functions when integrated through the viscous sublayer. The ω-equation also has an exact boundary condition at the wall.

Wilcox (1993) did a convincing study where he compared the performance of six low-Reynolds-number k-ε models with two k-ω models for turbulent boundary layers with favourable, zero and adverse pressure gradients. In all the test cases, the k-ω model, with or without low-Reynolds-number modifications, outperformed the k-ε models. Almost identical results were obtained using either wall functions or integrating through the sublayer. Moreover, Wilcox (1993) demonstrated that the k-ε formulation is inconsistent with the well-established physical structure of the turbulent boundary layer. Low-Reynolds-number corrections cannot remedy this inconsistency.

Wilcox (1998) made amendments to the Wilcox (1988) model to improve its performance for free shear flows. He claims that the new formulation is as accurate as the Wilcox (1988) model for boundary layers, but its predictive accuracy for free shear flows significantly improved. This renders the Wilcox (1998) model suitable for both wall-bounded and free shear flows.

The eddy viscosity for the Wilcox (1998) model is computed with

$$\nu_t = k/\omega. \tag{4.11}$$

The transport equations for the turbulent kinetic energy and specific dissipation rate are given by

$$\frac{\partial k}{\partial t} + U_j \frac{\partial k}{\partial x_j} = \frac{\partial}{\partial x_j}\left[(\nu + \sigma^* \nu_t)\frac{\partial k}{\partial x_j}\right] + \tau_{ij}\frac{\partial U_i}{\partial x_j} - \beta^* k\omega, \tag{4.12}$$

$$\frac{\partial \omega}{\partial t} + U_j \frac{\partial \omega}{\partial x_j} = \frac{\partial}{\partial x_j}\left[(\nu + \sigma \nu_t)\frac{\partial \omega}{\partial x_j}\right] + \alpha\frac{\omega}{k}\tau_{ij}\frac{\partial U_i}{\partial x_j} - \beta\omega^2, \tag{4.13}$$

where τ_{ij} is computed with Eq. (4.9). The model's closure coefficients and auxiliary relations are available in Wilcox (1998: 121).

Wilcox (1988) deduced boundary conditions for his model using perturbation methods to analyse the viscous sublayer. Two follow from the "no-slip" condition so that

$$u = k = 0 \quad \text{at} \quad y^+ = 0, \tag{4.14}$$

where $y^+ \equiv u_\tau y/\nu$ and $u_\tau \equiv \sqrt{\tau_\mathrm{w}/\rho}$. Another condition arises from the fact that molecular diffusion and dissipation balance in one of the model's equations of motion for the viscous sublayer, i.e.,

$$\omega \to \frac{6\nu}{\beta_1 y^2} \quad \text{as} \quad y^+ \to 0. \tag{4.15}$$

Apsley and Leschziner (1999) explain why the k-ω model is more likely to predict separation in flows subject to adverse pressure gradients than the k-ε model: A universal transport equation for the k-ε and k-ω models can be written as

$$\frac{\partial \gamma}{\partial t} + U_j \frac{\partial \gamma}{\partial x_j} = \frac{\partial}{\partial x_j}\left[\left(\nu + \frac{\nu_t}{\sigma_\gamma}\right)\frac{\partial \gamma}{\partial x_j}\right] + \frac{\gamma}{k}(C_{\gamma 1} P_k - C_{\gamma 2}\varepsilon) + S_\gamma, \tag{4.16}$$

where γ represents either ε or ω. Equation (4.16) can always be written in terms of ε by expressing γ as a function of k and ε, viz.,

$$\gamma = a\varepsilon^m k^n. \tag{4.17}$$

Turbulence models of this kind can thus be interconverted, and the constants $C_{\gamma 1}$ and $C_{\gamma 2}$ can be transformed to $C_{\varepsilon 1}$ and $C_{\varepsilon 2}$, respectively. The shear stress is sensitive to the difference, $C_{\varepsilon 2} - C_{\varepsilon 1}$ (Apsley and Leschziner, 1999). This difference thus has a strong effect on the model's response to adverse pressure gradients and its prediction of separation. In the k-ω model, the difference is smaller than in the k-ε model. The turbulence dissipation rate is thus higher in the k-ω model, which means the turbulence intensity is lower. The k-ω model is thus more likely to predict separation in adverse pressure gradients. Conversely, it tends to overpredict the reattachment length in separated flows.

4.3.1.2 The $\overline{v'^2}$-f model

Durbin (1991) developed the $\overline{v'^2}$-f model for wall-bounded turbulent shear flows. He argued that near-wall turbulent flows could be divided into two regions: an inner region that scales on small viscous lengths and an outer region that scales on larger flow dimensions. The peak of turbulence energy and production are both within the inner region. It is thus indispensable to represent this region in order to accurately model wall-bounded turbulent flows.

The majority of turbulence closures are based on isotropic approximations. Near the wall, in the strongly anisotropic inner region, such models perform poorly. In an attempt to remedy this shortcoming, *ad hoc* damping functions are often introduced to adjust the turbulence model to fit experimental or computational data. Patel *et al.* (1985) argue that such modifications are somewhat arbitrary and lack sound physical basis. Moreover, Durbin (1993) explains that a model's damping function is valid only for a particular flow scenario. It is "fixed" and is, therefore, unable to respond to dramatic changes in turbulence quantities. Damping functions are also generally non-linear, which causes numerical stiffness.

Durbin (1991) disliked the idea of using a fundamentally incorrect model that is "corrected" with arbitrary damping functions. Therefore, he aimed to develop a turbulence closure that can model near-wall flow by solving partial differential equations (PDEs) rather than using damping functions. He explains that the blocking effect of solid boundaries primarily suppresses the normal component of turbulence intensity. Therefore, if one approximates the eddy viscosity as

$$\nu_t = C_\mu \overline{v'^2} \tau_t, \tag{4.18}$$

with $\overline{v'^2}$ as the wall-normal turbulence velocity, *ad hoc* damping functions are unnecessary. According to Durbin (1991), blocking is associated with image vorticity, which is governed by an elliptic PDE. Non-homogeneous effects of turbulence can thus be incorporated using an elliptic model.

Lien and Kalitzin (2001) showed that the no-slip boundary condition for the elliptic function in the original model is ill-defined in laminar and transitional regions. This gives rise to numerical instability when using decoupled solvers. Therefore, they modified the original model to make it more robust. The model equations presented below are for this "code-friendly" version, with a limit imposed on the turbulent viscosity, as suggested by Davidson *et al.* (2003).

The $\overline{v'^2}$-f model uses the Boussinesq approximation, i.e. Eq. (4.9), and the eddy viscosity defined in Eq. (4.18). The turbulent time scale is given by

$$\tau_t = \min\left\{ \max\left[\frac{k}{\varepsilon}, 6\sqrt{\frac{\nu}{\varepsilon}} \right], \frac{0.6k}{\sqrt{6} C_\mu \overline{v'^2} S} \right\} \tag{4.19}$$

and the turbulent length scale is given by

$$\ell_t = C_L \max\left\{\min\left[\frac{k^{3/2}}{\varepsilon}, \frac{k^{3/2}}{\sqrt{6}C_\mu \overline{v'^2} S}\right], C_\eta\left(\frac{\nu^3}{\varepsilon}\right)^{1/4}\right\}, \tag{4.20}$$

where S is the magnitude of the mean strain-rate tensor, $S = \sqrt{S_{ij}S_{ji}}$. These turbulence scales are computed from the standard k-ε equations, viz.,

$$\frac{\partial k}{\partial t} + U_j \frac{\partial k}{\partial x_j} = \frac{\partial}{\partial x_j}\left[\left(\nu + \frac{\nu_t}{\sigma_k}\right)\frac{\partial k}{\partial x_j}\right] + P_k - \varepsilon, \tag{4.21}$$

$$\frac{\partial \varepsilon}{\partial t} + U_j \frac{\partial \varepsilon}{\partial x_j} = \frac{\partial}{\partial x_j}\left[\left(\nu + \frac{\nu_t}{\sigma_\varepsilon}\right)\frac{\partial \varepsilon}{\partial x_j}\right] + \frac{1}{\tau_t}(C_{\varepsilon 1}P_k - C_{\varepsilon 2}\varepsilon). \tag{4.22}$$

The transport equation for the turbulent stress normal to streamlines, $\overline{v'^2}$, is given by

$$\frac{\partial \overline{v'^2}}{\partial t} + U_j \frac{\partial \overline{v'^2}}{\partial x_j} = \frac{\partial}{\partial x_j}\left[\left(\nu + \frac{\nu_t}{\sigma_k}\right)\frac{\partial \overline{v'^2}}{\partial x_j}\right] + kf - 6\overline{v'^2}\frac{\varepsilon}{k}, \tag{4.23}$$

where kf is the source of $\overline{v'^2}$. It represents the redistribution of turbulence intensity from the streamwise component. Non-local effects of turbulence are accounted for by an elliptic relaxation function,

$$\ell_t^2 \frac{\partial^2 f}{\partial x_j^2} - f = \frac{1}{\tau_t}\left[(C_1 - 6)\frac{\overline{v'^2}}{k} - \frac{2}{3}(C_1 - 1)\right] - C_2\frac{P_k}{k}. \tag{4.24}$$

The model's closure coefficients can be found in Lien and Kalitzin (2001). All the coefficients are independent of the non-dimensional wall distance, y^+, which is not the case for most k-ε based low-Reynolds-number models.

Davidson *et al.* (2003) argued that the wall-normal stress should be the smallest of the normal stresses near walls, i.e. $\overline{v'^2} \leq \overline{u'^2}$ and $\overline{v'^2} \leq \overline{w'^2}$. Consequently, $\overline{v'^2}$ must be smaller than $2k/3$. In the model of Lien and Kalitzin (2001), the Laplacian term is assumed to be negligibly small in the homogeneous region far from solid boundaries, i.e. $\partial^2 f/\partial x_j^2 \to 0$. Equation (4.24) then reduces to

$$f_{\text{hom}} = -\frac{1}{\tau_t}\left[(C_1 - 6)\frac{\overline{v'^2}}{k} - \frac{2}{3}(C_1 - 1)\right] + C_2\frac{P_k}{k}. \tag{4.25}$$

It turns out that the Laplacian term is, in fact, not negligible far from walls, which causes $\overline{v'^2}$ to become too large so that $\overline{v'^2} > 2k/3$. Therefore, Davidson *et al.* (2003) set an upper bound on the source term, kf, of Eq. (4.23) so that

$$kf = \min\left[kf, kf_{\text{hom}}\right]. \tag{4.26}$$

This limit ensures that $\overline{v'^2} \leq 2k/3$. In regions where $\overline{v'^2} \approx 2k/3$, the turbulent viscosity calculated with Eq. (4.18) is $\nu_t = 0.147k^2/\varepsilon$, which is significantly larger than the normal k-ε value of $\nu_t = 0.09k^2/\varepsilon$. Davidson *et al.* (2003) thus limited the turbulent viscosity as follows:

$$\nu_t = \min\left[0.09k^2/\varepsilon, 0.22\overline{v'^2}\tau_t\right]. \tag{4.27}$$

With the above modifications, the $\overline{v'^2}$-f model produces more physical results and is more stable numerically. The "no-slip" boundary conditions simplify to

$$k = \overline{v'^2} = f = 0 \quad \text{and} \quad \varepsilon = 2\nu k/y^2 \quad \text{as} \quad y \to 0. \tag{4.28}$$

4.3.2 Hybrid eddy-viscosity models

Hybrid eddy-viscosity models combine eddy-viscosity models to take advantage of the strengths of the individual models while avoiding their shortcomings. The shear-stress-transport (SST) k-ω model of Menter (1994) is probably the most renowned hybrid model. It is a combination of the k-ω and k-ε models. The k-ω model performs well in near-wall flows, but Menter (1992) demonstrated that it is highly sensitive to the inlet freestream ω-value; the k-ε model is not sensitive to the latter, but integration to the wall is challenging. Menter (1994) thus introduced a blending interpolation parameter which leans towards the k-ω model near solid boundaries and towards the k-ε model in the far-field. A modification to the eddy viscosity has been introduced to the SST k-ω model, which is based on the philosophy of Johnson and King (1985). That is, the transport of the principal turbulent shear stress is of vital importance when solving strong adverse pressure gradients. The SST model is thus not a pure eddy-viscosity model but incorporates features of a Reynolds-stress model.

4.3.3 Non-linear models

While models based on the isotropic Boussinesq approximation provide accurate results for many practical flows, they fail to accurately solve flows with sudden changes in mean strain rate, high curvature, rotation, boundary layer separation, or body forces (Wilcox, 1998: 274). The two primary approaches to resolve the limitations of the Boussinesq approximation are to use non-linear constitutive relations or stress-transport models (Wilcox, 1998: 329). The former is appropriate for flows in which the anisotropy of the normal Reynolds stresses is essential; the latter solves transport equations for each Reynolds stress and thus naturally accounts for the shortcomings of the Boussinesq assumption (Wilcox, 1998: 283–284). However, despite the sophistication of these models, they do not necessarily provide superior results compared to normal two-equation models (Apsley and Leschziner, 1999).

Rodi (1976) deduced a non-linear constitutive equation by simplifying the full Reynolds-stress equation (given by Eq. (4.29) in the following subsection). He assumed that the sum of the convective and diffusive terms of the Reynolds stresses are proportional to the sum of the convective and diffusive terms of the turbulent kinetic energy. Introducing this simplification into the Reynolds-stress transport equation with suitable approximations for the dissipation tensor, ε_{ij}, and pressure-strain tensor, Π_{ij}, results in a non-linear algebraic stress model (ASM). Although ASMs incorporate the anisotropy of Reynolds stresses, they do not necessarily perform better than the standard k-ε model and they can suffer from stability issues (Versteeg and Malalasekera, 2007: 95). Therefore, the development of non-linear eddy-viscosity models enjoyed more attention.

The idea behind non-linear eddy-viscosity models is to account for Reynolds-stress transport and anisotropy. The Boussinesq approximation assumes that the specific Reynolds-stress tensor is proportional to the mean strain-rate tensor, turbulent quantities, and density, i.e. $-\overline{u_i u_j} = \tau_{ij}(S_{ij}, k, \varepsilon, \rho)$. This implies that turbulence instantaneously adjusts as it convects through the flow field. In reality, turbulence lags behind the rapid changes that disturb the balance between turbulence production and dissipation (Versteeg and Malalasekera, 2007: 95). Reynolds stresses are transported quantities that depend on rates of change, convective and diffusive redistribution as well as turbulence production and dissipation. Therefore, Speziale (1987) proposed a k-ε model that includes Oldroyd derivatives to partially account for Reynolds-stress transport. Non-linear models are often developed to adhere to the physical properties of the exact Navier-Stokes equation, such as coordinate and dimensional invariance, the realisability constraint of Lumley (1979), and material-frame indifference.

4.3.4 Stress-transport models

Stress-transport models, also known as second-order or second-moment closure models, attempt to solve the exact Reynolds-stress transport equation. The latter is a set of PDEs describing the behaviour of the specific Reynolds-stress tensor, $\tau_{ij} = -\overline{u_i' u_j'}$, which takes the following form:

$$\frac{\partial \tau_{ij}}{\partial t} + U_k \frac{\partial \tau_{ij}}{\partial x_k} = P_{ij} + \varepsilon_{ij} - \Pi_{ij} + D_{ij}, \tag{4.29}$$

where P_{ij} denotes the turbulence production term, ε_{ij} the dissipation rate term, Π_{ij} the pressure-strain redistribution term, and D_{ij} the diffusion term. According to Wilcox (1998: 284), such models naturally account for streamline curvature, sudden changes in strain rate, secondary motions, and the like. However, they do not guarantee superior performance, and they are computationally expensive to solve. That is because they need to solve six PDEs for the independent Reynolds stresses, and they are slow to converge.

In order to close Eq. (4.29), models are required for the dissipation rate, pressure-strain redistribution, and diffusion terms. The dissipation rate, ε_{ij}, is often modelled using the Kolmogorov (1941) hypothesis of local isotropy for the small dissipative eddies. Since dissipation is anisotropic in reality, Hanjalić and Launder (1976) accounted for it by incorporating the Reynolds-stress anisotropy tensor, $a_{ij} = \overline{u_i' u_j'} - \frac{2}{3} k \delta_{ij}$, and a low-Reynolds-number damping function that varies with the turbulent Reynolds number, $Re_t = k^2/(\varepsilon\nu)$.

The turbulence transport or diffusion term, D_{ij}, involves pressure fluctuations and triple products of velocity fluctuations. Traditionally, no attempt is made to model the pressure fluctuations since it cannot be measured with accuracy. DNS data support that the influence of pressure fluctuations is negligible (Wilcox, 1998: 286). The remainder of the diffusion term is typically modelled assuming a gradient transport process: Daly and Harlow (1970) assumed $D_{ij} \propto \partial \tau_{ij}/\partial x_k$, but this does not account for the rotational invariance of D_{ij}. Donaldson (1972) added terms to correct the symmetry issue, but the dimensionality was incorrect. Finally, Launder *et al.* (1975) introduced a scalar closure coefficient and multiplied by k^2/ε to ensure that the tensor is dimensionally correct and rotationally invariant.

The pressure-strain tensor, Π_{ij}, is critical to model representatively, but extremely challenging to do so. Its significance lies in the fact that it is of the same order of magnitude as the production term; its difficulty to model is due to the vast number and complexity of possible correlations (Wilcox, 1998: 287). The pressure fluctuations, p', in an incompressible flow are represented by a Poisson equation which can be solved with appropriate Green's functions. The most well-known model of this kind is the LRR model of Launder, Reece and Rodi (1975) with the optional wall-reflection term of Gibson and Launder (1978). The SSG model of Speziale, Sarkar and Gatski (1991) is another popular Reynolds-stress model and does not require wall-reflection corrections.

4.4 Fan/Stator Modelling

Actuator disc modelling refers to the modelling of the flow in the vicinity of turbomachinery blading without explicitly modelling the blades or blade passages (Louw, 2015: 16). Engelbrecht (2018) developed the actuator disc model (ADM) that was used in this study. He wrote a steady-state solver for the extended actuator disc model (EADM) of Van der Spuy (2011), which is based on Thiart and Von Backström's (1993) ADM. The model was developed for fans, but it can be used for stationary blades (stators) as well. Relative velocities and flow angles then become absolute velocities and flow angles, respectively.

The ADM requires three identical axially aligned discs in the vicinity of the fan/stator that are each one cell thick. Bredell (2005: 33) found the best results when placing the upstream and downstream discs approximately half a chord length away from the actuator disc. Figure 4.1 depicts this concept.

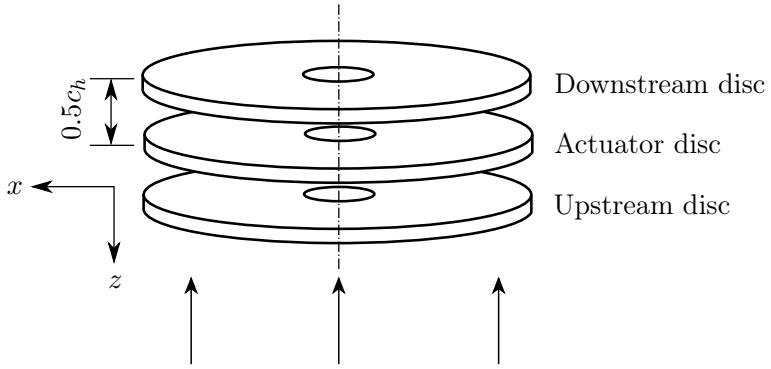

Figure 4.1: Computational discs required by ADM (Engelbrecht, 2018: 23)

The paper of Thiart and Von Backström (1993) provides the equations required for modelling flow in the vicinity of a fan. Since stator blades are stationary, these equations are presented in the absolute frame of reference. Figure 4.2 depicts the relevant velocity vectors, angles and forces. The lift and drag forces are determined with

$$\delta L = \tfrac{1}{2}\rho u_{\mathrm{m}}^2 C_L c_h \delta r, \tag{4.30}$$

$$\delta D = \tfrac{1}{2}\rho u_{\mathrm{m}}^2 C_D c_h \delta r. \tag{4.31}$$

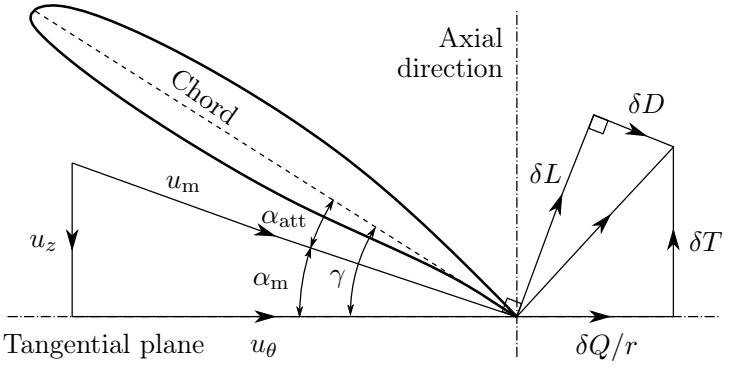

Figure 4.2: Two-dimensional blade element
(adapted from Thiart and Von Backström (1993))

The lift and drag data in Eqs. (4.30) and (4.31) were obtained using a uniform velocity field. The velocity field at the fan/stator contains swirl and hence reduces the validity of these data. To address this issue, Meyer and Kröger (2001) found that using the average velocity upstream and downstream of

the actuator disc, u_{m}, provides better results than using only the upstream free-stream velocity vector.

The thrust, δT, and torque, δQ, exerted by the blade element on the fluid are obtained by decomposing the lift and drag forces into axial and circumferential components, viz.,

$$\delta T = \delta L \cos \alpha_{\mathrm{m}} - \delta D \sin \alpha_{\mathrm{m}}, \tag{4.32}$$

$$\delta Q = (\delta L \sin \alpha_{\mathrm{m}} + \delta D \cos \alpha_{\mathrm{m}}) r. \tag{4.33}$$

For these blade forces to be expressed as momentum sources or sinks in the Navier-Stokes equations, they need to be expressed as per unit volume forces. The volume is obtained by taking the number of blades and axial "thickness", Δ, of the actuator disc into account, viz.,

$$\frac{\partial T}{\partial V} = \frac{n_b \delta T}{2\pi r \delta r \Delta} = \frac{\sigma \delta T}{c_h \delta r \Delta}, \tag{4.34}$$

$$\frac{\partial Q}{\partial V} = \frac{n_b \delta Q}{2\pi r \delta r \Delta} = \frac{\sigma \delta Q}{c_h \delta r \Delta}. \tag{4.35}$$

Substituting Eqs. (4.30) to (4.33) into Eqs. (4.34) and (4.35) yield the final form of the source terms:

$$\frac{\partial T}{\partial V} = \frac{1}{2} \rho u_{\mathrm{m}}^2 \frac{\sigma}{\Delta} (C_L \cos \alpha_{\mathrm{m}} - C_D \sin \alpha_{\mathrm{m}}), \tag{4.36}$$

$$\frac{\partial Q}{\partial V} = \frac{1}{2} \rho u_{\mathrm{m}}^2 \frac{\sigma}{\Delta} (C_L \sin \alpha_{\mathrm{m}} + C_D \cos \alpha_{\mathrm{m}}) r. \tag{4.37}$$

The ADM assumes radial forces to be negligibly small so that $\partial F_r / \partial V = 0$.

To resolve Eqs. (4.36) and (4.37), lift and drag data for the selected aerofoil profile are required. For a range of Mach numbers, the lift and drag characteristics of an aerofoil profile are a function of the Reynolds number and angle of attack (Meyer and Kröger, 2001). McGhee and Beasley (1979) gathered experimental data for the NASA-LS 0413 profile and plotted lift and drag coefficients as a function of angle of attack for a range of Reynolds numbers. They varied the angle of attack from $-10°$ to $20°$ for Reynolds numbers ranging from 2×10^6 to 9×10^6. For angles of attack beyond stall, Thiart and Von Backström (1993) used the empirical correlations of Hoerner (1965) and Hoerner and Borst (1985): Beyond stall, the blade element behaves like a flat plate in separated flow, in which case the lift and drag coefficients are described by

$$C_L = C_{D\max} \sin \alpha_{\mathrm{att}} \cos \alpha_{\mathrm{att}}, \tag{4.38}$$

$$C_D = C_{D\max} \sin^2 \alpha_{\mathrm{att}}, \tag{4.39}$$

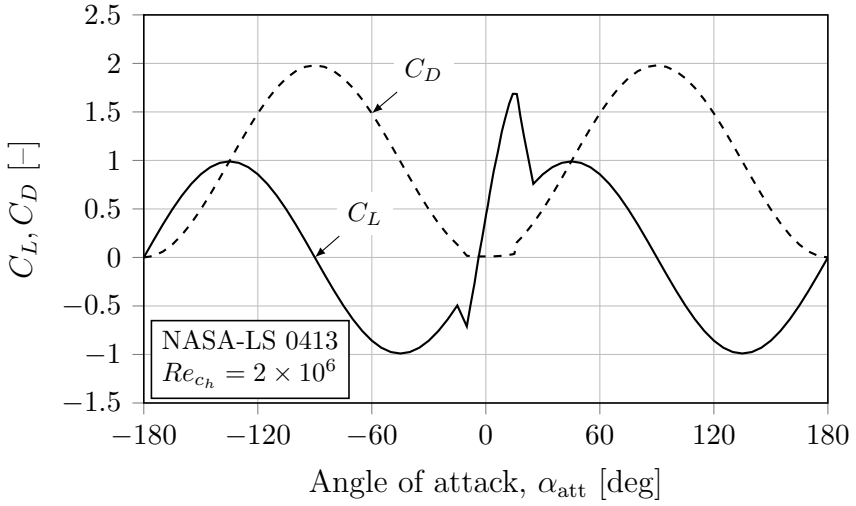

Figure 4.3: NASA-LS 0413 profile lift and drag characteristics at $Re_{c_h} = 2 \times 10^6$ (adapted from Engelbrecht (2018: 25))

where $C_{D\max} = 1.98$ when the plate is perpendicular to the flow direction. Figure 4.3 exemplifies lift and drag characteristics that are used in the fan/stator model. Linear interpolation and extrapolation are used to determine the lift and drag characteristics at other Reynolds numbers.

The extended actuator disc model (EADM) of Van der Spuy (2011) improves on the ADM at low flow rates by augmenting the lift and drag characteristics at low flow rates where radial flow is present. The EADM extends the linear section of the lift characteristic curve for radial stations above a specified radius ratio at low flow rates (see Subsection 2.6.4 for more on this). Subsequently, the drag coefficient is adjusted proportionally to the increase in lift coefficient.

4.5 Conclusions

The equations governing all fluid flow problems are provided in Section 4.2, and the closure problem is explained in Subsection 4.2.2. Section 4.3 covers various turbulence modelling strategies. It includes linear, hybrid, and non-linear eddy-viscosity models as well as stress-transport models. In Subsection 4.3.1, attention is given to the two-equation k-ω model of Wilcox (1998) and the four-equation $\overline{v'^2}$-f model of Durbin (1991). That is because the literature in Subsections 2.6.1 and 2.6.2 illustrated that good results had been reported with these models in flows involving adverse pressure gradients. Finally, the modelling equations for the extended actuator disc model are outlined in Section 4.4.

Chapter 5

Validation Study

5.1 Introduction

The physical size of air-cooled condenser fans often renders full-scale testing impractical. The number of outlet configurations that needs to be tested for the M-fan is also too extensive for a scaled-down experimental investigation. Therefore, computational fluid dynamics (CFD) was used to simulate the different discharge configurations for the M-fan (see the following chapter). Prior to those simulations, a representative test case with published experimental data was used to validate the CFD. The modelling strategies that provided the most accurate results were then extrapolated to the M-fan simulations.

5.2 ERCOFTAC Conical Diffuser

The experimental results of Clausen *et al.* (1993) were selected for the validation study. They took measurements of a swirling boundary layer developing in a conical diffuser with an included angle of 20° and an area ratio of 2.84. This test case has become known as the ERCOFTAC conical diffuser and is shown in Fig. 5.1. The inlet swirl was sufficient to prevent boundary layer separation but insufficient to cause recirculation at the centreline. The swirl was generated using a rotating cylinder with a honeycomb screen near its inlet. It produced a near solid-body rotation with a relatively uniform axial velocity in the core region at the diffuser inlet. The average inlet axial velocity was $U_0 = 11.6\,\mathrm{m/s}$ and the inlet swirl number was $W_{\max}/U_0 = 0.59$, where $W_{\max}$ is the maximum circumferential velocity at the diffuser inlet. The diffuser discharged into the open atmosphere. Measurements were taken in traverses normal to the wall, as shown in Fig. 5.1. Mean velocity measurements were measured using single wire hot-wire anemometers, with an estimated error of 2 %. Reynolds stresses were measured with an X-wire probe, with an estimated error of 10 %. Static pressures at the wall were measured with wall taps.

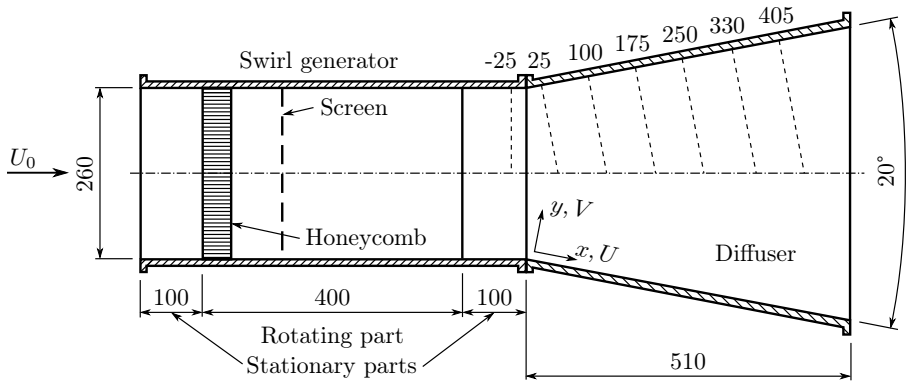

Figure 5.1: ERCOFTAC conical diffuser with measurement traverses (adapted from Armfield *et al.* (1990))

5.3 Past Studies

Several numerical studies have been performed on the ERCOFTAC test case (Armfield and Fletcher, 1989; Armfield *et al.*, 1990; Cho and Fletcher, 1991; Rodi *et al.*, 1995; Gyllenram and Nilsson, 2006; Bonous, 2008; Nilsson *et al.*, 2008; Dhiman *et al.*, 2011; From *et al.*, 2017). Armfield and Fletcher (1989) and Cho and Fletcher (1991) demonstrated that algebraic stress models (ASMs) outperform k-ε models, especially for the prediction of the peaks in near-wall velocity and turbulence quantities. Armfield *et al.* (1990) obtained good predictions of the mean flow and turbulence quantities using an ASM and a k-ε model with a two-layer wall function.

Bonous (2008) and Nilsson *et al.* (2008) found that the standard k-ε and SST k-ω models produce similar velocity profiles but different turbulent kinetic energy profiles. The results indicate that solutions obtained with both models are sensitive to the specified inlet turbulence quantities (Bonous, 2008: 48). The turbulence dissipation rate data in the ERCOFTAC database were generated using a turbulence intensity of 10 % and a viscosity ratio of $\mu_t/\mu = 14.5$ at the inlet. Substantial improvement was seen when an inlet turbulence viscosity ratio of $\mu_t/\mu = 27.3$ was used instead. Further, they found that the order of accuracy of the discretisation scheme influences solutions. Results were found to be insensitive to the linear solver and cross-sectional grid topology.

Dhiman *et al.* (2011) compared the performance of different RANS turbulence models. They tested the standard, realisable and RNG k-ε turbulence models with a two-layer wall function, the SST k-ω model, and an RSM. The standard k-ε model and RSM performed well overall, and the RNG k-ε and SST k-ω models performed poorly. All the models, however, underestimated the near-wall streamwise velocity and overpredicted it near the centreline. From *et al.* (2017) used a k-ω baseline-explicit algebraic-stress model (BSL-EASM) in their simulations. They reported excellent results, especially near the diffuser walls.

5.4 Computational Setup

The geometry used for the validation study was inspired by Gyllenram and Nilsson (2006). Since velocity and Reynolds-stress data are available at the diffuser inlet, the inlet extension they used was neglected. The contracted extension after the dump was also discarded. With it present, it was challenging to obtain converged solutions. The majority of the simulations were run as two-dimensional axisymmetric problems using wedge-shaped meshes. The wedge angle was set to five degrees, as advised by the OpenFOAM user manual (Greenshields, 2017: 141). Figure 5.2 depicts the computational domain.

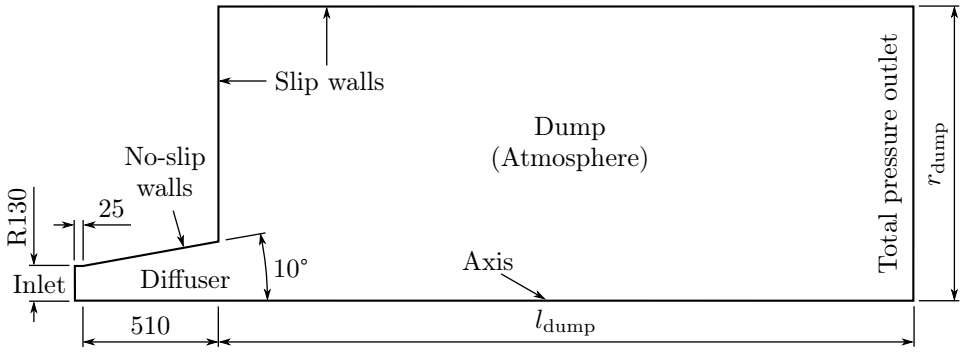

Figure 5.2: Computational domain for ERCOFTAC conical diffuser

OpenFOAM's built-in mesh generation utility, `blockMesh`, was used to generate hexahedral meshes. The meshes were parametrised using `m4` scripts. Initially, the realisable k-ε turbulence model with wall function was used. Velocity and turbulent kinetic energy profiles at the inlet ($x = -25\,\text{mm}$) were interpolated from the experimental measurements of Clausen *et al.* (1993) using `groovyBC`. This boundary condition requires the OpenFOAM extension, `swak4Foam`. The inlet turbulence dissipation rate was computed with

$$\varepsilon = \frac{C_\mu k^2}{\nu(\mu_t/\mu)}, \tag{5.1}$$

where $\nu = 1.5 \times 10^{-5}$ is the kinematic viscosity of air and $\mu_t/\mu = 14.5$ is the turbulent viscosity ratio initially used by Bonous (2008). Note that the standard constant coefficient of $C_\mu = 0.09$ was assumed at the inlet for all k-ε based models, even though this might not be true for the respective models—it is, for example, not constant in the realisable version (see Shih *et al.* (1995)). A zero-gradient condition was set for the inlet pressure boundary condition.

The boundary conditions for the stationary casing before the diffuser and diffuser walls were set to no-slip for velocity. Zero gradients were specified for pressure and turbulent kinetic energy. The `epsilonWallFunction` and `nutkWallFunction` wall functions were used for turbulence dissipation and

turbulent viscosity, respectively. Liu (2016) provides an in-depth explanation of these wall functions. The boundary conditions for the dump were set to slip for velocity and zero-gradient for the remaining variables. At the outlet, Neumann boundary conditions of zero were specified for velocity and turbulence quantities. A Dirichlet boundary condition equal to zero was used for pressure.

OpenFOAM's steady-state solver for incompressible turbulent flows was used for most simulations. It makes use of the semi-implicit method for pressure-linked equations (SIMPLE) algorithm for pressure-velocity coupling. The discretisation schemes rely on standard Gaussian finite-volume integration, which interpolates values from cell centres to face centres. Central differencing was used for all gradient schemes. The bounded variant of the second-order linear-upwind scheme was used for the advection of velocity. The advection of scalar fields was discretised with a bounded limited-linear scheme that limits towards the upwind scheme in regions of rapid change. Laplacian terms were discretised using linear interpolation for the diffusion coefficient and the corrected scheme for surface-normal gradients. The latter is a second-order scheme that allows for mesh non-orthogonality up to approximatively 70°. Simulations we deemed converged when the normalised residual for all equations reached at least 10^{-5} and the pressure difference between the outlet and inlet settled to a constant value.

5.5 Grid Dependence Study

A grid dependence study is an essential part of all high-quality CFD studies. The solution of the underlying partial differential equations (PDEs) emerges through the process of sequentially refining the mesh until grid independence is achieved. That is, key flow properties do not change as the computational grid is refined beyond a certain point.

For the grid dependence study, the dump length and radius were fixed at ten diffuser inlet diameters and five diffuser outlet radii, respectively. Table 5.1 provides the details of the successively refined meshes. The wall static pressure coefficient and flow profiles at the $x = 330\,\mathrm{mm}$ traverse are plotted in Fig. 5.3. The wall static pressure coefficient is calculated with

$$C_{p\mathrm{w}} = \frac{p_\infty - p_{\mathrm{sw}}(x)}{\rho U_0^2/2}, \tag{5.2}$$

where $p_{\mathrm{sw}}(x)$ is the static pressure along the diffuser wall and p_∞ is the static pressure at the domain outlet, which was set equal to zero. The overall static pressure coefficient of the diffuser, C_p, can be determined by replacing $p_{\mathrm{sw}}(x)$ with p_{si} in Eq. (5.2). The latter represents the area-weighted average of the static pressure at the domain inlet.

Table 5.1: Details of meshes used in grid dependence study

Grid identifier	Number of nodes	Average diffuser y^+	C_p [–]	Difference [%]
Grid 1	13 040	114.755	0.927	4.497
Grid 2	26 110	74.600	0.949	2.186
Grid 3	52 160	47.838	0.963	0.736
Grid 4	104 565	31.827	0.970	–
Grid 5	208 640	21.799	0.975	0.474

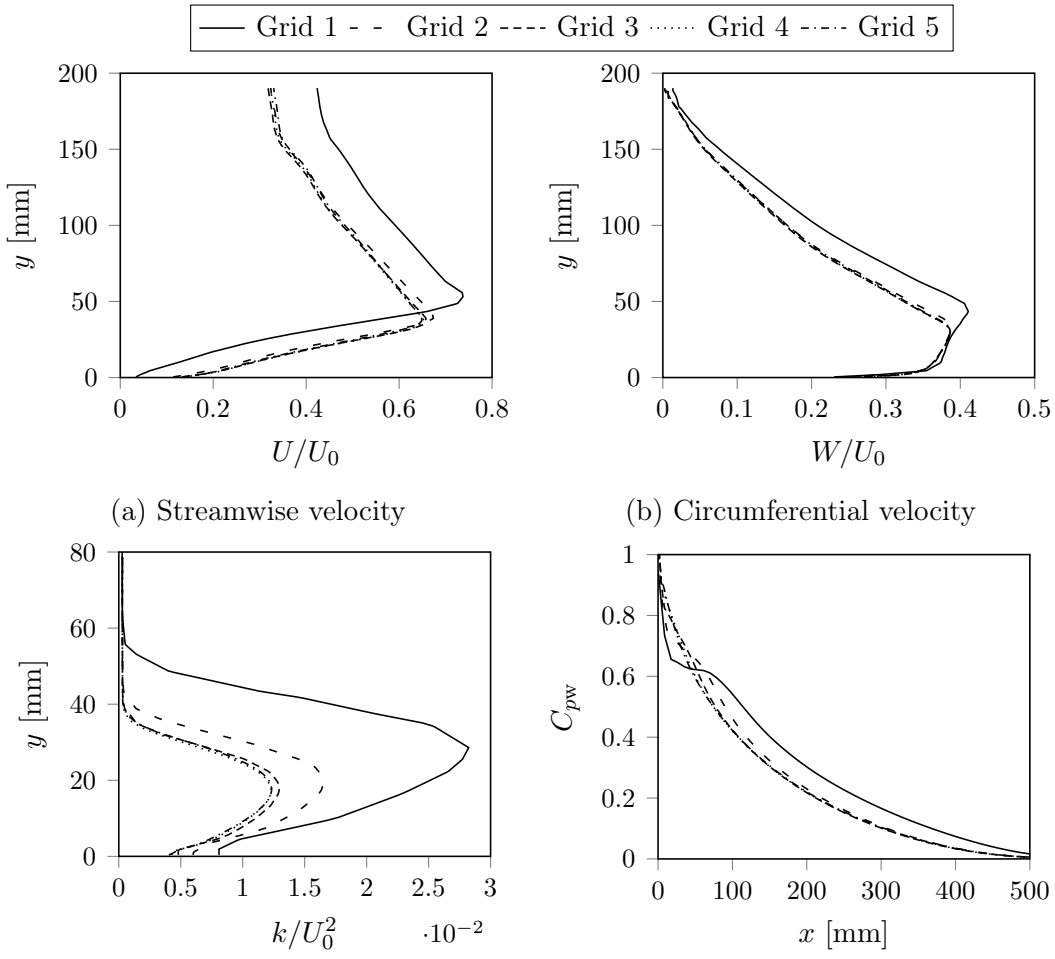

(a) Streamwise velocity

(b) Circumferential velocity

(c) Turbulent kinetic energy

(d) Wall static pressure coefficient

Figure 5.3: Flow profiles at the $x = 330\,\text{mm}$ traverse and wall static pressure coefficient for successively refined meshes

From Table 5.1 and Fig. 5.3 it is evident that results started to stabilise at Grid 3: The pressure difference is within one per cent of the next finer mesh. The profiles for Grids 3, 4 and 5 are similar. However, for Grid 4, the y^+-values at the diffuser wall lie within the range of 29.57 to 35.49—close to the desired value of 30. There is also a slight improvement in the turbulent kinetic energy profile compared to Grid 3. Note that the wall-adjacent grid points in Grid 5 fall within the buffer layer ($5 < y^+ < 30$), which should always be avoided. Therefore, Grid 4 was selected (and used as reference value in Table 5.1). It was used for all high-Reynolds-number computations in the validation study.

5.6 Boundary Distance Effects

The dump in Fig. 5.2 represents the open atmosphere. The size of this dump should be large enough to ensure that the results in the diffuser are not affected by the boundaries of the dump. As zero gradients were prescribed for velocity and turbulence quantities at the outlet, the flow needs to stabilise before it reaches the outlet boundary. Versteeg and Malalasekera (2007: 283) state that the outlet boundary should be located at least ten heights downstream of the last flow obstacle. Therefore, an initial dump length of ten inlet diffuser diameters was selected, i.e. $l_{\text{dump}} = 10 d_{\text{difi}}$. Gyllenram and Nilsson (2006) used a dump diameter of three diffuser outlet diameters. To be more conservative, an initial dump radius of five outlet diffuser radii was chosen, i.e. $r_{\text{dump}} = 5 r_{\text{difo}}$.

Grid 4 (see the previous section) was used for the boundary distance sensitivity study. In order to find a suitable dump length, the length was varied while the dump radius was fixed at five diffuser outlet radii. Similarly, the dump radius was varied while its length was fixed at ten inlet diffuser diameters in search of a suitable dump radius. Figure 5.4 illustrates the sensitivity of the diffuser static pressure coefficient to the dump length and radius.

From Fig. 5.4 (note the fine ordinate scale) it is evident that the diffuser pressure coefficient is relatively insensitive to the length and radius of the dump. The pressure coefficient varies by less than a per cent for all the lengths considered. However, velocity gradients existed close to the outlet boundary for $l_{\text{dump}}/d_{\text{difi}}$ equal to four and six. Therefore, a dump length equal to eight diffuser inlet diameters was selected. The results seem to stabilise for a dump radius equal to five diffuser outlet radii. Subsequently, $l_{\text{dump}}/d_{\text{difi}} = 8$ and $r_{\text{dump}}/r_{\text{difo}} = 5$ were deemed satisfactory. The flow and turbulence quantities are essentially independent of the dump length and radius. Profiles are, therefore, not provided.

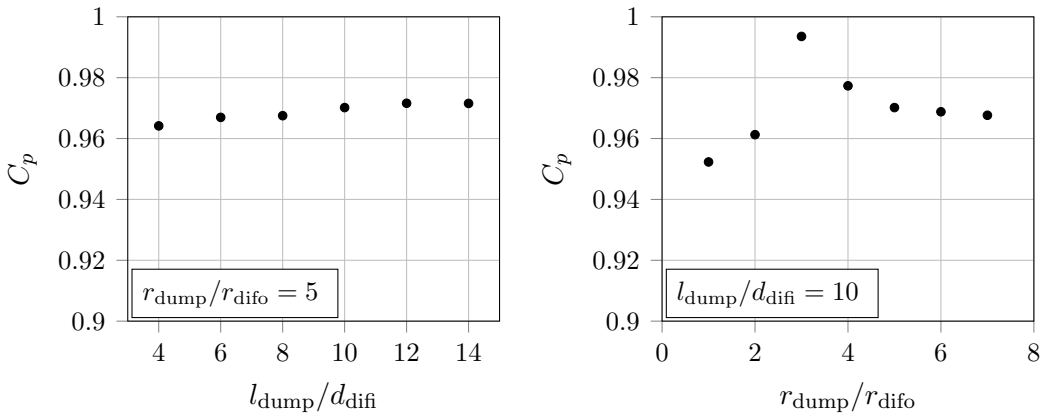

(a) Dump length effect

(b) Dump radius effect

Figure 5.4: Effects of the dump length and radius on the static pressure coefficient of the diffuser

5.7 Sensitivity to Inlet Turbulence Quantities

Clausen *et al.* (1993) provide velocity and turbulence kinetic energy profiles at the inlet of the domain. The profile for the remaining turbulence equation must be calculated. Turbulence dissipation can be approximated with

$$\varepsilon = \frac{C_\mu^{3/4} k^{3/2}}{\ell_t} \quad \text{or} \quad \varepsilon = \frac{C_\mu k^2}{\nu(\mu_t/\mu)}. \tag{5.3}$$

Bonous (2008) initially assumed an inlet turbulence intensity of 10 % and a turbulent viscosity ratio of $\mu_t/\mu = 14.5$. He obtained better results when he used $\mu_t/\mu = 27.3$. Gyllenram and Nilsson (2006) also used a turbulence intensity of 10 % but used a turbulent length scale of 3.2 mm. The latter is equal to the cell size of the honeycomb in the swirl generator.

In this validation study, it was deemed more accurate to use the inlet turbulent kinetic energy profile of Clausen *et al.* (1993) instead of a constant turbulence intensity. Both viscosity ratios of Bonous (2008) were used, namely 14.5 and 27.3, as well as the $\ell_t = 3.2$ mm length scale of Gyllenram and Nilsson (2006) to compute the inlet turbulence dissipation profile with Eq. (5.3).

From Fig. 5.5 it is clear that solutions are affected by the specified inlet turbulence conditions. Using an inlet turbulent length scale equal to the honeycomb cell size yields results that compare the closest with the experimental measurements. The rationale behind this length scale also makes sense. Therefore, this length scale was selected to compute the inlet turbulence quantities.

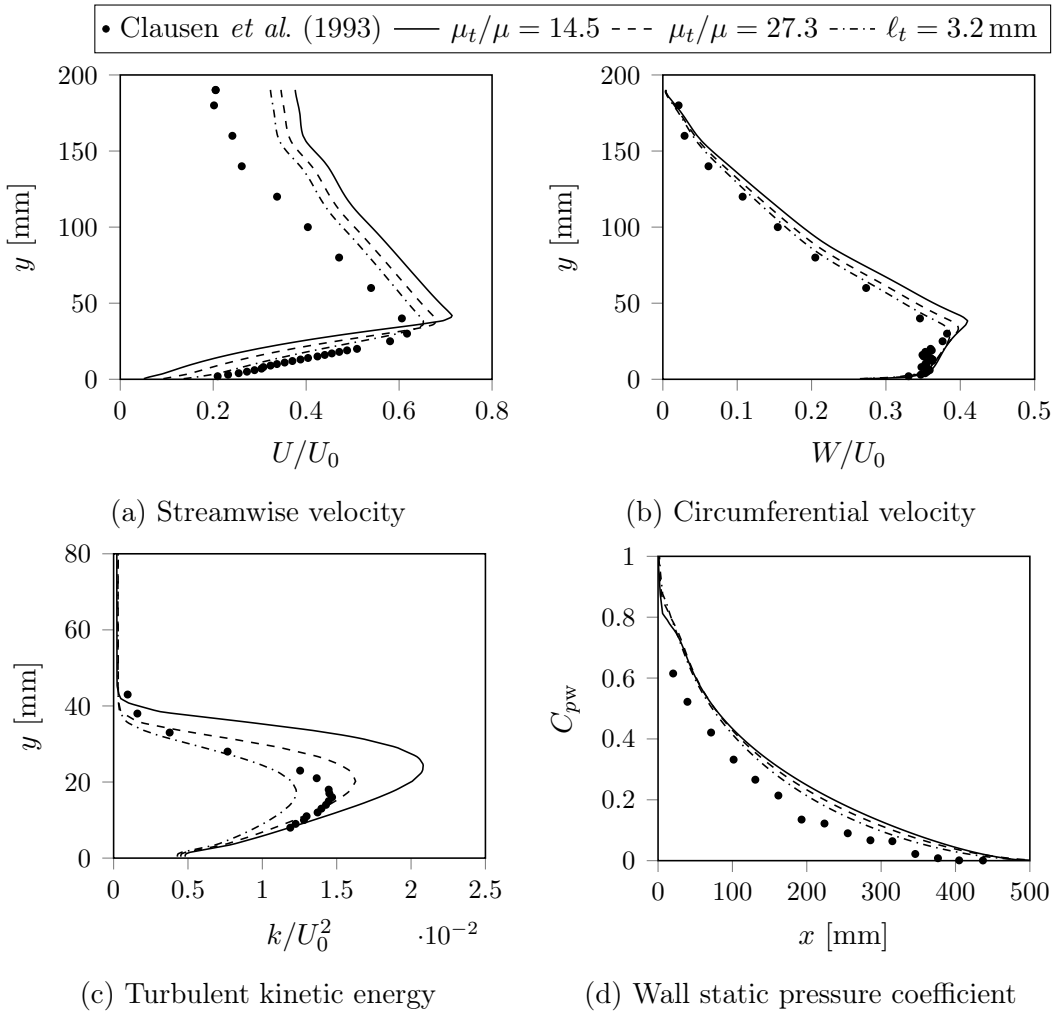

(a) Streamwise velocity

(b) Circumferential velocity

(c) Turbulent kinetic energy

(d) Wall static pressure coefficient

Figure 5.5: Flow profiles at the $x = 330\,\text{mm}$ traverse and wall static pressure coefficient for different inlet turbulence conditions

5.8 Turbulence Models

Thus far, the realisable k-ε turbulence model was used for all simulations. It was selected as an initial model since most of the more recent studies at Stellenbosch University on axial flow fans and ACCs employed it (Van der Spuy, 2011; Louw, 2015; Wilkinson, 2017; Engelbrecht, 2018). That is because the realisable version generally outperforms the standard k-ε model, especially when swirl is present (Shih *et al.*, 1995).

The literature survey suggested that k-ω based models or the $\overline{v'^2}$-f model might perform well for the current flow problem. Nevertheless, various turbulence models were tested to see which ones compare favourably with the experimental measurements of Clausen *et al.* (1993). The dimensionless distance from the wall for high-Reynolds-number models was kept in the order of $y^+ \sim 30$,

and $y^+ \sim 1$ for the low-Reynolds-number models. A grid dependence study was done using the low-Reynolds-number k-ε model of Launder and Sharma (1974) for y^+-values slightly above and below unity. Results were found to be insensitive to subtle refinement and coarsening of the near-wall grid clustering.

High-Reynolds-number computations utilised wall functions. The tested k-ε based models included Launder and Spalding's (1974) standard model, the realisable model of Shih *et al.* (1995), the RNG version of Yakhot *et al.* (1992), and Shih *et al.*'s (1993) quadratic model. The standard k-ω model of Wilcox (1998) and SST variant of Menter (1994) were tested. The LRR (Launder, Reece and Rodi, 1975) and SSG (Speziale, Sarkar and Gatski, 1991) RSMs were also tested. These closure models produced the streamwise velocity and turbulent kinetic energy profiles at the last measuring traverse ($x = 405\,\text{mm}$) shown in Fig. 5.6. The standard k-ω model compares the closest with the velocity measurements. However, it underestimates the near-wall spike in turbulent kinetic energy. The SST k-ω model performs surprisingly poor, which agrees with the findings of Dhiman *et al.* (2011).

The tested low-Reynolds-number models included the k-ε models of Launder and Sharma (1974) (LS k-ε) and the cubic non-linear version of Lien *et al.* (1996) (LC k-ε). The wall-integrated standard and SST k-ω models were tested. Finally, the modified four-equation $\overline{v'^2}$-f model of Lien and Kalitzin (2001) were implemented. Figure 5.7 presents the profiles obtained with these models. Again, the k-ω model predicts the velocity well and underestimates the near-wall turbulent kinetic energy. The SST k-ω model performs poorly.

It is difficult to make a conclusive statement as to which of the tested turbulence models performs the best. The k-ω model, with or without wall functions, predicts the flow well: Its streamwise and circumferential velocity profiles compare well with the measurements. Wall static pressures are predicted slightly better than the other models (not shown). However, the near-wall turbulent kinetic energy is underestimated. Generally, k-ε models predict the near-wall turbulent kinetic energy better. They also provide comparable velocity and pressure results. However, Subsections 2.6.1 and 2.6.2 demonstrated that such models typically fail when applied to boundary layers in adverse pressure gradients. Wall functions are also generally not applicable in adverse pressure gradients, and damping functions lack sound physical basis. Therefore, it was decided to avoid k-ε models. Stress-transport models do not show any clear advantage in this case. The $\overline{v'^2}$-f model provides better kinetic energy profile predictions, but slightly worse velocity and pressure predictions. Ultimately, the wall-integrated k-ω turbulence model was selected for future computations. Wall and damping functions are thus avoided. This model typically predicts separation before k-ε models would (see Subsection 4.3.1). It will thus yield more conservative designs when applied to diffuser design.

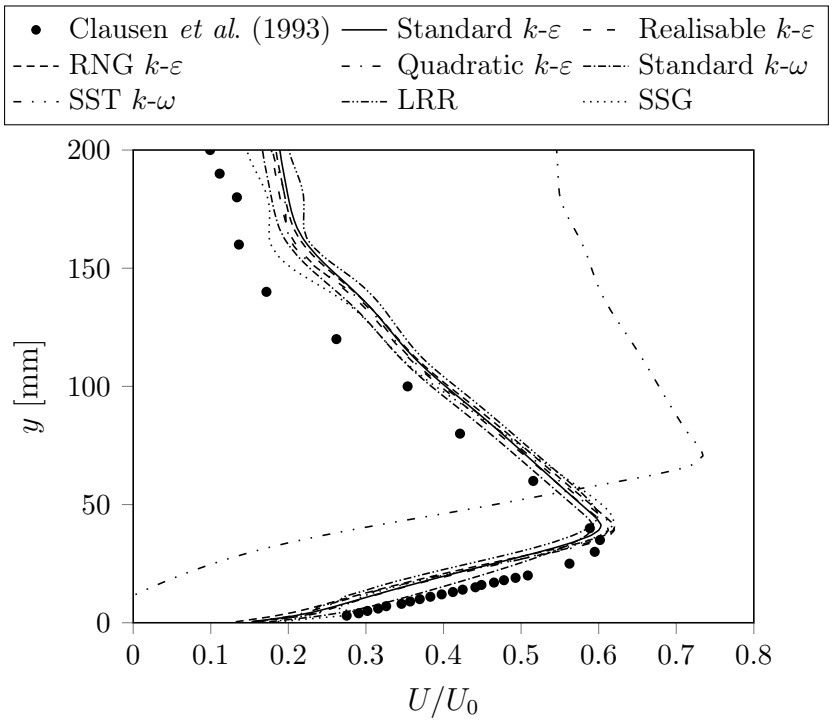

(a) Streamwise velocity

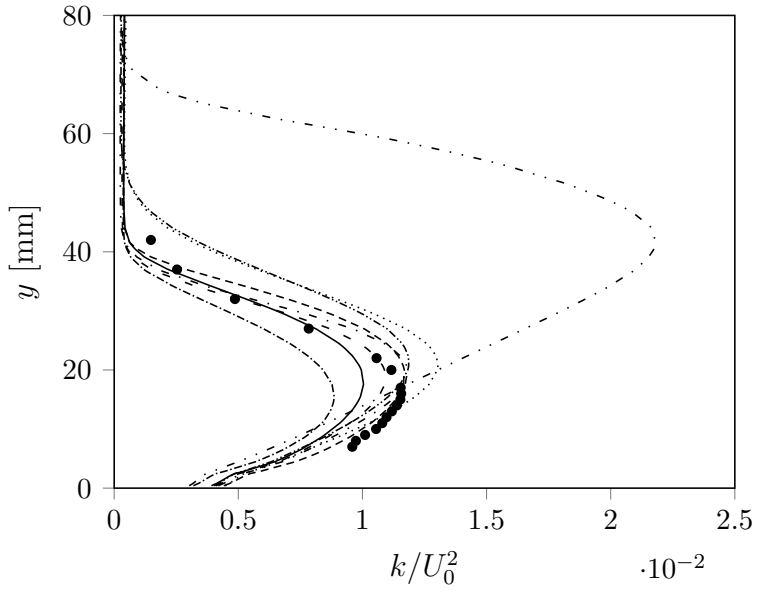

(b) Turbulent kinetic energy

Figure 5.6: Flow profiles at the $x = 405\,\text{mm}$ traverse for different high-Reynolds-number turbulence models

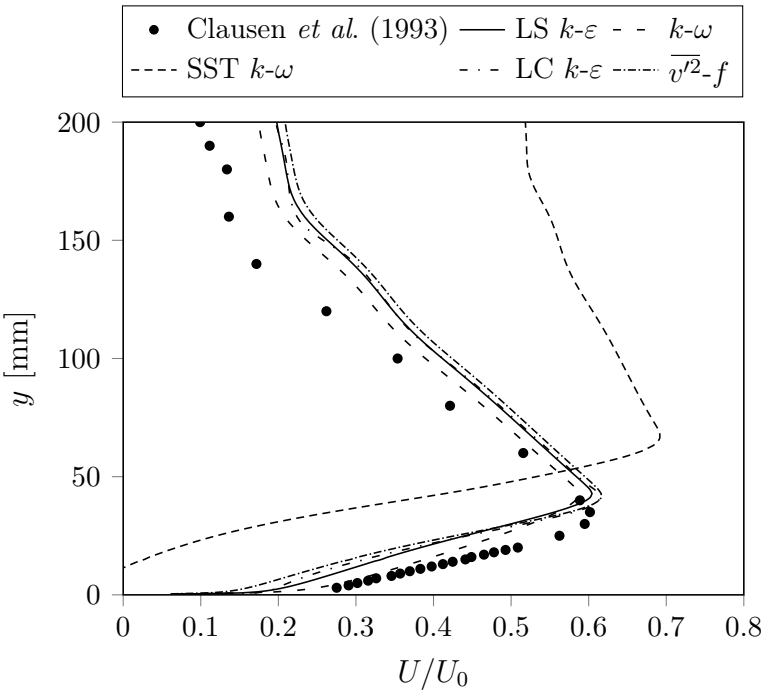

(a) Streamwise velocity

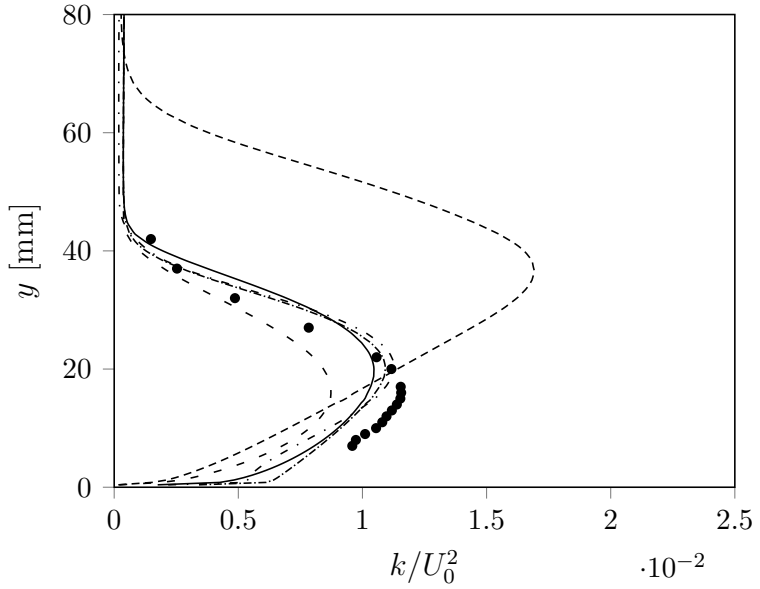

(b) Turbulent kinetic energy

Figure 5.7: Flow profiles at the $x = 405\,\text{mm}$ traverse for different low-Reynolds-number turbulence models

5.9 Transient and Three-Dimensional Effects

According to Stewart *et al.* (2013), adverse pressure gradients may cause asymmetries or disturbances in both computational and experimental data. However, McDonald *et al.* (1971) found that the flow inside unstalled diffusers with swirling inlet flow was symmetric within experimental error. This finding suggests that the flow inside the ERCOFTAC conical diffuser should be axisymmetric. Notwithstanding, Dhiman *et al.* (2011) reported substantial improvement in the wall static pressure coefficient and velocity profile predictions within the ERCOFTAC diffuser using a three-dimensional approach as opposed to a two-dimensional axisymmetric approach.

An investigation was, therefore, performed to determine whether an axisymmetric condition eliminates physical aspects of the problem. Steady-state and transient simulations were performed to test for time-dependence as well. Convergence was challenging to achieve ($\sim 10^{-3}$) for the transient simulations and the time step needed to be extremely small ($\sim 10^{-5}$) for the low-Reynolds-number meshes.

Figure 5.8 illustrates that transient and three-dimensional effects are insignificant. The best wall static pressure coefficients are, in fact, obtained assuming steady-state conditions on a two-dimensional axisymmetric mesh. However, this is probably due to the improved level of convergence ($\sim 10^{-5}$) achieved for the steady-state simulations. Therefore, steady-state axisymmetric simulations were deemed sufficient.

5.10 Conclusions

The experimental results of Clausen *et al.* (1993) were used to validate the computational fluid dynamics. Their experiment involved swirling flow in a conical diffuser, which is discussed in Section 5.2. Previous numerical studies on this particular diffuser are briefly outlined in Section 5.3. The computational setup is discussed in Section 5.4. It includes details of the computational domain, mesh, boundary conditions, solvers, and discretisation practices. Section 5.5 contains a grid dependence study: A high-Reynolds-number grid with 104 565 nodes and $y^+ \sim 30$ produced grid-independent solutions. The effects of the boundary distances are examined in Section 5.6: The outlet boundary should be located eight inlet diffuser diameters downstream of the diffuser discharge plane. The dump, which represents the open atmosphere, requires a radius equal to five times the diffuser outlet radius. Section 5.7 demonstrates that solutions are sensitive to the inlet length scale and viscosity ratio used to compute the turbulence dissipation: A turbulent length scale equal to the honeycomb cell size, i.e. 3.2 mm, gave good results. An appropriate turbulence model is identified in Section 5.8: No model clearly outperformed the rest, but the wall-integrated

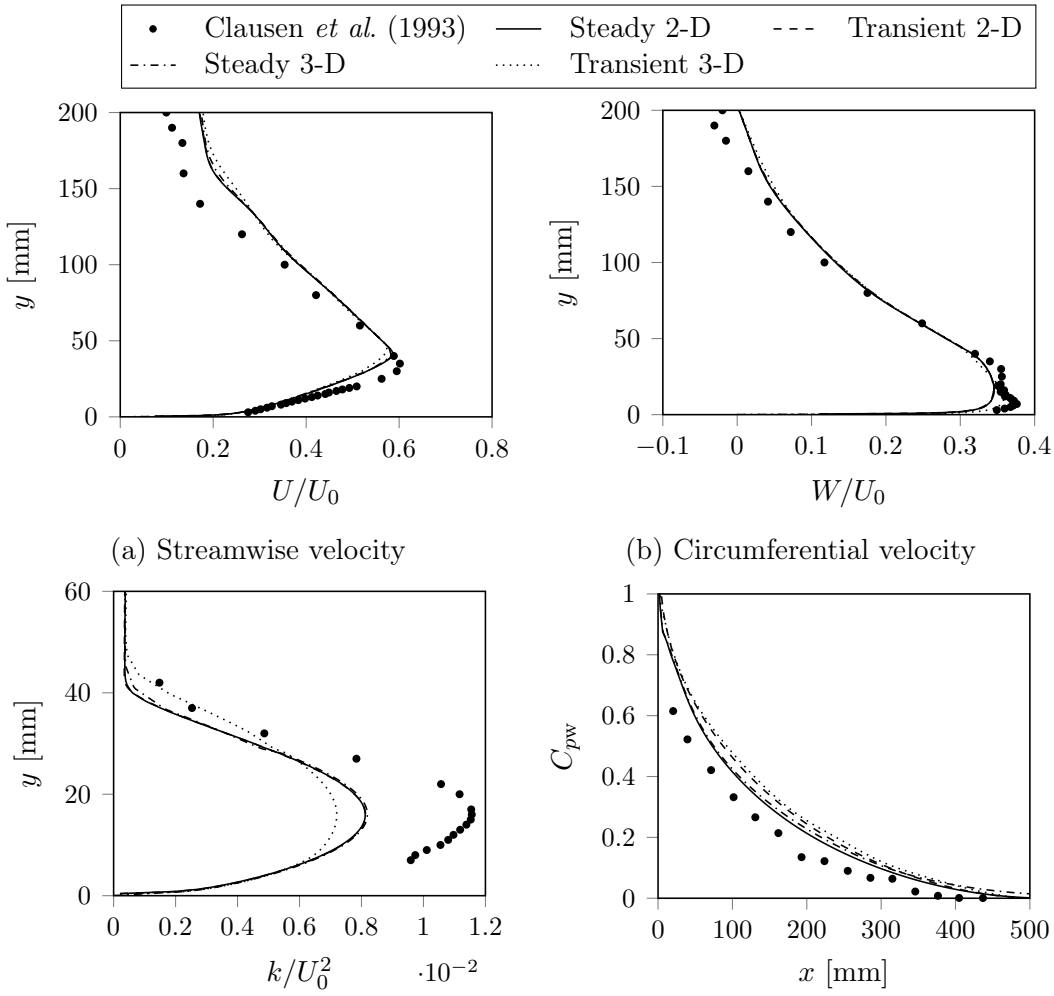

(a) Streamwise velocity

(b) Circumferential velocity

(c) Turbulent kinetic energy

(d) Wall static pressure coefficient

Figure 5.8: Flow profiles at the $x = 405\,\text{mm}$ traverse and wall static pressure coefficient for steady-state and transient simulations on two-dimensional axisymmetric and three-dimensional meshes

standard k-ω model produced satisfactory results. Finally, time dependence and three-dimensionality are investigated in Section 5.9: Steady-state axisymmetric simulations performed just as well as transient three-dimensional simulations.

Chapter 6

M-Fan Discharge Configurations

6.1 Introduction

Diffusers, stators, or a combination of these can be used to convert a portion of the dynamic pressure loss to static pressure—hence the term pressure recovery. Pressure recovery increases the mechanical energy available to the air in the fan system, which raises the fan static pressure characteristic curve. Pressure recovery will thus tend to shift the operating point of a given fan system to a higher volumetric flow rate.

This chapter considers various outlet configurations for the M-fan. That is, the addition of a stator, a conical diffuser with and without a stator at its inlet, an annular diffuser with and without a stator at its inlet, and an annular diffuser with a stator at its outlet. The aim is to find the configuration that provides the highest pressure recovery at the design flow rate, and that is robust to off-design conditions.

As a start, parametric studies were conducted to find the diffuser geometries that yield maximum pressure recovery at the design flow rate. Fixed inlet velocity profiles were used for this. Thereafter, the best performing geometries of the individual cases were tested at off-design flow rates. Finally, the pressure recoveries of the overall highest performing discharge configuration were added to the characteristics of the M-fan to obtain the combined characteristics of the fan-diffuser unit.

6.2 Computational Setup

The geometries and meshing strategies were similar to those used in the validation study (see Section 5.4), i.e. wedge-shaped two-dimensional axisymmetric meshes with hexahedral and prism cells. Since the wall-integrated k-ω turbu-

lence model was selected, integration through the viscous sublayer was achieved using a densely clustered layer of width $0.05r_{\text{FC}}$ at no-slip boundaries so that $y^+ \sim 1$. Again, a large dump represented the free discharge to the open atmosphere.

The inlet of the computational domain started at the outlet of the M-fan. The fan itself was thus not modelled. Fixed velocity and turbulence profiles at the fan outlet were used to specify the inlet boundary conditions. These profiles were obtained from Wilkinson (2017: 70–72), who provides outlet velocity profiles of the M-fan at flow rates ranging from 265 to 385 m^3/s. The profiles were measured from the hub to the tip of a periodic three-dimensional CFD model, approximately 0.1 m downstream of the aerofoil trailing edge at the hub. Since the validation study proved that results are sensitive to the specified inlet turbulence quantities (see Section 5.7), profiles for k and ε were obtained from Wilkinson himself. The exact inlet profiles were thus used instead of estimated turbulence intensities and length scales. Turbulence dissipation was converted to turbulence frequency using $\omega = \varepsilon/(\beta^* k)$, where $\beta^* = 0.09$ (Wilcox, 1988). A zero Neumann boundary condition was set for pressure at the inlet.

The duct wall following the fan casing and diffuser walls were modelled as no-slip boundaries. A zero-gradient condition for pressure and a fixed value of zero for turbulent kinetic energy were specified at these walls. The turbulent specific dissipation within the viscous sublayer was determined with $\omega = 6\nu/(\beta_1 y^2)$, where $\beta_1 = 0.075$ (see Eq. (4.15)). The turbulent viscosity was set equal to zero at the no-slip walls.

Slip boundaries were specified for the dump and fan hub walls. That is because no mechanical energy losses are expected at the walls of the dump. Also, the exact shape of the fan hub is not known and the near-wall flow there is unimportant. Since the solver deals more easily with slip walls compared to no-slip walls, the former was used for the hub. Zero gradients were assumed for pressure and turbulence quantities at these slip boundaries.

A total pressure of zero was specified as outlet boundary condition along with zero gradients for velocity and turbulence quantities. The front and rear planes of the domain were set to wedge boundaries, which is how OpenFOAM deals with two-dimensional axisymmetric problems. The sharp edge of the wedge was specified as a symmetry boundary, but this was merely a placeholder.

The kinematic viscosity and density of air at 20 °C were used in all simulations, i.e. $\nu \approx 1.5 \times 10^{-5}$ and $\rho \approx 1.2\,\text{kg}/\text{m}^3$, respectively. Steady-state simulations for incompressible turbulent flows were performed. For simulations involving stators, the solver written by Engelbrecht (2018) was used. It incorporates the EADM (discussed in Section 4.4) into a steady-state incompressible solver

for turbulent flows. These solvers achieve pressure-velocity coupling using the SIMPLE algorithm. Simulations generally ran for 50 000 to 100 000 iterations to reach residuals in the order of 10^{-5} to 10^{-6}. The area-weighted average of pressure at the inlet was also monitored. If it stabilised by the time the residuals reached the mentioned values, the solution was deemed converged.

OpenFOAM's discretisation practices are generally based on standard Gaussian finite-volume integration: It sums values on cell faces that were interpolated from cell centres (Greenshields, 2017: 118). Gradient schemes were discretised using the second-order central-differencing scheme. The bounded variants of the second-order linear-upwind scheme and first-order upwind scheme were used for the advection of velocity and turbulence quantities, respectively. Laplacian terms were discretised using linear interpolation for the diffusion coefficient and the limited-corrected scheme with a stabilising coefficient of 0.33 for surface-normal gradients. The latter scheme offers improved stability, but reduced accuracy, compared to the normally recommended corrected scheme (Greenshields, 2017: 124). The high aspect ratio wall-adjacent cells near the diffuser exit made convergence with the corrected scheme challenging. The limited scheme, however, made convergence possible.

Sensitivity to grid density and boundary distances were tested for the different outlet configurations. Details hereof are available in Appendices C and D, respectively. These sensitivity studies employed the standard k-ω turbulence model with wall functions. After the grid that resolves the mean flow and the boundary distances that do not affect key results have been found, grid clustering was added to facilitate integration through the boundary layer. Final results were then obtained with fully resolved boundary layers. The results presented below are thus grid and boundary-distance independent.

6.3 Downstream Stator

McKenzie (1997: 24) advises to use a stator if the flow angle at the rotor outlet is larger than 15° and smaller than 45°. For the M-fan, the minimum and maximum flow angles occur at the tip and hub, i.e. 20° and 44°, respectively. The M-fan may thus benefit from a stator.

Figure 6.1 depicts the computational domain that was used for the stator simulations. Note the discs that are required by the extended actuator disc model (EADM). As advised by Bredell (2005: 33), the upstream and downstream discs are located half a mean stator chord length from the actuator disc. The stator was designed following the design methodology outlined in Appendix B. The velocity profiles at the M-fan outlet were used as inlet velocity profiles to the stator. The resulting stator has nine blades with a mean chord length of $c_{h\mathrm{m}} = 1.286\,\mathrm{m}$. Wallis (1983: 291) recommends straightener vanes to be

located at least half a rotor blade chord downstream of the blade trailing edge to minimise interference noise. This is approximately where Wilkinson *et al.* (2017) measured their outlet velocity profiles. Therefore, the upstream disc of the EADM is located right at the inlet of the domain.

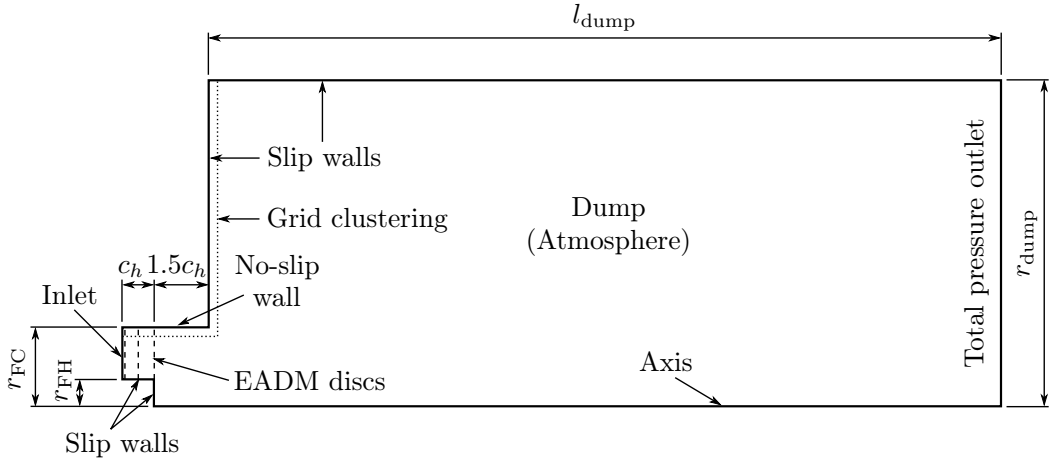

Figure 6.1: Computational domain used for downstream stator simulations

Solutions are proved to be independent of the mesh density and boundary distances in Appendices C and D, respectively. Key results did not change after the dump reached a size of $l_{\text{dump}}/d_{\text{FC}} = 18$ and $r_{\text{dump}}/r_{\text{FC}} = 13$. Grid clustering at no-slip boundaries facilitated integration through the viscous sublayer. The final mesh had 1 533 362 nodes with $y^+ \sim 1$ at the walls of interest. Figure 6.2 illustrates that the EADM solver with the designed stator effectively removed the swirl from the flow while hardly affecting the axial velocity profile. The stator caused a pressure rise of 11.302 Pa at the design flow rate, which translates to a pressure recovery coefficient of $K_{\text{rec}} = 0.316$.

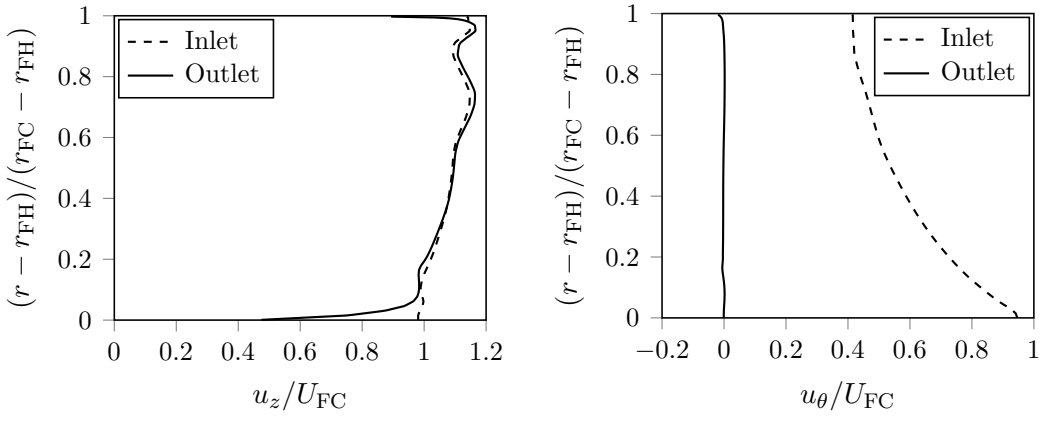

(a) Axial velocity (b) Circumferential velocity

Figure 6.2: Velocity profiles at the inlet and outlet of the stator

6.4 Conical Diffuser

Senoo *et al.* (1978) reported good performance with a conical diffuser having a total divergence angle of $2\theta = 8°$. The highest pressure recovery was obtained with an inlet free-vortex swirl intensity in the order of $S_\mathrm{i} = 0.10$ to 0.12. Recirculation at the centreline started when $S_\mathrm{i} = 0.18$. The swirl intensity at the outlet of the M-fan is approximately equal to 0.3, which is high compared to the results of Senoo *et al.* (1978). Reverse core flow is thus probable if a conical diffuser is to be installed downstream of the M-fan.

Hill *et al.* (1963) found that wake-type distortions caused by upstream flow obstructions may lead to diffuser stall if the pressure gradient is large enough. Raj and Lakshminarayana (1973) reported velocity defects in the downstream wakes caused by aerofoils up to three-quarter chord lengths. Therefore, it was decided to locate the inlet of the diffuser two mean stator chord lengths downstream of the M-fan. This axial clearance is ample to avoid rotor wakes entering the diffuser. However, the wake following the fan hub will probably still enter the conical diffuser and affect its performance negatively. Figure 6.3 is a schematic of the computational domain.

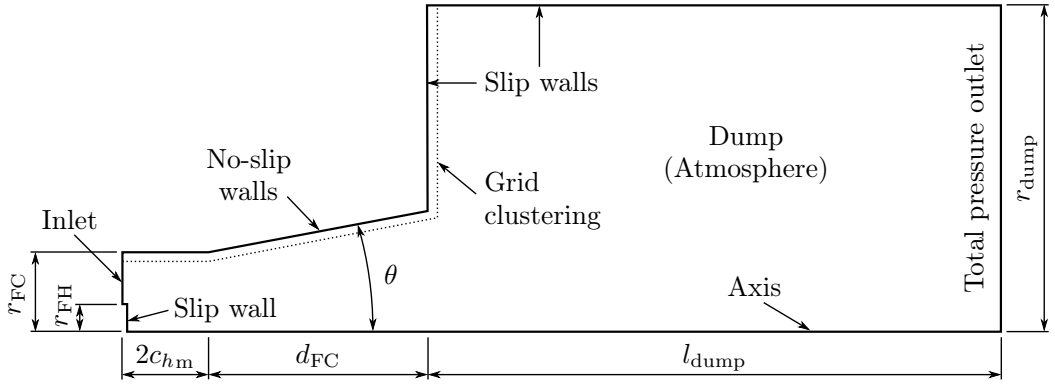

Figure 6.3: Computational domain used for conical diffuser simulations

Solutions became independent of the dump boundaries when it reached a size of $l_\mathrm{dump}/d_\mathrm{FC} = 14$ and $r_\mathrm{dump}/r_\mathrm{FC} = 8$ (see Appendix D). A parametric study was performed in search of the diffuser geometry that provides the highest pressure recovery. Wall angles within the range of $0° \leq \theta \leq 20°$ were tested in increments of one degree. The axial length of the diffuser was held constant at one fan diameter. Figure 6.4 depicts the results in the form of a pressure recovery coefficient versus area ratio plot. For these diffusers, the area ratio is defined as the total area at the diffuser outlet divided by the area of the fan annulus, i.e. $AR = A_\mathrm{difo}/\Delta A_\mathrm{F}$. These simulations were performed on grid-independent meshes with 807 003 nodes (see Appendix C).

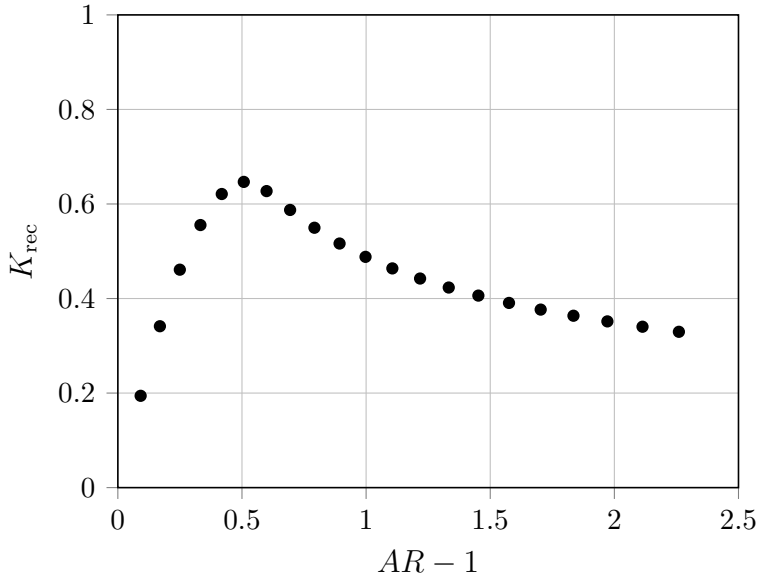

Figure 6.4: Variation of pressure recovery coefficient with area ratio for conical diffusers

There is a pronounced maximum of $K_{\text{rec}} = 0.647$ at an area ratio of 1.507 (or included angle of $2\theta = 10°$). This pressure recovery coefficient is two times higher than the value reported in the previous section with a stator only. Included angles of 8° and 12° provide pressure recoveries within five per cent of the maximum, and 14° within ten per cent of the maximum. The range of area ratios providing high pressure recoveries is thus quite narrow.

6.5 Conical Diffuser with a Stator at its Inlet

Swirl angles up to approximately ten degrees may aid diffuser performance (see Subsection 2.4.5). However, it was mentioned earlier that the swirl at the outlet of the M-fan is higher than this, which may be detrimental for diffuser performance. A stator was thus added between the fan outlet and diffuser inlet to remove the swirl before it enters the diffuser. The leading edge of the stator was located at a half mean rotor chord length downstream of the M-fan (thus at the inlet of the domain), and the trailing edge was located at 1.5 mean stator chord lengths upstream of the diffuser. According to the findings of Raj and Lakshminarayana (1973), stator wakes are not expected to influence diffuser performance.

The same computational domain as in Section 6.4 was used, but EADM discs were added at the inlet to represent the stator. Grid independence is proved in Appendix C and the final mesh had 1 114 632 grid points with strong grid clustering near the walls to resolve the boundary layer. Results became

independent of the dump boundaries when it reached a size of $l_{\text{dump}}/d_{\text{FC}} = 16$ and $r_{\text{dump}}/r_{\text{FC}} = 10$ (see Appendix D). A parametric study was performed for the same range of diffuser wall angles, i.e. $0° \leq \theta \leq 20°$. The results are displayed in Fig. 6.5.

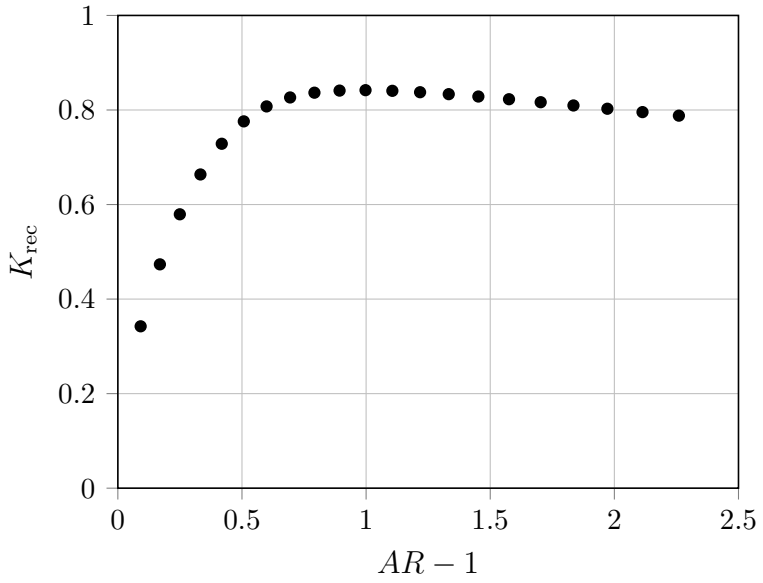

Figure 6.5: Variation of pressure recovery coefficient with area ratio for conical diffusers with a stator at their inlets

In this case, the highest pressure recovery coefficient, i.e. $K_{\text{rec}} = 0.842$, occurs at an area ratio of 1.998 (or included angle of $2\theta = 20°$). This maximum is far less pronounced than the one in the previous section for conical diffusers with inlet swirl. The pressure recoveries reported here are also considerably higher and diffuser performance is less sensitive to area ratio. Included angles in the range of 16° to 24° perform within one per cent of the maximum reported value, and the wider range of 12° to 36° is still within five per cent of the maximum.

However, the observed insensitivity to area ratio and elevated pressure recoveries will most probably change as the outlet velocity profiles of the M-fan change due to a shift in operating point. The diffuser of area ratio 1.792 ($2\theta = 16°$) yielding a recovery of $K_{\text{rec}} = 0.837$ is recommended: Its performance is essentially the same as the highest reported value and the reduced wall angle is preferred as it translates to decreased wall surface area and hence costs.

6.6 Annular Diffuser

The geometry of an annular diffuser is expressed in terms of its length, inner and outer wall angles, and inlet radius ratio. In this case, the inlet radius ratio

coincides with the hub-to-tip ratio of the M-fan and the length is equal to the fan diameter. These simulations were performed using the computational domain in Fig. 6.6. With dump boundary distances of $l_{\mathrm{dump}}/d_{\mathrm{FC}} = 16$ and $r_{\mathrm{dump}}/r_{\mathrm{FC}} = 8$, and a mesh of approximately 900 000 cells, results proved to be grid and boundary-distance independent (see Appendices C and D).

A parametric study was performed for various combinations of diffuser hub and casing wall angles: The hub wall angle was varied within the range of $0° \leq \theta_{\mathrm{H}} \leq 30°$ in increments of two degrees; a range of casing wall angles was tested for each one of these hub wall angles. A total of 87 simulations were performed, and their results are contained in Fig. 6.7. For these annular diffusers, the area ratio is defined as the annular area at the diffuser outlet divided by the area of the fan annulus, i.e. $AR = \Delta A_{\mathrm{difo}}/\Delta A_{\mathrm{F}}$.

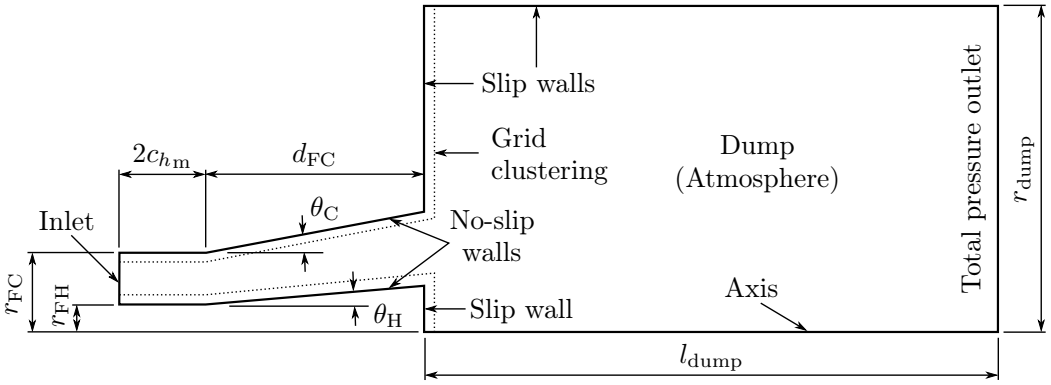

Figure 6.6: Computational domain used for annular diffuser simulations

Comparing Figs. 6.7a and 6.7c, it is clear that the area ratio for maximum pressure recovery is dependent on the combination of wall angles used, which contradicts the findings of Sovran and Klomp (1967: 287). However, they performed their experiments with axial inlet flow. The presence of inlet swirl thus makes the selection of wall-angle combination more critical. The highest pressure recovery, i.e. $K_{\mathrm{rec}} = 1.143$, is reported for a diffuser with both inner and outer wall angles equal to 24° from the axial, giving an area ratio of 2.381. The equiangular annular diffusers with wall angles equal to 20°, 22° and 26° perform within five per cent of the maximum value.

The equiangular diffuser of area ratio 2.253 with wall angles of 22° from the axial is recommended: Its pressure recovery of $K_{\mathrm{rec}} = 1.134$ is within one per cent of the maximum value but with slightly shallower wall angles. It is interesting how this compares with the findings of Srinath (1968), cited by McDonald *et al.* (1971) (see Subsection 2.4.5). He observed peak pressure recovery with a constant inlet swirl angle equal to the total divergence angle of the annular walls. The total divergence angle of the recommended equiangular

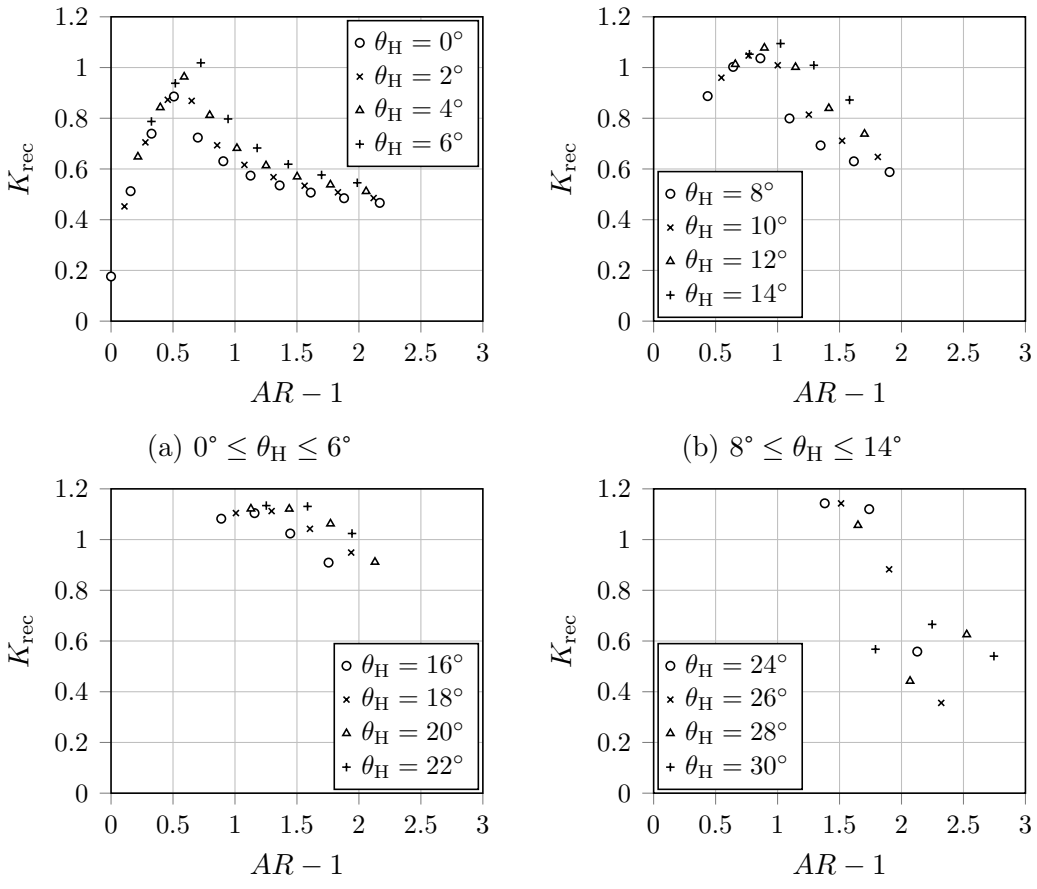

(a) $0° \leq \theta_{\text{H}} \leq 6°$

(b) $8° \leq \theta_{\text{H}} \leq 14°$

(c) $16° \leq \theta_{\text{H}} \leq 22°$

(d) $24° \leq \theta_{\text{H}} \leq 30°$

Figure 6.7: Variation of pressure recovery coefficient with area ratio for annular diffusers

diffuser is $2\theta = 44°$. The maximum swirl angle at the M-fan outlet is 44° at the hub. It thus seems that his finding may hold for the maximum swirl angle of free-vortex swirl distributions as well.

6.7 Annular Diffuser with a Stator at its Inlet

In this case, a stator was installed between the fan outlet and annular diffuser inlet. Similar to the conical diffuser case with a stator at its inlet, the leading edge of the stator was located half a mean rotor chord length downstream of the M-fan, and the trailing edge was located 1.5 mean stator chord lengths upstream of the diffuser. The same computational domain as in the previous section was used, but EADM discs were inserted at the domain inlet to represent the stator. Grid-independent solutions where obtained (see Appendix C) and results became independent with boundary distances of $l_{\text{dump}} = 14d_{\text{FC}}$ and $r_{\text{dump}} = 6r_{\text{FC}}$ (see Appendix D). These simulations were performed on wall-

integrated meshes with approximately 650 000 nodes.

A parametric study was performed to find the annular diffuser geometry that yields the highest performance: The hub wall angle was varied within the range of $0° \leq \theta_H \leq 20°$ combined with various casing wall angles. Altogether, 93 combinations were simulated. The results are illustrated in Fig. 6.8

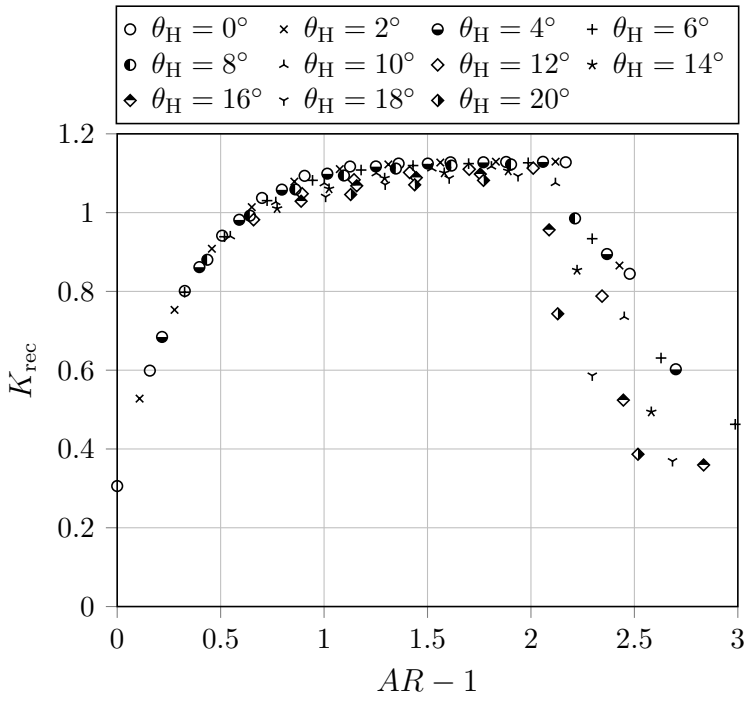

Figure 6.8: Variation of pressure recovery coefficient with area ratio for annular diffusers with a stator at their inlets

Although Fig. 6.8 may seem overwhelmingly dense, there is a clear trend in the data for area ratios up to approximately three. This trend substantiates the finding of Sovran and Klomp (1967: 287), namely that the area ratio for a specified pressure recovery is relatively independent of the combination of wall angles. From the figure, it seems that any of the tested annular diffusers with area ratios between two and three will perform well. The highest reported pressure recovery, i.e. $K_{rec} = 1.129$, is for a diffuser of area ratio 3.119 having a wall angle combination of $\theta_H = 2°$ and $\theta_C = 20°$. However, 15 more of the tested wall angle combinations produce pressure recoveries within one per cent of the maximum value. The diffuser with a cylindrical hub, i.e. $\theta_H = 0°$, and outer wall angle of 14° (or area ratio 2.360) falls within this group. This diffuser will probably be the most economical to manufacture since shallower wall angles result in smaller wall surface areas.

6.8 Annular Diffuser with a Stator at its Outlet

Only the recommended annular diffuser in Section 6.6 is considered here, i.e. the equiangular diffuser with half-wall angles equal to 22°. A stator was added at the diffuser outlet to recover the residual circumferential component of dynamic pressure. A new stator had to be designed as the velocity profiles at its inlet were now different than they were when located directly downstream of the M-fan. The design method in Appendix B was followed, but this time, 13 stator blades were used and only 45 % of the swirl could be removed. These changes were necessary in order to obtain realistic blade chord lengths (i.e., approximately 1 m to 1.5 m). The chord of the resulting stator blades varies in the range of 1.29 m at the hub to 1.52 m at the tip. The blade loading varies between 0.31 and 0.75. Figure 6.9 illustrates how the flow profiles change from the inlet to the outlet of the new stator.

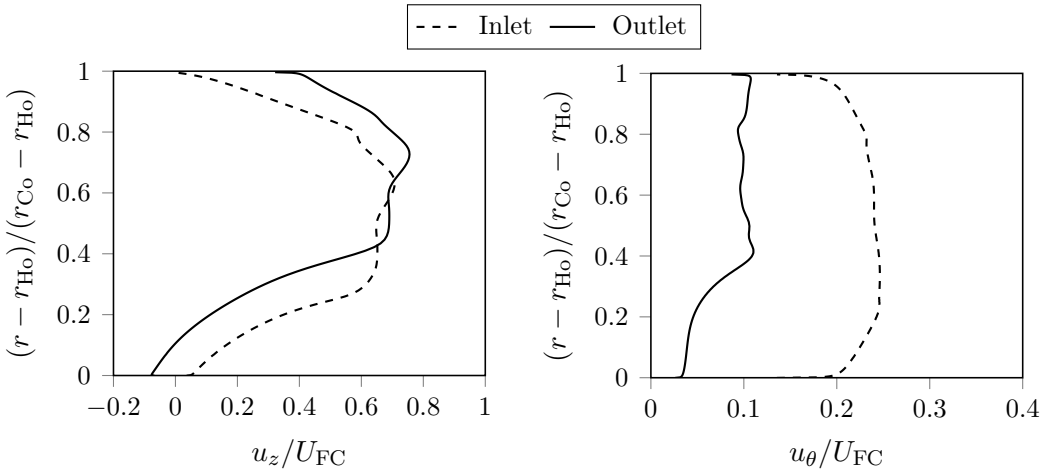

(a) Axial velocity

(b) Circumferential velocity

Figure 6.9: Velocity profiles at the inlet and outlet of the stator located at the annular diffuser exit

The discharge dump dimensions needed to be $l_{\mathrm{dump}} = 14d_{\mathrm{FC}}$ and $r_{\mathrm{dump}} = 6r_{\mathrm{FC}}$ for these computations to not be affected by the dump boundaries (see Appendix D). With these boundary distances, meshes with 681 320 cells were capable of resolving the mean and near-wall flow (see Appendix C). This outlet configuration yields a pressure recovery coefficient of $K_{\mathrm{rec}} = 0.951$ near the design flow rate. This is about 16 % lower than what it was for the annular diffuser on its own, i.e. $K_{\mathrm{rec}} = 1.134$ (see Section 6.6). Notwithstanding the added complexity and costs associated with the stator, the performance is actually worse. Therefore, this configuration is deemed unsuccessful.

6.9 Sensitivity to Off-Design Conditions

From the above results, it is evident that the recommended annular diffusers with and without stators outperformed the recommended conical diffusers with and without stators. The least amount of pressure recovery was achieved with a stator only. It is, however, not clear whether the annular diffuser with or without a stator at its inlet performs better at the design flow rate: Without a stator, the pressure recovery coefficient was $K_{\text{rec}} = 1.134$. With a stator, it was $K_{\text{rec}} = 1.125$.

A conclusive statement as to which outlet configuration provides the best performance can thus not yet be made. The determining factor will be to see which outlet configuration responds the best to off-design conditions. The recommended diffuser geometries in Sections 6.4 to 6.8 were used for this investigation: That is, the conical diffuser of area ratio 1.507, and the one of area ratio 1.792 with a stator at its inlet. The 22° equiangular annular diffuser, and the one with half-wall angles of $\theta_{\text{H}} = 0°$ and $\theta_{\text{C}} = 14°$ with a stator at its inlet. Finally, that same annular diffuser with 22° equiangular walls, but fitted with a newly designed stator at its outlet.

Wilkinson (2017: 70–72) provides outlet velocity profiles for the M-fan at off-design conditions ranging from 265 to 385 m^3/s. These fixed profiles were used to specify the inlet boundary conditions for the individual cases. The resulting pressure recovery coefficients are displayed in Fig. 6.10. The equiangular annular diffuser and the annular diffuser with a stator at its inlet produced the highest pressure recoveries over a range of flow rates. In the vicinity of the design flow rate, these two annular diffusers perform essentially the same. However, at low flow rates, the performance of the annular diffuser with a stator deteriorates. It seems that outlet configurations with stators generally follow this trend. A possible reason for this is that the stators were designed for the design point only. At off-design flow rates, the velocity profiles at the inlets of the stators are no longer the same, and optimum stator performance is not expected. The performance of fixed stator blades is thus not robust to off-design conditions. Moreover, adding a stator generally results in a longer and more expensive diffuser unit. The best overall performer is, therefore, the equiangular annular diffuser with wall angles of 22° from the axial: It provides the highest pressure recoveries at design and off-design flow rates.

6.10 Fan-Diffuser Characteristics

Chapter 3 demonstrated that the effect of pressure recovery is to shift the operating point to a higher volume flow rate than the initial design point. The pressure recovery results for the 22° equiangular annular diffuser that was recommended in the previous section were used to illustrate how this

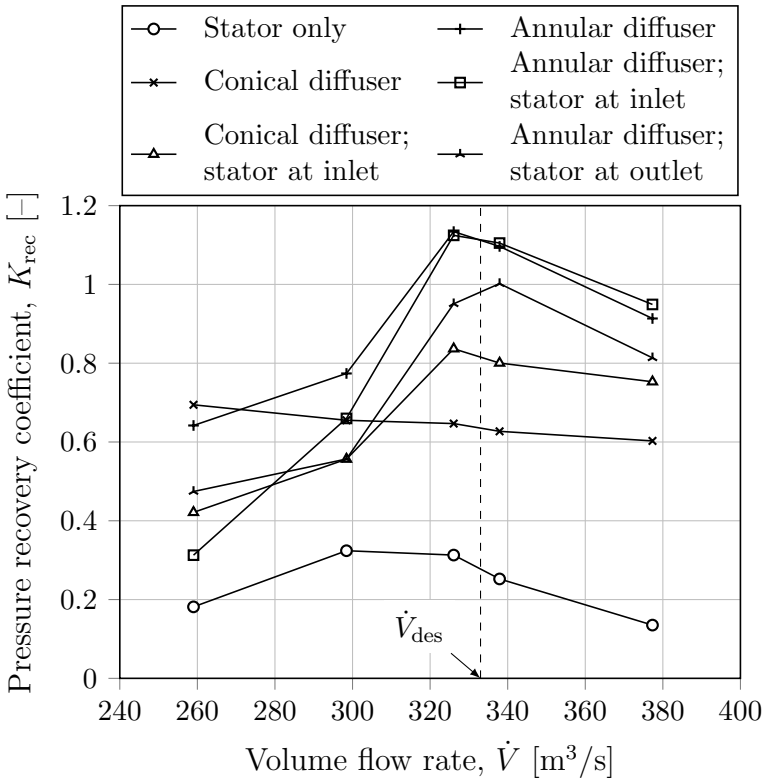

Figure 6.10: Variation of pressure recovery coefficient with volume flow rate for the different outlet configurations (lines added for clarity; not for trends)

diffuser affects the characteristics of the M-fan. Figures 6.11 and 6.12 depict the fan-diffuser static pressure and static efficiency characteristics, respectively. Similar to the approach in Chapter 3, a system curve of the form $\Delta p_{\text{sys}} = a\dot{V}^2$ that passes through the origin and design point was included in Fig. 6.11.

Pressure recovery raised the static pressure from 114.7 Pa at the design point to 130.0 Pa at the new operating point—a relative increase of 13.3 %. The volume flow rate though the fan increased from 333.0 to 354.2 m^3/s (a 6.3 % relative increase). The static efficiency increased from 59.4 to 79.4 %—an absolute increase of 20.0 %.

6.11 Conclusions

In this chapter, various outlet configurations were tested for the M-fan to see which one provides the highest pressure recovery at the design flow rate. These configurations were then evaluated at off-design flow rates to see how robust they are to off-design operating conditions. After that, the results of the overall best performing discharge configuration were superimposed on the characteristics of the M-fan to investigate how pressure recovery affects the characteristics of

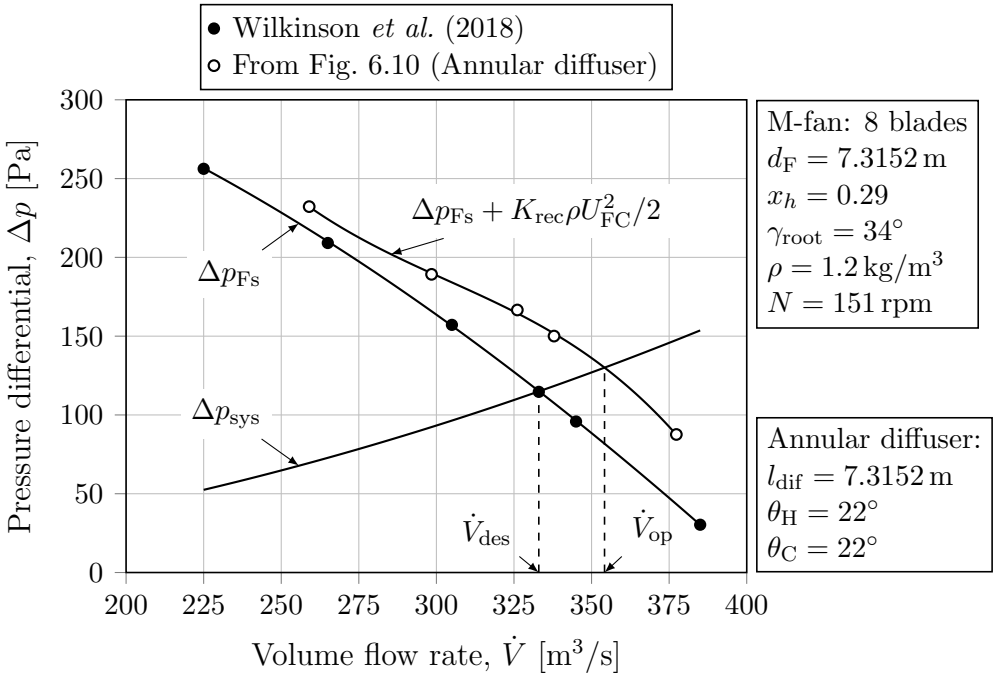

Figure 6.11: Effect of pressure recovery on M-fan static pressure characteristics

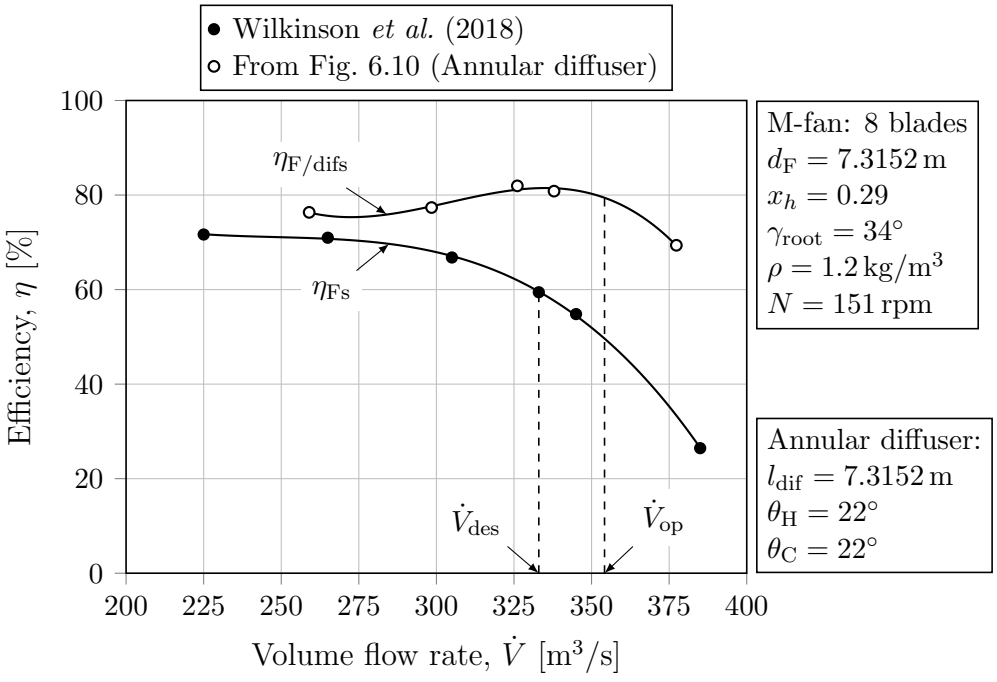

Figure 6.12: Effect of pressure recovery on M-fan static efficiency characteristics

the fan. Section 6.2 contains details pertaining to the computational setup: It includes information on the geometry and meshing strategies, the modelling of turbulence and the discharge to the open atmosphere, boundary conditions, fluid properties, solvers, discretisation practises, and sensitivity studies.

The pressure recovery at the design flow rate analyses for the different outlet configurations are contained in Sections 6.3 to 6.8. The configuration with the stator only is discussed in Section 6.3: It produced the least amount of pressure recovery amongst all the tested discharge configurations. Conical diffusers are scrutinised in Section 6.4: The best diffuser performed approximately twice as good as the previous stator case. Only a narrow range of area ratios produced high pressure recoveries. In Section 6.5 a stator was added between the fan discharge and conical diffuser inlet: Geometries yielding high pressure recoveries were considerably less sensitive to the area ratio. Pressure recoveries were also higher than in the previous case.

Annular diffusers are investigated in Section 6.6: The wall-angle combination for a specified area ratio affected diffuser performance. High pressure recoveries were reported for relatively wide-angled equiangular diffusers. One of these with a total divergence angle equal to the maximum swirl angle at the fan outlet nearly produced the highest pressure recovery. Section 6.7 considers a case where a stator was added in-between the fan and annular diffuser: Pressure recoveries were high and insensitive to the combination of wall angles used for a specified area ratio. The final discharge configuration is discussed in Section 6.8: A stator was added at the outlet of the recommended equiangular annular diffuser of Section 6.6. However, this setup was not a success. The performance with the stator was worse compared to when it was not installed.

The best diffuser geometries that came from Sections 6.3 to 6.8 were now tested at off-design flow rates. Section 6.9 contains the results: Configurations that employed stators generally performed poorly at off-design flow rates, especially lower flow rates. That is because the stators were designed for operating conditions only. The annular diffuser with both wall angles equal to 22° from the axial produced high pressure recoveries at design and off-design flow rates. Therefore, this is the recommended discharge configuration for the M-fan.

The final section, Section 6.10, demonstrates how this recommended annular diffuser affects the performance characteristics of the M-fan: The effect of pressure recovery was to increase the static pressure from 114.7 Pa at the design point to 130.0 Pa at the new operating point (13.3 % relative increase). The flow rate through the fan increased from 333.0 to 354.2 m^3/s (6.3 % relative increase). Finally, the static efficiency of 59.4 % at the design point increased to 79.4 % at the new operating point—an absolute increase of 20.0 %.

Chapter 7

Conclusions and Recommendations

7.1 Main Findings

This research aimed to reduce the outlet dynamic pressure loss of an induced draught air-cooled condenser (ACC) through pressure recovery. The latter refers to the conversion of dynamic pressure to static pressure. Diffusers, stators, or a combination of these can be used to recover pressure. The effect of pressure recovery is to increase the mechanical energy available to the airstream in the ACC. Pressure recovery thus shifts the operating point of the fan to a higher volume flow rate than the initial design point and increases the static efficiency of the fan. Higher heat removal rates are thus possible due to the increased flow rate through the fan unit.

The M-fan of Wilkinson *et al.* (2017) was selected for this study. Various discharge configurations were tested for this fan using computational fluid dynamics (CFD). These discharges included a stator, conical and annular diffusers with and without stators at their inlets, and an annular diffuser with a stator at its outlet. The discharge configuration that produced the highest pressure recovery was an annular diffuser. Its inner hub and outer casing walls were both directed 22° away from the axial. Its length was equal to the diameter of the M-fan. This diffuser produced a pressure recovery coefficient of $K_{\text{rec}} = 1.134$ at the design flow rate. It also produced high pressure recoveries at off-design flow rates, making it robust to off-design ACC operating conditions. Assuming a system curve of the form $\Delta p_{\text{sys}} = a\dot{V}^2$, the achieved pressure recovery increased the volume flow rate through the M-fan by 6.34 %. The static efficiency at the new operating point was 20 % (absolute) higher than at the initial design point.

7.2 Thesis Overview

The topic was introduced in Chapter 1, which outlined the purpose of the study. Chapter 2 covered literature on the M-fan, diffusers, stators, and numerical studies on flows involving adverse pressure gradients and turbomachinery blading. Chapter 3 provided the draught equation for an induced draught ACC and illustrated the effect of pressure recovery on the system. A pressure recovery coefficient, K_{rec}, was defined. It is a function of the kinetic energy correction factors at the fan and diffuser discharge planes as well as the area ratio and loss coefficient of the diffuser.

Chapter 4 covered details on the modelling of turbulence and turbomachinery blading. The details of the CFD validation study on the ERCOFTAC conical diffuser were provided in Chapter 5. Solutions were found to be sensitive to the specified inlet turbulence quantities and turbulence model. Amongst 13 turbulence models, the wall-integrated k-ω model compared relatively well with measurements while the SST k-ω version deviated vastly. Furthermore, solutions were found to be insensitive to transient and three-dimensional effects.

Chapter 6 outlined the details and results of the parametric studies of the different M-fan outlet configurations. A stator alone performed the worst. Conical diffusers performed better, and when a stator was added at their inlets, the performance increased at design conditions. Annular diffusers performed even better, but in this case, the best ones with and without a stator at their inlets performed very similarly in the vicinity of the design flow rate. However, the pressure recovery dropped sharply at low off-design flow rates in most of the configurations that employed stators. An annular diffuser with a stator at its outlet was also tested, but it was not a success. Therefore, the earlier mentioned 22° annular diffuser with no stator was deemed the most successful outlet configuration for the M-fan.

7.3 Recommendations

The most pressing shortcoming of the current research is that the numerical results are not particularly well validated. In the validation study, the numerical results did not compare as closely with the experimental measurements as one would have liked. Experimental data of the M-fan with these different outlet configurations were not available for validation purposes. The generation of such data also did not fall within the scope of this project. An experimental study that follows on the current research is, therefore, recommended.

In the current research, parametric studies were performed using fixed velocity profiles at the design point. After that, the best configurations were tested at off-design flow rates. However, Chapter 3 demonstrated that pressure recovery

shifts the operating point to a higher volume flow rate than the initial design flow rate. At this new operating point, the velocity profiles at the fan outlet will be different than at the design point. Therefore, stators and diffusers that are designed for the new operating point might look slightly different from the ones in this study. It is thus recommended to perform parametric studies where the fan is simulated together with the stators and diffusers.

The performance of conical and annular diffusers generally increases as inlet swirl increases up to a point and then deteriorates. The swirl intensity at the M-fan outlet was found to be higher than what is beneficial for diffuser performance. In this study, the stator at the inlet of the diffusers was designed to remove all the swirl from the flow exiting the M-fan. Simulations were thus performed with either excessive or zero inlet swirl—no in-between swirl intensities. It is, therefore, recommended to perform parametric studies with stators that remove different levels of swirl. The overall highest performing configuration might be a specific diffuser geometry matched with a specific level of inlet swirl.

Owing to the higher discharge velocities associated with induced draught ACCs, they are less sensitive to crosswinds and less susceptible to hot-plume recirculation compared to forced draught ACCs. However, adding a diffuser will reduce the discharge velocity and potentially nullify this advantage associated with induced draught ACCs. As a consequence, pressure recovery might deteriorate under windy conditions. A study investigating the effect of crosswind on an induced draught ACC fitted with a diffuser is thus recommended.

Diffuser performance is also a function of its length. In this study, the length was fixed equal to the fan diameter. The best annular diffuser had wall angles of 22° from the axial. Adding such a diffuser downstream of the M-fan will result in a large and possibly impractical structure. Therefore, it is recommended to perform parametric studies where the diffuser lengths are varied. A considerably shorter diffuser might still yield satisfactory performance.

Appendix A

M-Fan Specifications

Wilkinson *et al.* (2017) designed the M-fan for a forced draught ACC in a CSP plant. The fan is depicted in Fig. A.1 and its design specifications are listed in Table A.1. The chord and aerofoil thickness distributions of the fan are linear due to manufacturing constraints. The blading was designed similar to the isolated aerofoil methodologies of Bruneau (1994) and Van der Spuy (1997), with an added XFOIL optimisation step. This step optimises the aerofoil camber distribution by optimising the lift-drag ratio along the blade span. As a result, it improves the efficiency and stall margin near the hub. Wilkinson *et al.* (2017) used the NASA-LS 0413 aerofoil profile for the fan blades with the lift-drag data of McGhee and Beasley (1979). The angle of attack at any point on the blade is kept below five degrees to reduce blade twist and allow for a wider range of stall-free operation (stall commences when $\alpha_{\text{att}} = 15^{\circ}$ for the NASA-LS 0413 blade profile).

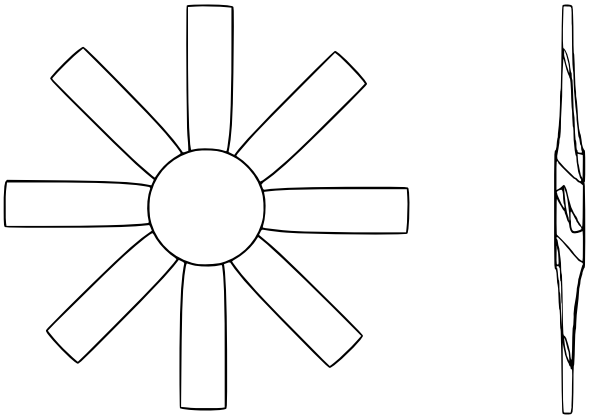

Figure A.1: Schematic of the M-fan (Wilkinson *et al.*, 2018)

Figures A.2 to A.4 portray the fan characteristic curves. These performance characteristics were obtained numerically using a three-dimensional periodic fan model with zero tip clearance. This model produced a fan static pressure

Table A.1: M-fan design specifications (Wilkinson *et al.*, 2017)

Description	**Symbol**	**Value**
Diameter	d_F	24 ft (7.3152 m)
Number of blades	n_b	8
Hub-to-tip ratio	x_h	0.29
Rotational speed	N	151 rpm
Blade root setting angle	γ_root	34°
Design flow rate	$\dot{V}$	333 m^3/s
Estimated fan static pressure	p_Fs	116.7 Pa
Estimated fan power consumption	P_F	63.29 kW
Estimated fan static efficiency	η_Fs	61.4 %

rise of 114.7 Pa at the design flow rate while consuming 64.24 kW of power. The fan static efficiency is thus 59.4 % at the design point.

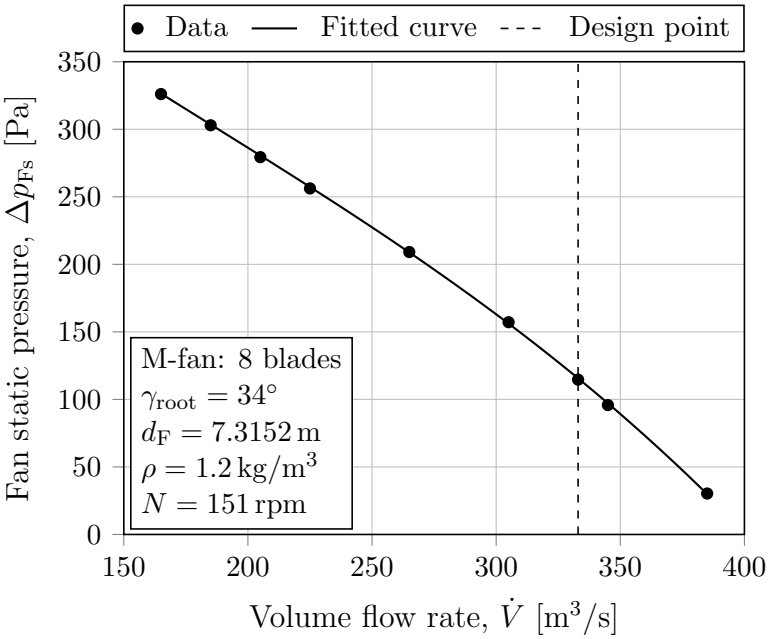

Figure A.2: M-fan static pressure characteristics (Wilkinson *et al.*, 2018)

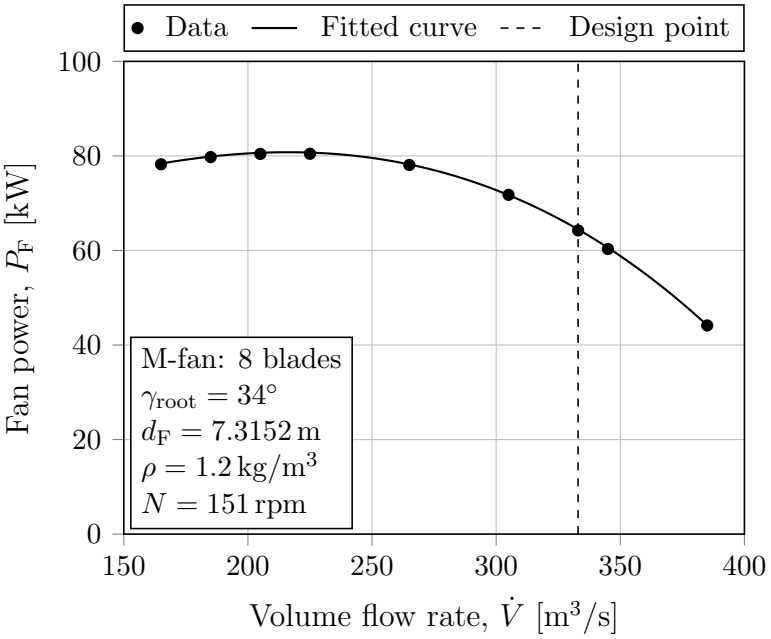

Figure A.3: M-fan power consumption characteristics (Wilkinson *et al.*, 2018)

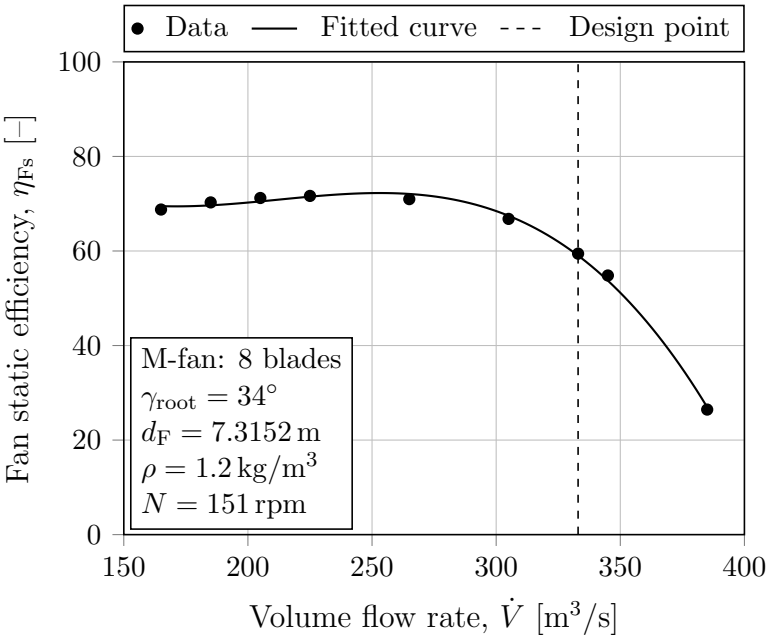

Figure A.4: M-fan static efficiency characteristics (Wilkinson *et al.*, 2018)

Appendix B

Stator Design

B.1 Introduction

This appendix documents the design methodology that was followed to design the stators that were used in this research project. The method employs isolated aerofoil theory, i.e. it treats each blade as a series of two-dimensional aerofoil sections (Bruneau, 1994: 13). With knowledge of inlet velocity profiles, lift and drag data of isolated aerofoil sections can be used for blading design at specified radial stations. The methodology is based on the work of Louw *et al.* (2012), which is a design method for large rotor-only axial flow fans.

Rotor design requires a design objective, i.e. required pressure rise and volume flow rate. The fan configuration must then be established, i.e. the number of blades and hub-to-tip ratio. The blading that will satisfy the design objectives then needs to be designed. This design is usually done under a criterion such as maximum efficiency. Louw *et al.* (2012) achieved this with three Fortran programs: FANVTX, FANOPT and FANBLD. The first program calculates the swirl and axial velocity distributions for a specified mass flow rate and static pressure rise. The second program determines the optimum hub-to-tip ratio. Then, the blading geometry that will provide the profiles calculated by FANVTX is determined by the third program.

The design process for a stator is somewhat more straightforward. The aim is to eliminate, or reduce, the swirl of the flow entering the stator. The velocity profiles at the stator inlet will be available. At the outlet, the stator forces the swirl to zero, or to a percentage of the inlet swirl. The vortex distribution is therefore known, and a program such as FANVTX is unnecessary. The hub-to-tip ratio will coincide with that of the fan or annular diffuser. Hence, only the blading needs to be designed. The equations used by Louw *et al.* (2012) for FANBLD were used to write a Python program, named OGVBLD, for the design of stator blades. Note that rotor design is for a moving frame

of reference and, therefore, involves relative velocities and flow angles. Stator design, on the other hand, is for a stationary frame of reference. It thus involves absolute velocities and flow angles.

The sections below provide the equations to calculate the static pressure rise over the stator and its blading geometry. A sample calculation for a stator to be used downstream of the M-fan is also provided at a radial station of approximately two-thirds of the stator blade span.

B.2 Static Pressure Rise

In the equations to follow, positions 3 and 4 refer to the immediate upstream and downstream locations from the stator, respectively. Positions 1 and 2 denote the immediate upstream and downstream locations from the rotor, respectively. The stator does no work on the fluid. Under the assumption of isotropic flow, the total pressure thus remains constant across the stator. In other words,

$$p_{\mathrm{t}3} - p_{\mathrm{t}4} = 0, \tag{B.1}$$

$$(p_{\mathrm{s}3} + p_{\mathrm{d}3}) - (p_{\mathrm{s}4} + p_{\mathrm{d}4}) = 0. \tag{B.2}$$

Assuming that the axial velocity remains constant through the stator and that radial velocity is negligible, the static pressure difference across the stator is given by,

$$\Delta p_{\mathrm{OGVs}} = p_{\mathrm{s}4} - p_{\mathrm{s}3} = p_{\mathrm{d}3} - p_{\mathrm{d}4} \tag{B.3}$$

$$= \tfrac{1}{2}\rho\big(u_z^2 + u_{\theta 3}^2\big) - \tfrac{1}{2}\rho\big(u_z^2 + u_{\theta 4}^2\big) \tag{B.4}$$

$$= \tfrac{1}{2}\rho\big(u_{\theta 3}^2 - u_{\theta 4}^2\big). \tag{B.5}$$

The mass-averaged pressure differential is obtained by integrating the distribution over the annulus, viz.,

$$\Delta\bar{p}_{\mathrm{OGVs}} = \frac{2\pi\rho}{\dot{m}} \int_{r_{\mathrm{H}}}^{r_{\mathrm{C}}} u_z \Delta p_{\mathrm{OGVs}} r \,\mathrm{d}r \,. \tag{B.6}$$

B.3 Blading Design

OGVBLD is a program that was written to determine the blading geometry for outlet guide vanes. The program requires velocity profiles at the stator inlet. Further, the user needs to specify the number of stator blades, the lift coefficients at the hub and tip, as well as the percentage swirl to be removed.

In the equations presented below, all angles are measured from the axial plane. The swirl coefficients at each radial station are computed with

$$\epsilon_3 = u_{\theta 3}/u_z \quad \text{and} \quad \epsilon_4 = u_{\theta 4}/u_z, \tag{B.7}$$

with an upper limit of 1.1 to avoid blade stall (Wallis, 1983: 183). The flow angles are then computed with

$$\alpha_3 = \arctan \epsilon_3 \quad \text{and} \quad \alpha_4 = \arctan \epsilon_4. \tag{B.8}$$

The mean flow angles and velocities are calculated with

$$\alpha_\mathrm{m} = \arctan\left[(\epsilon_3 + \epsilon_4)/2\right], \tag{B.9}$$

$$u_\mathrm{m} = u_z \sec \alpha_\mathrm{m}. \tag{B.10}$$

According to Wallis (1983: 149), the blade loading factors can be approximated with

$$C_L\sigma \approx 2(\epsilon_3 - \epsilon_4)\cos \alpha_\mathrm{m}. \tag{B.11}$$

The blade chord at the hub and tip can now be calculated using the lift coefficients that were specified by the user at the hub and tip, i.e.,

$$c_h = \frac{2\pi r(C_L\sigma)}{n_b C_L}. \tag{B.12}$$

The chord distribution along the blade span is obtained by interpolating between the hub and tip. Any interpolation scheme can be used, but following the example of Louw *et al.* (2012), linear interpolation was used. Subsequently, the blade solidity, lift coefficient, and Reynolds number distributions are determined with

$$\sigma = \frac{n_b c_h}{2\pi r}, \tag{B.13}$$

$$C_L = C_L\sigma/\sigma, \tag{B.14}$$

$$Re_{c_h} = u_\mathrm{m} c_h/\nu. \tag{B.15}$$

With the lift coefficient distribution known, the angle of attack at each radial station is obtained from the selected aerofoil's characteristics, i.e. the lift coefficient versus angle of attack for specified Reynolds numbers. The final step is to calculate the stagger angle distribution that describes the blade twist. Louw *et al.* (2012) and Wilkinson *et al.* (2017) calculate it using

$$\xi = \alpha_3 - \alpha_\mathrm{att}, \tag{B.16}$$

where α_3 is the incoming flow angle. However, this equation yields incorrect results when implemented with the extended actuator disc model (EADM) that was written by Engelbrecht (2018). His model employs mean flow angles to compute the angles of attack. Therefore, for the stator design method and EADM code to correlate, the following definition for the stagger angle was adopted:

$$\xi = \alpha_\mathrm{m} - \alpha_\mathrm{att}. \tag{B.17}$$

B.4 Sample Calculation

In this section, the equations in the previous sections are applied to illustrate the working of OGVBLD. A sample calculation for the stator that was used downstream of the M-fan in Sections 6.3, 6.5 and 6.7 is provided. The inlet velocity profiles to the stator are the outlet velocity profiles of the M-fan at the design flow rate of $\dot{V} = 333\,\mathrm{m}^3/\mathrm{s}$, shown in Fig. B.1. The blade profile that was selected for the stator is the same as that of the M-fan, namely the NASA-LS 0413 profile. It has good lift-drag characteristics and is well documented. Figure B.2 contains lift coefficient versus angle of attack characteristics for this profile. The red square data points in Figs. B.1 and B.2 are at approximately two-thirds of the blade span and were used in the sample calculation.

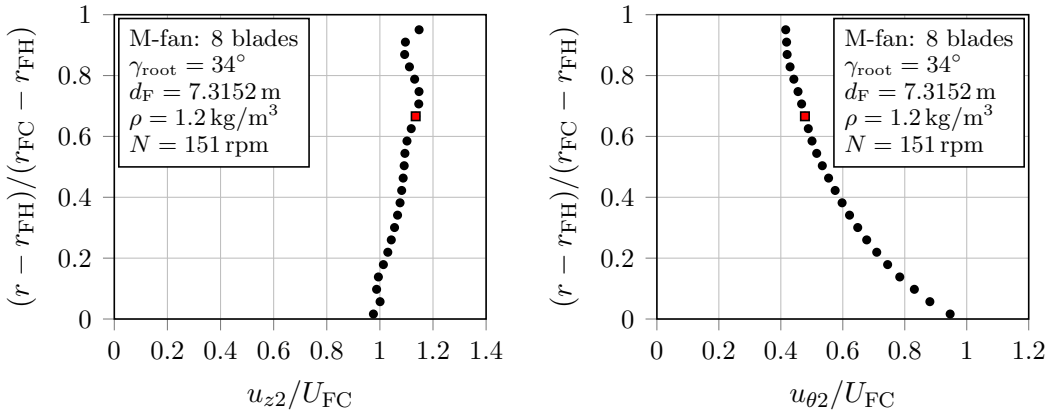

(a) Axial velocity (b) Circumferential velocity

Figure B.1: M-fan outlet velocity profiles at $\dot{V} = 333\,\mathrm{m}^3/\mathrm{s}$ (Wilkinson *et al.*, 2017)

The static pressure increase over the stator is calculated by applying Eq. (B.5) to all the data points in Fig. B.1 and then integrating over the annulus as in Eq. (B.6). This stator was designed to remove all the swirl from the incoming flow so that $u_{\theta 4} = 0$. The resulting pressure rise is $\Delta\bar{p}_{\mathrm{OGVs}} = 10.1\,\mathrm{Pa}$. This correlates exceptionally well with the pressure increase that was reported in Subsection 3.5.2 for the case of swirl removal only, where $\alpha_{e\mathrm{difo}} \approx \alpha_{e\mathrm{FC}z}$ was assumed. The result was $\Delta\bar{p}_{\mathrm{OGVs}} = 10.0\,\mathrm{Pa}$.

The first steps of the blading design are to select the number of stator blades, the lift coefficients at the hub and tip, and the amount of swirl to remove. In order to keep the chord within reasonable length (see Eq. (B.12)), either the number of blades and lift coefficients should be selected sufficiently large or the amount of flow deflection, and hence blade loading (see Eq. (B.11)), should be sufficiently small. However, the lift coefficient should not be selected too close to the stall point of the blade profile to ensure stable operation in the case of

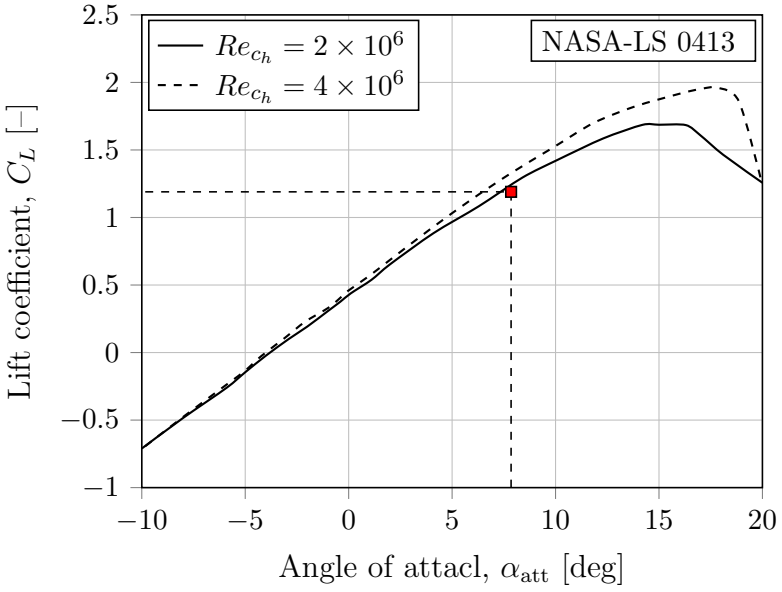

Figure B.2: Lift characteristics of the NASA-LS 0413 profile (McGhee and Beasley, 1979)

slight off-design conditions. Figure B.2 illustrates that the largest lift coefficient that was measured by McGhee and Beasley (1979) for a Reynolds number of 2×10^6 was 1.69 at an angle of attack of 15°. Beyond this point, the blade stalls, marked by a sharp reduction in lift coefficient. For the current design, the hub and tip lift coefficients were selected as $0.7C_{L\max} \approx 1.2$. It was found that nine stator blades could remove all the swirl without having excessive blade loading or chord lengths. The blade design equations in Section B.3 are now applied to the data points marked in red in Fig. B.1:

Swirl coefficient:

$$\begin{aligned} \epsilon_3 &= u_{\theta 3}/u_z \\ &= 3.707/8.805 \\ &= 0.421 \end{aligned} \tag{B.18}$$

Mean flow angle:

$$\begin{aligned} \alpha_{\text{m}} &= \arctan\left[(\epsilon_3 + \epsilon_4)/2\right] \\ &= \arctan[(0.421 + 0)/2] \\ &= 11.888^\circ \end{aligned} \tag{B.19}$$

Mean velocity:

$$\begin{aligned} u_{\text{m}} &= u_z \sec \alpha_{\text{m}} \\ &= 8.805 \sec(11.888^\circ) \\ &= 8.998\,\text{m/s} \end{aligned} \tag{B.20}$$

Blade loading factor:

$$\begin{aligned} C_L\sigma &\approx 2(\epsilon_3 - \epsilon_4)\cos\alpha_\mathrm{m} \\ &\approx 2(0.421 - 0)\cos(11.888^\circ) \\ &\approx 0.824 \end{aligned} \tag{B.21}$$

The chords at the hub and tip need to be calculated so that the rest of the chords can be obtained through linear interpolation. The values for the hub and tip where obtained in a similar fashion than above.

Fan hub:

$$\begin{aligned} c_h(r_\mathrm{FH}) &= \frac{2\pi r_\mathrm{FH}(C_L\sigma)_\mathrm{FH}}{n_b C_{L\mathrm{FH}}} \\ &= \frac{2\pi \cdot 1.103 \cdot 1.745}{9 \cdot 1.2} \\ &= 1.126\,\mathrm{m} \end{aligned}$$

Fan casing:

$$\begin{aligned} c_h(r_\mathrm{FC}) &= \frac{2\pi r_\mathrm{FC}(C_L\sigma)_\mathrm{FC}}{n_b C_{L\mathrm{FC}}} \\ &= \frac{2\pi \cdot 3.528 \cdot 0.713}{9 \cdot 1.2} \\ &= 1.447\,\mathrm{m} \end{aligned}$$

The chord for the data point of interest is thus:

$$\begin{aligned} c_h &= c_h(r_\mathrm{FH}) + \frac{c_h(r_\mathrm{FC}) - c_h(r_\mathrm{FH})}{r_\mathrm{FC} - r_\mathrm{FH}}(r - r_\mathrm{FH}) \\ &= 1.126 + \frac{1.447 - 1.126}{3.529 - 1.103}(2.791 - 1.103) \\ &= 1.349\,\mathrm{m} \end{aligned} \tag{B.22}$$

Solidity ratio:

$$\begin{aligned} \sigma &= \frac{n_b c_h}{2\pi r} \\ &= \frac{9 \cdot 1.349}{2\pi \cdot 2.791} \\ &= 0.692 \end{aligned} \tag{B.23}$$

Lift coefficient:

$$\begin{aligned} C_L &= C_L\sigma/\sigma \\ &= 0.824/0.692 \\ &= 1.190 \end{aligned} \tag{B.24}$$

Reynolds number:

$$\begin{aligned} Re_{c_h} &= u_\mathrm{m} c_h/\nu \\ &= 8.998 \cdot 1.349/\left(1.5 \times 10^{-5}\right) \\ &= 8.092 \times 10^5 \end{aligned} \tag{B.25}$$

The calculated Reynolds number is lower than the smallest Reynolds number at which McGhee and Beasley (1979) performed experiments to obtain lift-drag data for the NASA-LS 0413 profile. Subsequently, the data sets for the two lowest Reynolds numbers, namely $Re_{c_h} = 2 \times 10^6$ and 4×10^6, are used to extrapolate to lower Reynolds numbers.

The angle of attack is required to determine the stagger angle. It can be read off from the aerofoil's lift characteristics, shown in Fig. B.2. The angles of attack that correspond to $C_L = 1.190$ are $\alpha_{\text{att}} = 7.331^\circ$ and 6.471° for $Re_{c_h} = 2 \times 10^6$ and 4×10^6, respectively. Using linear extrapolation, the angle of attack corresponding to $Re_{c_h} = 8.092 \times 10^5$ is $\alpha_{\text{att}} = 7.851^\circ$. The stagger angle is thus:

$$\begin{aligned} \xi &= \alpha_{\text{m}} - \alpha_{\text{att}} \\ &= 11.888^\circ - 7.851^\circ \\ &= 4.037^\circ \end{aligned} \tag{B.26}$$

The above steps can be repeated for each and every data point to obtain the distributions of each variable.

B.5 Conclusions

This appendix contains a design methodology for stators. The equations for the determination of the static pressure rise over the stator and the design of the stator blades are provided. A program, OGVBLD, was written to aid the design process. The inputs to the program are velocity profiles at the stator inlet, the number of stator blades, the hub and tip lift coefficients, and the percentage swirl to be removed. The program also requires the isolated aerofoil lift characteristics for a specified blade profile. OGVBLD then computes, amongst other things, the spanwise distributions of the blade chord and stagger angle—the distributions that are required by the extended actuator disc model. OGVBLD also estimates the static pressure rise across the stator. A comprehensive sample calculation demonstrates the working of OGVBLD.

Appendix C

Grid Dependence Studies

C.1 Introduction

High-quality numerical studies usually include grid dependence studies. The solution of the underlying partial differential equations (PDEs) emerges through sequentially refining the mesh until grid-independent solutions are reached. That is, key flow properties do not change as the computational grid is refined beyond a certain point. This appendix contains the grid dependence studies for the different M-fan outlet configurations that were tested. For these simulations, the dump length and radius were fixed at $l_{\text{dump}} = 10d_{\text{FC}}$ and $r_{\text{dump}} = 5r_{\text{FC}}$, respectively.

C.2 Downstream Stator

Grid dependence for the configuration with only a stator at the fan exit was tested using the standard k-ω turbulence model with wall functions. The highest residual in these simulations reached 10^{-6}. Table C.1 provides the details of the different meshes. Figure C.1 illustrates how mesh refinement affects the discharge velocity profiles.

Table C.1: Grid dependence study for a downstream stator

Grid identifier	**Number of nodes**	**Average y^+** [–]	**K_{rec}** [–]	**Difference** [%]
Grid 1	342 462	265	0.352	2.239
Grid 2	685 378	189	0.345	0.052
Grid 3	1 369 684	134	0.344	–

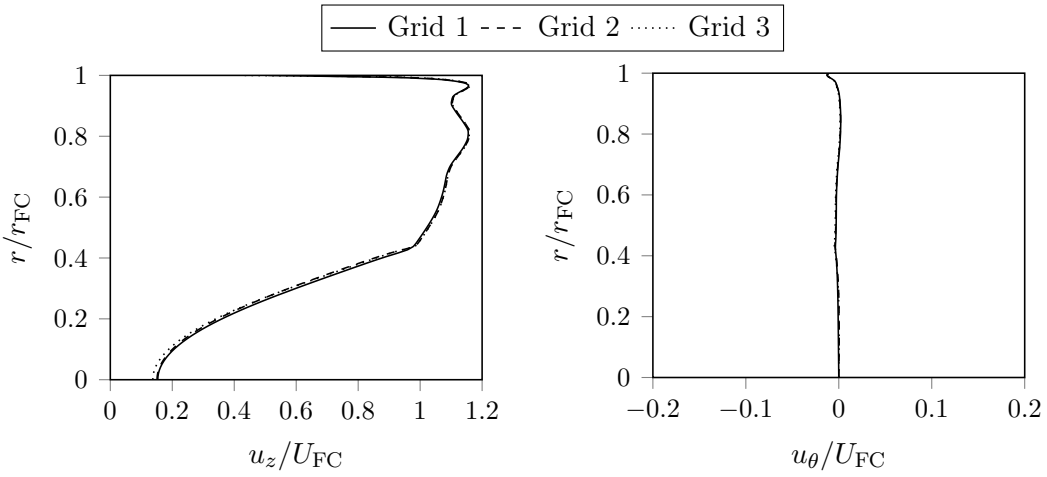

(a) Axial velocity (b) Circumferential velocity

Figure C.1: Flow profiles at the discharge plane with a stator only for successively refined meshes

The difference in pressure recovery coefficients obtained with the finest (Grid 3) and coarsest (Grid 1) meshes is smaller than five per cent (see Table C.1). From Fig. C.1 it is clear that flow profiles are captured just as well with Grid 1 compared to finer meshes. Therefore, Grid 1 is deemed satisfactory for resolving the mean flow.

C.3 Conical Diffuser

A conical diffuser with an included angle of $2\theta = 16°$, and thus area ratio of 1.792, was selected for the grid dependence study. It was arbitrarily selected within the range provided by Kröger (1998: 6.4.9), i.e. $12° \leq 2\theta \leq 17°$. The standard k-ω turbulence model with wall functions was employed. Residuals converged to 10^{-5} in each case. Table C.2 provides the details of the meshes and Fig. C.2 illustrates how mesh refinement affects the velocity profiles at the diffuser inlet and outlet. Results are very insensitive to the level of grid refinement. Grid 1 suffices to resolve the mean flow and was, therefore, selected.

Table C.2: Grid dependence study for a conical diffuser

Grid identifier	**Number of nodes**	**Average y^+** [–]	**K_{rec}** [–]	**Difference** [%]
Grid 1	364 288	311	0.537	0.479
Grid 2	729 070	219	0.538	0.644
Grid 3	1 456 932	154	0.537	0.509
Grid 4	2 913 843	108	0.534	–

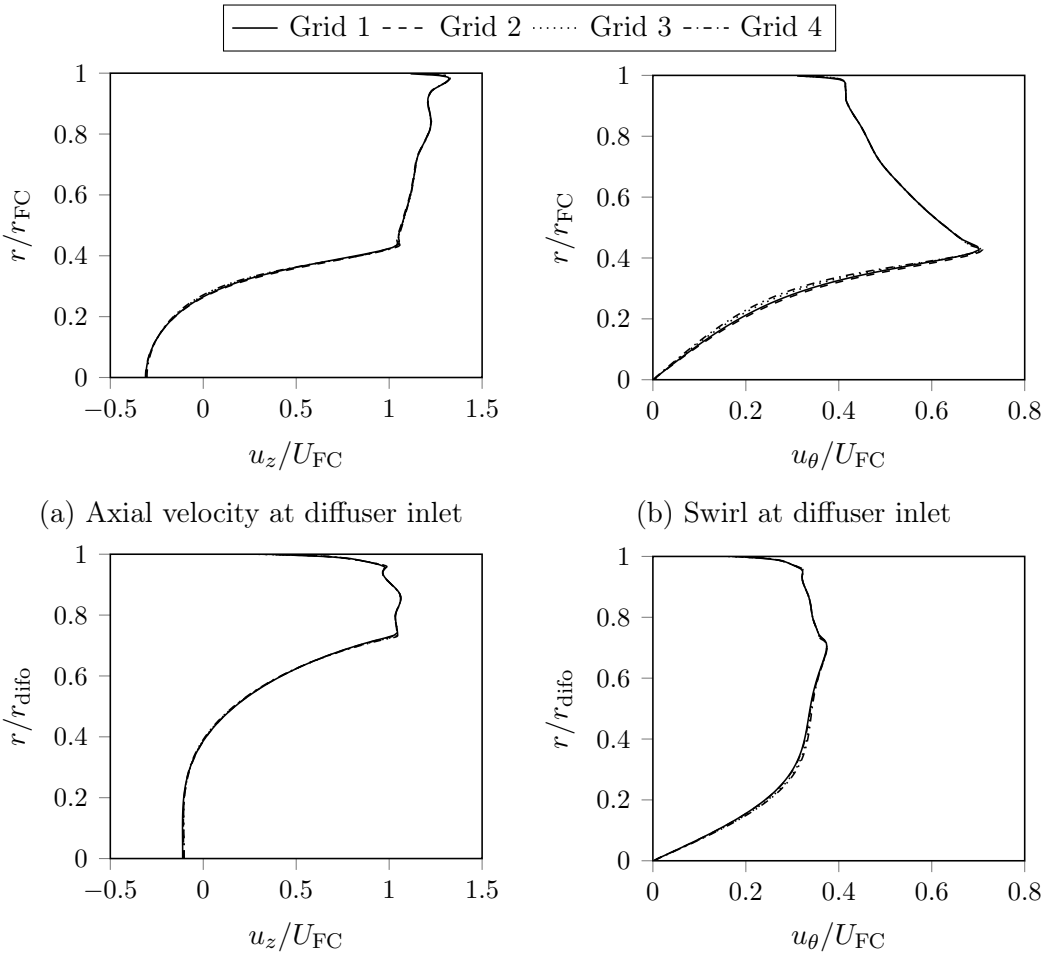

(a) Axial velocity at diffuser inlet

(b) Swirl at diffuser inlet

(c) Axial velocity at diffuser outlet

(d) Swirl at diffuser outlet

Figure C.2: Flow profiles at the inlet (top) and outlet (bottom) of a conical diffuser for successively refined meshes

C.4 Conical Diffuser with a Stator at its Inlet

In this case, a stator was added between the fan outlet and conical diffuser inlet. The conical diffuser with no stator that provided the highest pressure recovery in Section 6.4 was used for the grid dependence study, i.e. the $2\theta = 10°$ diffuser with an area ratio of 1.507. Wall functions were used along with the standard k-ω turbulence model. Residuals reached the order of 10^{-6} in these simulations. Table C.3 contains the details of the different meshes. Figure C.3 depicts the axial velocity profiles at the inlet and outlet of the diffuser for the successively refined meshes. The circumferential velocity profiles are not shown since the stator entirely removed the swirl. Therefore, it looks similar to Fig. C.1b. The results indicate that Grid 1 is capable of resolving the mean flow.

Table C.3: Grid dependence study for a conical diffuser with a stator at its inlet

Grid identifier	Number of nodes	Average y^+ [–]	K_{rec} [–]	Difference [%]
Grid 1	367 212	248	0.798	1.837
Grid 2	735 142	174	0.785	0.087
Grid 3	1 468 684	122	0.784	–

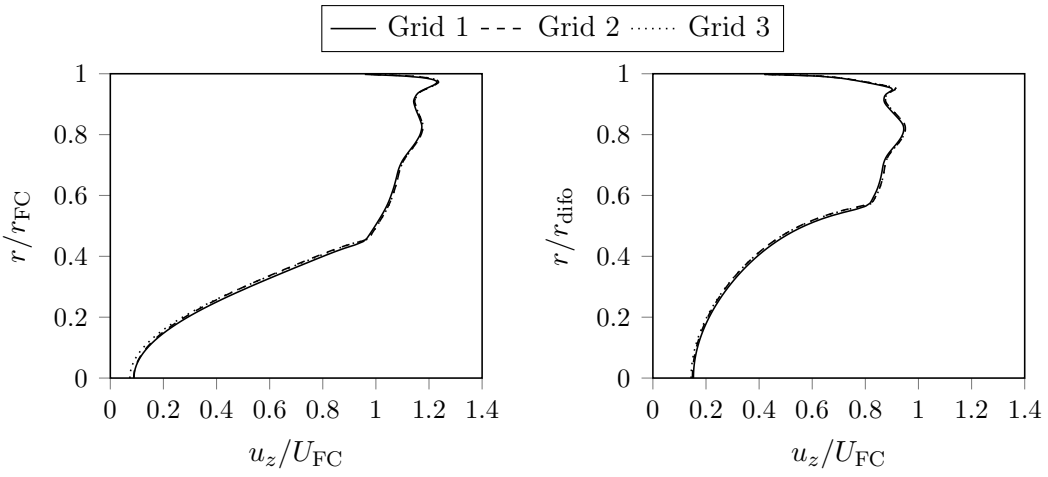

(a) Diffuser inlet (b) Diffuser outlet

Figure C.3: Axial velocity profiles of a conical diffuser with a stator at its inlet for successively refined meshes

C.5 Annular Diffuser

The formulas provided by Shepherd (1974) were used to obtain an annular diffuser that is analogous to the conical diffuser that was used for the grid dependence study in Section C.3. The resulting annular diffuser has wall angles of $\theta_{\mathrm{H}} = 3.3°$ and $\theta_{\mathrm{C}} = 11.2°$ measured from the axial. The standard k-ω turbulence model was used with the appropriate wall functions. The residuals of the underlying equations reached a maximum of 10^{-5}. The details of the successively refined meshes are contained in Table C.4. Figure C.4 provides velocity profiles at the diffuser inlet and outlet. Results are seen to be relatively insensitive to grid refinement. Grid 1 was, therefore, regarded adequate.

Table C.4: Grid dependence study for an annular diffuser

Grid identifier	Number of nodes	Average y^+ [–]	K_{rec} [–]	Difference [%]
Grid 1	400 240	272	0.644	2.454
Grid 2	801 206	189	0.641	1.911
Grid 3	1 600 780	134	0.635	0.976
Grid 4	3 199 474	94	0.630	0.198
Grid 5	6 402 760	66	0.629	–

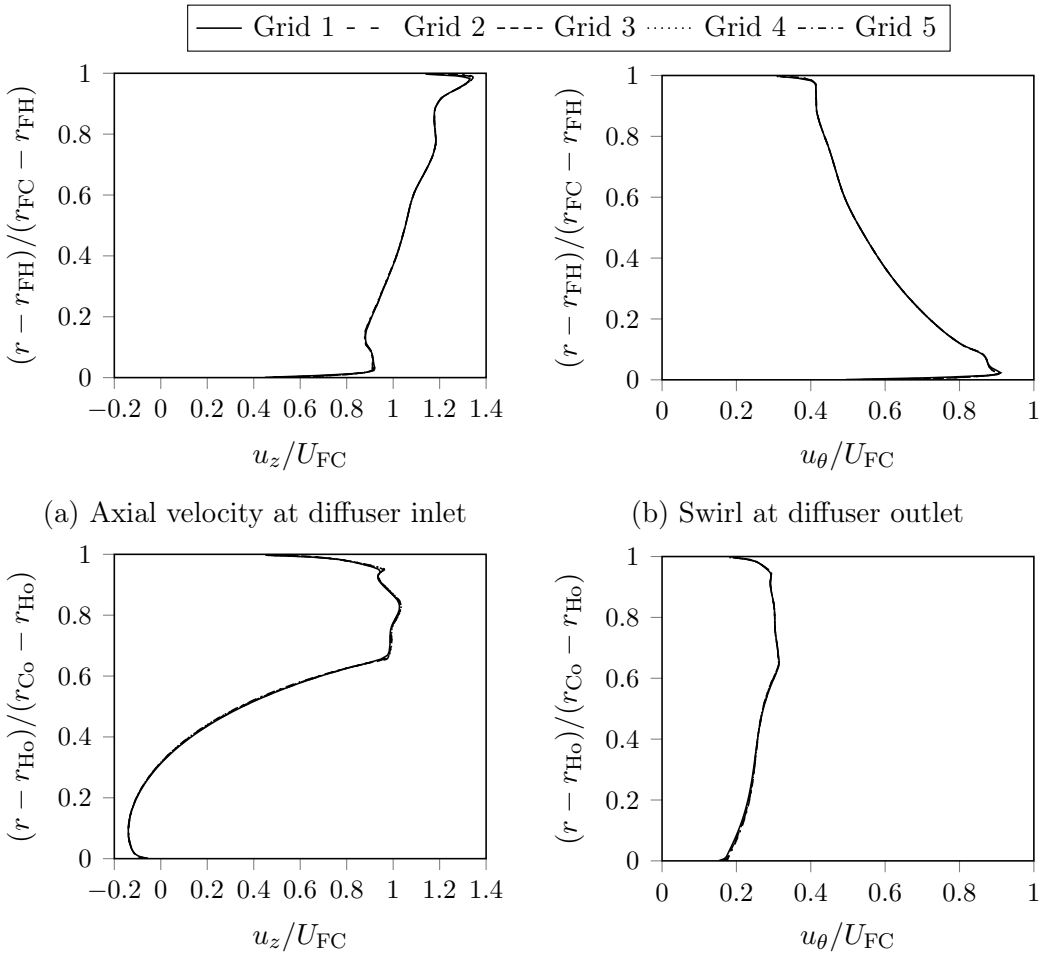

(a) Axial velocity at diffuser inlet

(b) Swirl at diffuser outlet

(c) Axial velocity at diffuser outlet

(d) Swirl at diffuser outlet

Figure C.4: Flow profiles at the inlet (top) and outlet (bottom) of an annular diffuser for successively refined meshes

C.6 Annular Diffuser with a Stator at its Inlet

The same annular diffuser as in Section C.5 was used for this grid dependence study. Except, this time a stator was added between the domain inlet and diffuser inlet. The standard k-ω model with wall functions was used, and residuals converged to the order of 10^{-6}. Table C.5 and Fig. C.5 illustrate that these simulation results are very insensitive to grid refinement. The mesh with 403 840 nodes yields results within one per cent of the finest mesh with 1 615 180 grid points. Therefore, Grid 1 was used for further computations.

Table C.5: Grid dependence study for an annular diffuser with a stator at its inlet

Grid identifier	**Number of nodes**	**Average** $\boldsymbol{y}^+$ [–]	$\boldsymbol{K}_{\mathbf{rec}}$ [–]	**Difference** [%]
Grid 1	403 840	230	1.120	0.460
Grid 2	808 630	159	1.124	0.167
Grid 3	1 615 180	111	1.126	–

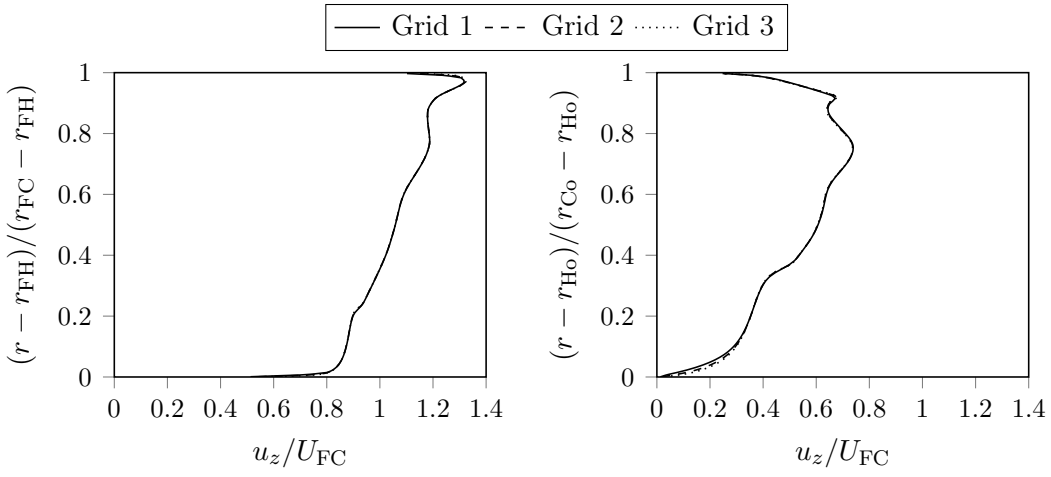

(a) Diffuser inlet (b) Diffuser outlet

Figure C.5: Axial velocity profiles in an annular diffuser with a stator at its inlet for successively refined meshes

C.7 Annular Diffuser with a Stator at its Outlet

The best annular diffuser in Section 6.6 was used to inspect sensitivity to grid refinement. This diffuser has equiangular walls that are 22° from the axial. A stator was added at its outlet to remove the residual swirl in an attempt to recover the circumferential component of dynamic pressure at the diffuser discharge. This time meshes with grid clustering at solid boundaries to facilitate integration through the boundary layer were used for the grid dependence study. The standard k-ω model was used but without wall functions. Residual levels reached 10^{-6} for these computations. Again, the results in Table C.6 and Fig. C.6 demonstrate that grid independence was achieved with Grid 1.

Table C.6: Grid dependence study for an annular diffuser with a stator at its outlet

Grid identifier	**Number of nodes**	**Average y^+** [–]	**K_{rec}** [–]	**Difference** [%]
Grid 1	460 370	0.618	0.951	0.211
Grid 2	869 948	0.625	0.949	–

C.8 Conclusions

This appendix contains the grid dependence studies for the different outlet configurations that were tested for the M-fan. The details of these simulations are briefly outlined, such as mesh specifications, turbulence modelling approach, level of convergence achieved, boundary distances, and diffuser geometries that were selected. The pressure recoveries reported with Grid 1 for the different outlet configurations differed by less than five per cent from the results obtained with the finest meshes. A grid with less than 500 000 nodes is thus capable of resolving the mean flow in every instance if the dump length and radius are kept constant at $l_{\text{dump}} = 10d_{\text{FC}}$ and $r_{\text{dump}} = 5r_{\text{FC}}$, respectively.

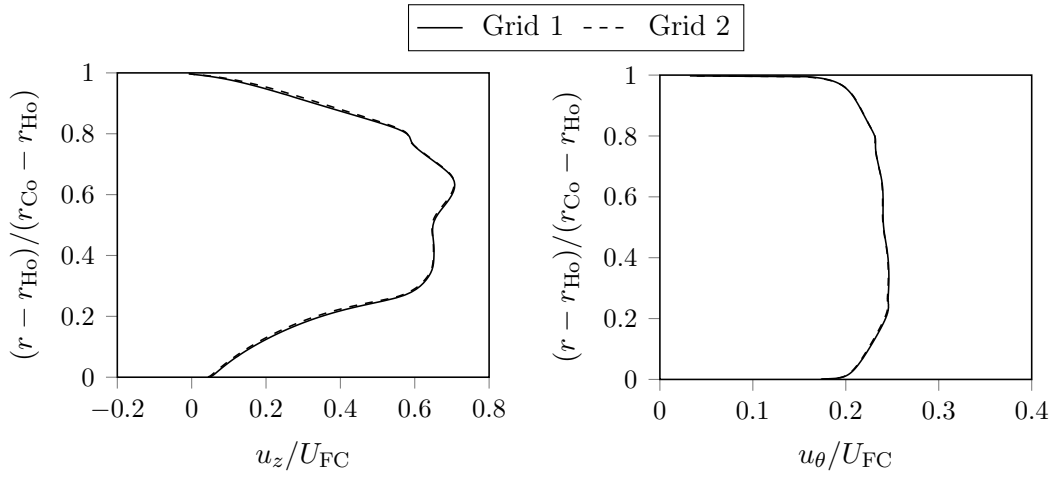

(a) Axial velocity at guide vane inlet

(b) Swirl at guide vane inlet

(c) Axial velocity at guide vane outlet

(d) Swirl at guide vane outlet

Figure C.6: Flow profiles at the inlet (top) and outlet (bottom) of an annular diffuser with a stator at its outlet for successively refined meshes

Appendix D

Boundary Distance Effects

D.1 Introduction

In this appendix, the sensitivity to the location of the dump boundaries is investigated. The dump represents the free discharge to the open atmosphere at the diffuser outlet. The grid dependence studies in Appendix C proved that Grid 1, with less than 500 000 nodes, was capable of resolving the mean flow for the different outlet configurations. Therefore, the mesh density of Grid 1 was maintained for the simulations in this appendix. That is, if the dump got extended, extra grid points were added; if it was shortened, grid points were removed. The same holds for the dump radius. All, except the final outlet configuration, were simulated using the standard k-ω turbulence model with wall functions. The last configuration, i.e. an annular diffuser with a stator at its outlet, also employed the k-ω model but the boundary layer was resolved with a clustered grid so that $y^+ \sim 1$. Boundary distances that do not affect critical results were obtained as follows: The radius of the dump was first held constant while varying its length. Once a dump length that does not affect the pressure recovery coefficient has been found, it was kept constant while changing the dump radius. Once the results stabilised, the solution was deemed independent of the boundary distances.

D.2 Downstream Stator

Figure D.1 depicts how the pressure recovery coefficient varies as the length of the dump, and then the radius of the dump are changed. The pressure recovery coefficient with a dump length of $l_{\text{dump}} = 18d_{\text{FC}}$ varies by less than one per cent compared to the longest dump tested, i.e. $l_{\text{dump}} = 24d_{\text{FC}}$, and was therefore selected. The dump radius was then varied while keeping the length constant at 18 fan diameters. Note that $r_{\text{dump}}/r_{\text{FC}} = 1$ corresponds to a case where a pipe is added after the outlet. In this case, and all the others, it

overestimates the pressure recovery. A dump is thus necessary to accurately model the free discharge to the open atmosphere. The pressure recovery with a dump radius of $r_{\text{dump}} = 13r_{\text{FC}}$ varied by less than one per cent compared to the largest radius tested. Therefore, a dump length and diameter equal to 18 and 13 fan diameters, respectively, were selected.

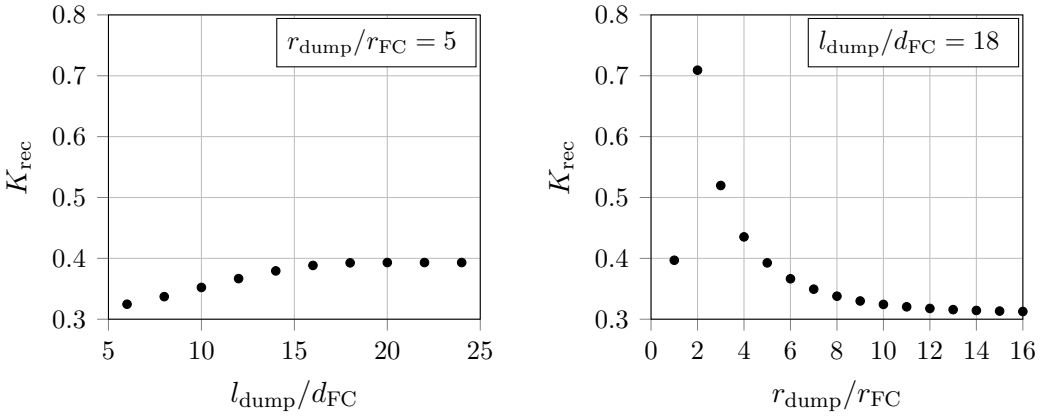

(a) Dump length effects

(b) Dump radius effects

Figure D.1: Effects of dump length and radius on pressure recovery with a downstream stator only

D.3 Conical Diffuser

The sensitivity to boundary distances for a conical diffuser of area ratio 1.792 (or $2\theta = 16°$) is illustrated in Fig. D.2. The results became insensitive to the boundaries when $l_{\text{dump}} = 14d_{\text{FC}}$ and $r_{\text{dump}} = 8r_{\text{difo}}$, where r_{difo} is the radius at the outlet of the diffuser. These dimensions were thus used for the conical diffuser simulations presented in the main body of this document.

D.4 Conical Diffuser with a Stator at its Inlet

For the conical diffuser with a stator between the fan outlet and diffuser inlet, the results in Fig. D.3 were obtained. This was for a conical diffuser with an area ratio of 1.507 (or $2\theta = 10°$). Not such a wide range of dump lengths and diameters were tested as in the previous case since it became apparent that results generally become independent of boundary distances within the ranges of $6 \leq l_{\text{dump}}/d_{\text{FC}} \leq 24$ and $6 \leq r_{\text{dump}}/r_{\text{difo}} \leq 16$. In this case, the pressure recovery coefficients stabilised with $l_{\text{dump}} = 16d_{\text{FC}}$ and $r_{\text{dump}} = 10r_{\text{difo}}$.

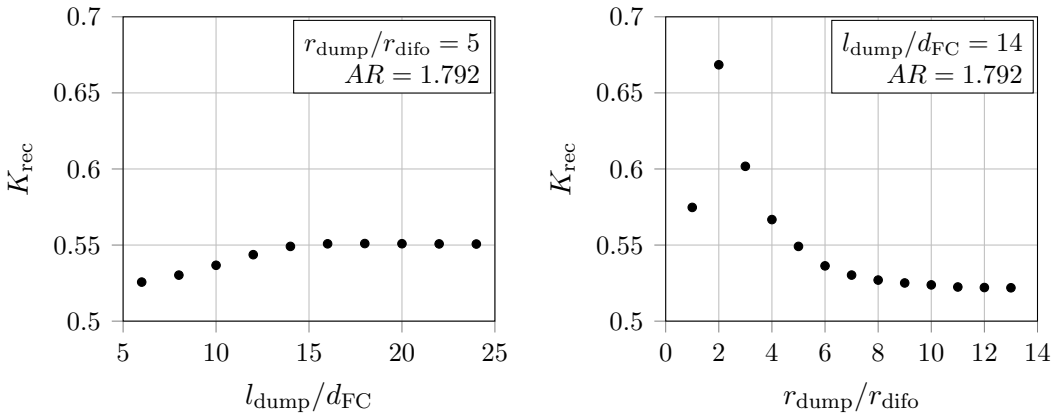

(a) Dump length effects (b) Dump radius effects

Figure D.2: Effects of dump length and radius on pressure recovery for a conical diffuser

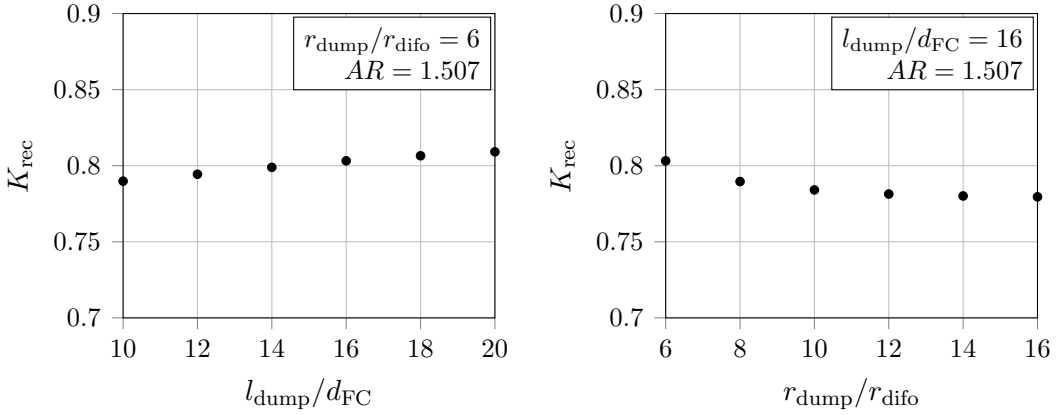

(a) Dump length effects (b) Dump radius effects

Figure D.3: Effects of dump length and radius on pressure recovery for a conical diffuser with a stator at its inlet

D.5 Annular Diffuser

The same annular diffuser that was used for the grid dependence study in Appendix C was used for the boundary distance sensitivity study. The diffuser's length is equal to the fan diameter, the area ratio is 1.936, and the wall angles are $\theta_{\text{H}} = 3.3°$ and $\theta_{\text{C}} = 11.2°$ from the axial. With a dump length equal to 16 fan diameters and dump diameter equal to eight diffuser outlet diameters, the results stabilised. This is evident in Fig. D.4.

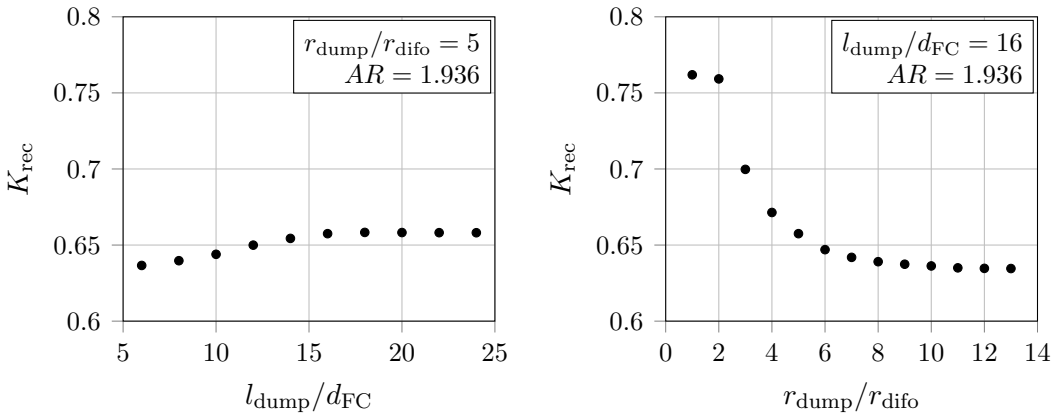

(a) Dump length effects (b) Dump radius effects

Figure D.4: Effects of dump length and radius on pressure recovery for an annular diffuser

D.6 Annular Diffuser with a Stator at its Inlet

The same annular diffuser as in the previous case was used here again. This time, however, a stator was added between the fan outlet and diffuser inlet to remove the swirl before it enters the diffuser. Figure D.5 illustrates that results are not sensitive to the boundary distances within the given range. Even though a shorter dump length produced stable results, a length of $l_{\text{dump}} = 14d_{\text{FC}}$ was used to ensure that the wake downstream of the diffuser discharge has dissipated before it reaches the outlet boundary. This is to make the description of the outlet boundary more representative, i.e. zero gradients for velocity and turbulence quantities. A dump height of $r_{\text{dump}} = 6r_{\text{difo}}$ proved sufficient.

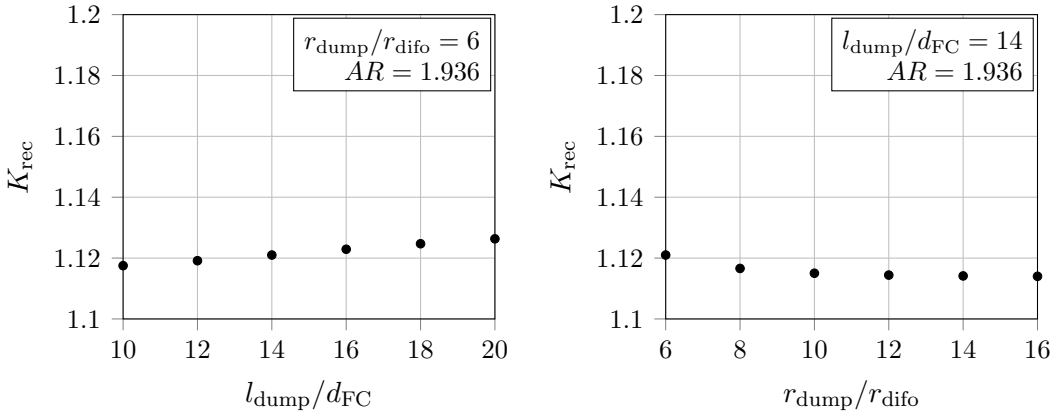

(a) Dump length effects (b) Dump radius effects

Figure D.5: Effects of dump length and radius on pressure recovery for an annular diffuser with a stator at its inlet

D.7 Annular Diffuser with a Stator at its Outlet

The annular diffuser without a stator that produced the highest pressure recovery in Section 6.6 was an equiangular diffuser with wall angles equal to 22° from the axial. In this case, an attempt was made to remove the residual swirl at the outlet of this diffuser by installing a stator at its discharge. The k-ω turbulence model was used with the correct boundary conditions for an integrated boundary layer. The mesh was so that $y^+ \sim 1$ at no-slip boundaries. Figure D.6 illustrates this case's sensitivity to the boundary distances of the dump. Solutions are very insensitive to length variations: The shortest length gave a pressure recovery coefficient within one per cent of the longest dump that was tested. Notwithstanding, a dump length of $l_{\text{dump}} = 14d_{\text{FC}}$ was selected to avoid the wake downstream of the diffuser discharge to reach the outlet boundary. Dump radius variations also had minimal effect on the results. Therefore, the smallest tested radius of $r_{\text{dump}} = 6r_{\text{difo}}$ was selected.

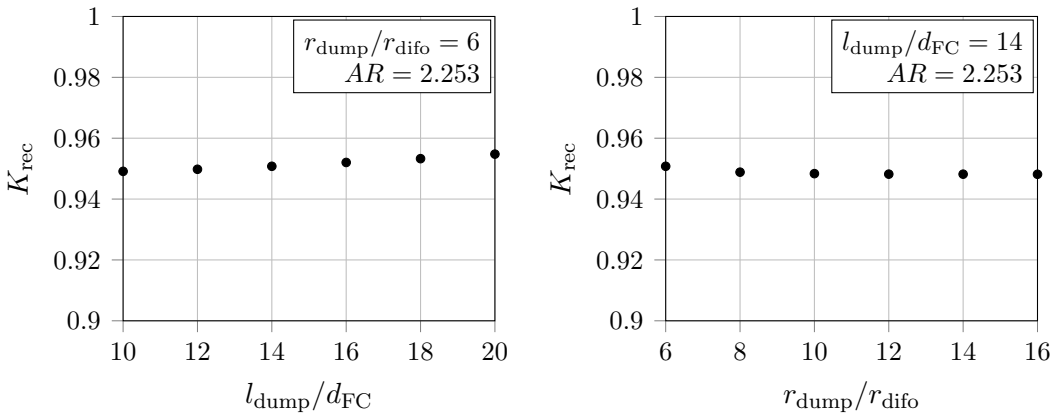

(a) Dump length effects

(b) Dump radius effects

Figure D.6: Effects of dump length and radius on pressure recovery for an annular diffuser with a stator at its outlet

D.8 Conclusions

This appendix investigates the influence the positioning of the dump boundaries has on the pressure recovery results for the various M-fan outlet configurations. A dump length of 14 fan diameters was the minimum length required to produce length-independent solutions; the maximum required length was 18 fan diameters. In some cases, a dump diameter of six diffuser outlet diameters was sufficient, but for others, it needed to be as large as 13 diffuser outlet diameters.

List of References

Adkins, R.C. (1983). A simple method for designing optimum annular diffusers. In: *ASME 1983 International Gas Turbine Conference and Exhibit*, pp. V001T01A020–V001T01A020. American Society of Mechanical Engineers.

Andersson, U. (2009). *An experimental study of the flow in a sharp-heel Kaplan draft tube*. Ph.D. thesis, Department of Applied Physics and Mechanical Engineering, Luleå University of Technology.

Apsley, D.D. and Leschziner, M.A. (1999). Advanced turbulence modelling of separated flow in a diffuser. *Flow, Turbulence and Combustion*, vol. 63, pp. 81–112.

Armfield, S.W., Cho, N.-H. and Fletcher, C.A.J. (1990). Prediction of turbulence quantities for swirling flow in conical diffusers. *AIAA Journal*, vol. 28, no. 3, pp. 453–460.

Armfield, S.W. and Fletcher, C.A.J. (1989). Comparison of k-ε and algebraic Reynolds stress models for swirling diffuser flow. *International Journal for Numerical Methods in Fluids*, vol. 9, no. 8, pp. 987–1009.

Arora, B.B. and Pathak, B.D. (2009). Effect of geometry on the performance of annular diffuser. *International Journal of Applied Engineering Research*, vol. 4, no. 12, pp. 2639–2652.

Blevins, R.D. (1984). *Applied fluid dynamics handbook*. Van Nostrand Reinhold Company, New York. ISBN 978-0-44-221296-4.

Bonous, O. (2008). Studies of the ERCOFTAC conical diffuser with OpenFOAM. Research report 2008:05, Department of Applied Mechanics, Chalmers University of Technology, Göteborg, Sweden.

Bredell, J.R. (2005). *Numerical investigation of fan performance in a forced draft air-cooled steam condenser*. Master's thesis, Department of Mechanical Engineering, Stellenbosch University.

Bredell, J.R., Kröger, D.G. and Thiart, G.D. (2006). Numerical investigation of fan performance in a forced draft air-cooled steam condenser. *Applied Thermal Engineering*, vol. 26, no. 8–9, pp. 846–852.

Bruneau, P.R.P. (1994). *The design of a single rotor axial flow fan for a cooling tower application.* Master's thesis, Department of Mechanical Engineering, Stellenbosch University.

BS 848 (2007). *Industrial fans: Performance testing using standardized airways.* Part 1, British Standards Institution.

Chien, K.-Y. (1982). Predictions of channel and boundary layer flows with a low-Reynolds-number turbulence model. *AIAA Journal*, vol. 20, no. 1, pp. 33–38.

Chieng, C.C. and Launder, B.E. (1980). On the calculation of turbulent heat transport downstream from an abrupt pipe expansion. *Numerical Heat Transfer*, vol. 3, no. 2, pp. 189–207.

Cho, N.-H. and Fletcher, C.A.J. (1991). Computation of turbulent conical diffuser flows using a non-orthogonal grid system. *Computers and Fluids*, vol. 19, no. 3, pp. 347–361.

Clausen, P.D., Koh, S.G. and Wood, D.H. (1993). Measurements of a swirling turbulent boundary layer developing in a conical diffuser. *Experimental Thermal and Fluid Science*, vol. 6, no. 1, pp. 39–48.

Daly, B.J. and Harlow, F.H. (1970). Transport equations in turbulence. *The Physics of Fluids*, vol. 13, no. 11, pp. 2634–2649.

Davidson, L., Nielsen, P.V. and Sveningsson, A. (2003). Modifications of the $\overline{v^2}$-f model for computing the flow in a 3D wall jet. *Turbulence, Heat and Mass Transfer*, vol. 4, pp. 577–584.

Dhiman, S., Foroutan, H. and Yavuzkurt, S. (2011). Simulation of flow through conical diffusers with and without inlet swirl using CFD. In: *Proceedings of ASME-JSME-KSME 2011 Joint Fluids Engineering Conference, Hamamatsu, Japan, 24–29 July*, pp. 1235–1244. American Society of Mechanical Engineers.

Dixon, S.L. and Hall, C.A. (2014). *Fluid mechanics and thermodynamics of turbomachinery.* Seventh edn. Elsevier. ISBN 978-0-12-415954-9.

Donaldson, C.d. (1972). Atmospheric turbulence and the dispersal of atmospheric pollutants. ARAP report no. 175, Aeronautical Research Association of Princeton, Princeton, New Jersey.

Durbin, P.A. (1991). Near-wall turbulence closure modeling without "damping functions". *Theoretical and Computational Fluid Dynamics*, vol. 3, no. 1, pp. 1–13.

Durbin, P.A. (1993). Application of a near-wall turbulence model to boundary layers and heat transfer. *International Journal of Heat and Fluid Flow*, vol. 14, no. 4, pp. 316–323.

Durbin, P.A. (1995). Separated flow computations with the k-ε-v^2 model. *AIAA Journal*, vol. 33, no. 4, pp. 659–664.

Duvenhage, K., Vermeulen, J.A., Meyer, C.J. and Kröger, D.G. (1996). Flow distortions at the fan inlet of forced-draught air-cooled heat exchangers. *Applied Thermal Engineering*, vol. 16, no. 8–9, pp. 741–752.

Eck, B. (1973). *Fans: Design and operation of centrifugal, axial-flow and cross-flow fans*. Pargamon Press Ltd. ISBN 0-08-015872-2.

El-Behery, S.M. and Hamed, M.H. (2011). A comparative study of turbulence models performance for separating flow in a planar asymmetric diffuser. *Computers and Fluids*, vol. 44, no. 1, pp. 248–257.

Enexio (no date). Induced draft air cooled condenser: InAIR—innovative and intelligent [Online]. Retrieved February 14, 2019 from: `https://www.enexio.com/us/products/dry-cooling-systems/air-cooled-condensers/induced-draft-air-cooled-condenser-inair/`.

Engelbrecht, R.A. (2018). *Numerical investigation of fan performance in a forced draft air-cooled condenser*. Ph.D. thesis, Department of Mechanical and Mechatronic Engineering, Stellenbosch University.

From, C.S., Sauret, E., Armfield, S.W., Saha, S.C. and Gu, Y.T. (2017). Turbulent dense gas flow characteristics in swirling conical diffuser. *Computers and Fluids*, vol. 149, pp. 100–118.

Gatski, T.B. and Speziale, C.G. (1993). On explicit algebraic stress models for complex turbulent flows. *Journal of Fluid Mechanics*, vol. 254, pp. 59–78.

Gibson, M.M. and Launder, B.E. (1978). Ground effects on pressure fluctuations in the atmospheric boundary layer. *Journal of Fluid Mechanics*, vol. 86, no. 3, pp. 491–511.

Greenshields, C.J. (2017). *OpenFOAM: User Guide*. 5th edn. OpenFOAM Foundation Ltd.

Gur, O. and Rosen, A. (2005). Propeller performance at low advance ratio. *Journal of Aircraft*, vol. 42, no. 2, pp. 435–441.

Gyllenram, W. and Nilsson, H. (2006). Very large eddy simulation of draft tube flow. In: *23rd IAHR Symposium, Yokohama, Japan*.

Hall, S. (2012). *Rules of Thumb for Chemical Engineers*. 5th edn. Elsevier. ISBN 978-0-12-387785-7.

Hanjalić, K. and Launder, B.E. (1976). Contribution towards a Reynolds-stress closure for low-Reynolds-number turbulence. *Journal of Fluid Mechanics*, vol. 74, no. 4, pp. 593–610.

Harvey, J.K. (1962). Some observations of the vortex breakdown phenomenon. *Journal of Fluid Mechanics*, vol. 14, no. 4, pp. 585–592.

Hill, P.G., Schaub, U.W. and Senoo, Y. (1963). Turbulent wakes in pressure gradients. *Journal of Applied Mechanics*, vol. 30, no. 4, pp. 518–524.

Himmelskamp, H. (1947). *Profile investigations on a rotating airscrew.* Ministry of Aircraft Production.

Hoerner, S.F. (1965). *Fluid-dynamic drag: Practical information on aerodynamic drag and hydrodynamic resistance.* Hoerner Fluid Dynamics.

Hoerner, S.F. and Borst, H.V. (1985). *Fluid-dynamic lift: Practical information on aerodynamic and hydrodynamic lift.* L.A. Hoerner.

Holzmann, T. (2017). *Mathematics, numerics, derivations and OpenFOAM: The basics of numerical simulations.* 4th edn. Holzmann CFD, Leoben.

Hotchkiss, P.J., Meyer, C.J. and Von Backström, T.W. (2006). Numerical investigation into the effect of cross-flow on the performance of axial flow fans in forced draught air-cooled heat exchangers. *Applied Thermal Engineering*, vol. 26, no. 2–3, pp. 200–208.

Howell, A.R. (1945). Fluid dynamics of axial compressors. *Proceedings of the Institution of Mechanical Engineers*, vol. 153, no. 1, pp. 441–452.

Iaccarino, G. (2001). Predictions of a turbulent separated flow using commercial CFD codes. *Journal of Fluids Engineering*, vol. 123, no. 4, pp. 819–828.

Johnson, D.A. and King, L.S. (1985). A mathematically simple turbulence closure model for attached and separated turbulent boundary layers. *AIAA Journal*, vol. 23, no. 11, pp. 1684–1692.

Johnston, I.H. (1953). The effect of inlet conditions on the flow in annular diffusers. Tech. Rep., National Gas Turbine Establishment.

Kalitzin, G., Medic, G., Iaccarino, G. and Durbin, P. (2004). Near-wall behaviour of RANS turbulence models and implications of wall functions. *Journal of Computational Physics*, vol. 204, no. 1, pp. 265–291.

Kim, J.-Y., Ghajar, A.J., Tang, C. and Foutch, G.L. (2005). Comparison of near-wall treatment methods for high Reynolds number backward-facing step flow. *International Journal of Computational Fluid Dynamics*, vol. 19, no. 7, pp. 493–500.

Kim, S.-E. and Choudhury, D. (1995). A near-wall treatment using wall functions sensitized to pressure gradients. In: *Separated and Complex Flows*, vol. 217, pp. 273–280. American Society of Mechanical Engineers.

Kneen, T.H. (1970). Annular diffuser studies with 36 in. axial flow fan rig in exhaust configuration, part 2 (boss ratio 0.5, area ratio of approximately 2). Internal report 76, CSIRO Division of Mechanical Engineering.

Kolmogorov, A.N. (1941). The local structure of turbulence in incompressible viscous fluid for very large Reynolds numbers. *Doklady Akademii Nauk SSSR*, vol. 30, no. 4, pp. 299–303.

Kröger, D.G. (1994). Fan performance in air-cooled steam condensers. *Heat Recovery Systems and CHP*, vol. 14, no. 4, pp. 391–399.

Kröger, D.G. (1998). *Air-cooled heat exchangers and cooling towers: Thermal-flow performance evaluation and design.* Department of Mechanical Engineering, Matieland, South Africa.

Kumar, D.S. and Kumar, K.L. (1980). Effect of swirl on pressure recovery in annular diffusers. *Journal Mechanical Engineering Science*, vol. 22, no. 6, pp. 305–313.

Lai, Y.G., So, R.M.C. and Hwang, B.C. (1989). Calculation of planar and conical diffuser flows. *AIAA Journal*, vol. 27, no. 5, pp. 542–548.

Launder, B.E., Reece, G.J. and Rodi, W. (1975). Progress in the development of a Reynolds-stress turbulence closure. *Journal of Fluid Mechanics*, vol. 68, no. 3, pp. 537–566.

Launder, B.E. and Sharma, B.I. (1974). Application of the energy-dissipation model of turbulence to the calculation of flow near a spinning disc. *Letters In Heat and Mass Transfer*, vol. 1, no. 2, pp. 131–138.

Launder, B.E. and Spalding, D.B. (1974). The numerical computation of turbulent flows. *Computer Methods in Applied Mechanics and Engineering*, vol. 3, no. 2, pp. 269–289.

Lee, J., Jang, S.J. and Sung, H.J. (2012). Direct numerical simulations of turbulent flow in a conical diffuser. *Journal of Turbulence*, vol. 13, no. 30, pp. 1–29.

Lien, F.S., Chen, W.L. and Leschziner, M.A. (1996). Low-Reynolds-number eddy-viscosity modelling based on non-linear stress-strain/vorticity relations. In: *Engineering Turbulence Modelling and Experiments 3*, pp. 91–100. Elsevier.

Lien, F.-S. and Kalitzin, G. (2001). Computations of transonic flow with the v^2-f turbulence model. *International Journal of Heat and Fluid Flow*, vol. 22, no. 1, pp. 53–61.

Liu, F. (2016). A thorough description of how wall functions are implemented in OpenFOAM. In: *Proceedings of CFD with OpenSource Software.*

Louw, F.G. (2015). *Investigation of the flow field in the vicinity of an axial flow fan during low flow rates.* Ph.D. thesis, Department of Mechanical and Mechatronic Engineering, Stellenbosch University.

Louw, F.G., Bruneau, P.R.P., von Backström, T.W. and Van der Spuy, S.J. (2012). The design of an axial flow fan for application in large air-cooled heat exchangers. In: *ASME Turbo Expo 2012: Turbomachinery Technical Conference and Exposition*, pp. 771–785. American Society of Mechanical Engineers.

Lumley, J.L. (1979). Computational modeling of turbulent flows. *Advances in Applied Mechanics*, vol. 18, pp. 123–176.

Marks, L.S. and Weske, J.R. (1934). The design and performance of an axial-flow fan. *Transactions of the American Society of Mechanical Engineers*, vol. 56, no. 13, pp. 807–813.

McDonald, A.T. and Fox, R.W. (1966). An experimental investigation of incompressible flow in conical diffusers. *International Journal of Mechanical Sciences*, vol. 8, no. 2, pp. 125–139.

McDonald, A.T., Fox, R.W. and Van Dewoestine, R.V. (1971). Effects of swirling inlet flow on pressure recovery in conical diffusers. *AAIA Journal*, vol. 9, no. 10, pp. 2014–2018.

McGhee, R.J. and Beasley, W.D. (1979). Low-speed aerodynamic characteristics of a 13-percent-thick medium-speed airfoil designed for general aviation applications. NASA technical paper 1498, Langley Research Center, Hampton, Virginia.

McKenzie, A.B. (1997). *Axial flow fans and compressors: Aerodynamic design and performance*. Ashgate Publishing Ltd., New York 13, N.Y. ISBN 0-29139-850-2.

Menter, F.R. (1992). Influence of freestream values on k-ω turbulence model predictions. *AIAA Journal*, vol. 30, no. 6, pp. 1657–1659.

Menter, F.R. (1994). Two-equation eddy-viscosity turbulence models for engineering applications. *AIAA Journal*, vol. 32, no. 8, pp. 1598–1605.

Meyer, C.J. (2000). *A numerical investigation of the plenum chamber aerodynamic behaviour of mechanical draught air-cooled heat exchangers*. Ph.D. thesis, Department of Mechanical Engineering, Stellenbosch University.

Meyer, C.J. (2005). Numerical investigation of the effect of inlet flow distortions on forced draught air-cooled heat exchanger performance. *Applied Thermal Engineering*, vol. 25, no. 11–12, pp. 1634–1649.

Meyer, C.J. and Kröger, D.G. (1998). Plenum chamber flow losses in forced draught air-cooled heat exchangers. *Applied Thermal Engineering*, vol. 18, no. 9, pp. 875–893.

Meyer, C.J. and Kröger, D.G. (2001). Numerical simulation of the flow field in the vicinity of an axial flow fan. *International Journal for Numerical Methods in Fluids*, vol. 36, no. 8, pp. 947–969.

Meyer, C.J. and Kröger, D.G. (2004). Numerical investigation of the effect of fan performance on forced draught air-cooled heat exchanger plenum chamber aerodynamic behaviour. *Applied Thermal Engineering*, vol. 24, no. 2, pp. 359–371.

Miller, D.S. (1971). *Internal flow: A guide to losses in pipe and duct systems*. BHRA Fluid Engineering.

Miller, D.S. (1978). *Internal flow systems.* BHRA Fluid Engineering. ISBN 0-900983-78-7.

Mohan, R., Singh, S.N. and Agrawal, D.P. (1998). Optimum inlet swirl for annular diffuser performance using CFD. *Indian Journal of Engineering and Materials Science*, vol. 5, no. 1, pp. 15–21.

Monroe, R.C. (1978). Improving cooling tower fan system efficiencies. In: *Proceedings of the Seventh Turbomachinery Symposium*, pp. 159–166. Texas A&M University. Gas Turbine Laboratories.

Moore, J., Grimes, R., O'Donovan, A. and Walsh, E. (2014). Design and testing of a novel air-cooled condenser for concentrated solar power plants. *Energy Procedia*, vol. 49, pp. 1439–1449.

Munisamy, K.M., Govindasamy, R. and Thangaraju, S.K. (2015). Experimental investigation on design enhancement of axial fan using fixed guide vane. In: *IOP Conference Series: Materials Science and Engineering*, vol. 88. IOP Publishing.

Neve, R.S. and Wirasinghe, N.E.A. (1978). Changes in conical diffuser performance by swirl addition. *The Aeronautical Quarterly*, vol. 29, no. 3, pp. 131–143.

Nilsson, H. and Davidson, L. (2001). A numerical investigation of the flow in the wicket gate and runner of the Hölleforsen (Turbine 99) Kaplan turbine model. In: *Proceedings of Turbine 99-II.*

Nilsson, H., Page, M., Beaudoin, M., Gschaider, B. and Jasak, H. (2008). The OpenFOAM turbomachinery working-group, and conclusions from the turbomachinery session of the third OpenFOAM workshop. In: *IAHR: 24th Symposium on Hydraulic Machinery and Systems, Foz do Iguassu, Brazil, 27–31 October.*

Obi, S., Aoki, K. and Masuda, S. (1993). Experimental and computational study of turbulent separating flow in an asymmetric plane diffuser. In: *Ninth Symposium on "Turbulent Shear Flows", Kyoto, Japan.*

Okhio, C.B., Horton, H.P. and Langer, G. (1983). Effects of swirl on flow separation and performance of wide angle diffusers. *International Journal of Heat and Fluid Flow*, vol. 4, no. 4, pp. 199–206.

Patel, V.C., Rodi, W. and Scheuerer, G. (1985). Turbulence models for near-wall and low Reynolds number flows: a review. *AIAA Journal*, vol. 23, no. 9, pp. 1308–1319.

Peters, H. (1934). Conversion of energy in cross-sectional divergences under different conditions of inflow. Technical memorandum 737, National Advisory Committee for Aeronautics.

Raj, R. and Lakshminarayana, B. (1973). Characteristics of the wake behind a cascade of airfoils. *Journal of Fluid Mechanics*, vol. 61, no. 4, pp. 707–730.

Reynolds, O. (1895). On the dynamical theory of incompressible viscous fluids and the determination of the criterion. *Philosophical Transactions of the Royal Society of London. A*, vol. 186, pp. 123–164.

Rodi, W. (1976). A new algebraic relation for calculating the Reynolds stresses. In: *Gesellschaft Angewandte Mathematik und Mechanik Workshop, Paris, France*, vol. 56.

Rodi, W., Bonnin, J.C. and Buchal, T. (1995). ERCOFTAC workshop on data bases and testing of calculation methods for turbulent flows. In: *Fourth ERCOFTAC/IAHR Workshop on Refined Flow Modelling, Karlsruhe, Germany, April 3–7.*

Russell, B.A. and Wallis, R.A. (1969). A note on annular diffuser design, axial flow fans. Internal report 63, CSIRO Division of Mechanical Engineering.

Salta, C.A. and Kröger, D.G. (1995). Effect of inlet flow distortions on fan performance in forced draught air-cooled heat exchangers. *Heat Recovery Systems and CHP*, vol. 15, no. 6, pp. 555–561.

Senoo, Y., Kawaguchi, N. and Nagata, T. (1978). Swirl flow in conical diffusers. *Bulletin of JSME*, vol. 21, no. 151, pp. 112–119.

Shepherd, I.C. (1974). Annular exhaust diffusers for axial flow fans. In: *Fifth Australasian Conference on Hydraulics and Fluid Mechanics, Christchurch, New Zealand*, pp. 74–81.

Sherras, B.R. (1980). *An investigation of the 'G' parameter for design of annular diffusers.* Master's thesis, School of Mechanical Engineering, Cranfield Institution of Technology.

Shih, T.-H., Liou, W.W., Shabbir, A., Yang, Z. and Zhu, J. (1995). The new k-ε eddy viscosity model for high Reynolds number turbulent flows. *Computers and Fluids*, vol. 24, no. 3, pp. 227–238.

Shih, T.-H., Zhu, J. and Lumley, J.L. (1993). A realizable Reynolds stress algebraic equation model. NASA technical memorandum 105993, NASA Lewis Research Center, Cleveland, OH, United States.

Singh, S.N., Agrawal, D.P., Sapre, R.N. and Malhotra, R.C. (1994). Effect of inlet swirl on the performance of wide-angled annular diffusers. *Indian Journal of Engineering and Materials Science*, vol. 1, pp. 63–69.

Singh, S.N., Seshadri, V., Saha, K., Vempati, K.K. and Bharani, S. (2006). Effect of inlet swirl on the performance of annular diffusers having the same equivalent cone angle. In: *Proceedings of the Institution of Mechanical Engineers, Part G, Journal of Aerospace Engineering*, vol. 220, pp. 129–143.

So, K.L. (1967). Vortex phenomena in a conical diffuser. *AIAA Journal*, vol. 5, no. 6, pp. 1072–1078.

Sovran, G. and Klomp, E.D. (1967). Experimentally determined optimum geometries for rectilinear diffusers with rectangular, conical or annular cross-section. In: *Fluid mechanics of internal flow*, pp. 270–319. Elsevier.

Spalart, P.R. and Allmaras, S.R. (1992). A one-equation turbulence model for aerodynamic flows. In: *AIAA 30th Aerospace Sciences Meeting and Exhibit, Reno, NV, U.S.A.*

Speziale, C.G. (1987). On nonlinear k-ℓ and k-ε models of turbulence. *Journal of Fluid Mechanics*, vol. 178, pp. 459–475.

Speziale, C.G., Sarkar, S. and Gatski, T.B. (1991). Modelling the pressure-strain correlation of turbulence: An invariant dynamical systems approach. *Journal of Fluid Mechanics*, vol. 227, pp. 245–272.

Stewart, S.F.C., Hariharan, P., Paterson, E.G., Burgreen, G.W., Reddy, V., Day, S.W., Giarra, M., Manning, K.B., Deutsch, S., Berman, M.R., Myers, M.R. and Malinauskas, R.A. (2013). Results of FDA's first interlaboratory computational study of a nozzle with a sudden contraction and conical diffuser. *Cardiovascular Engineering and Technology*, vol. 4, no. 4, pp. 374–391.

Stinnes, W.H. (1998). *The performance of axial fans subjected to forced cross-flow at inlet.* Master's thesis, Department of Mechanical Engineering, Stellenbosch University.

Stinnes, W.H. and Von Backström, T.W. (2002). Effect of cross-flow on the performance of air-cooled heat exchanger fans. *Applied Thermal Engineering*, vol. 22, no. 12, pp. 1403–1415.

Terzis, A., Stylianou, I., Kalfas, A.I. and Ott, P. (2012). Heat transfer and performance characteristics of axial cooling fans with downstream guide vanes. *Journal of Thermal Science*, vol. 21, no. 2, pp. 162–171.

Thiart, G.D. and Von Backström, T.W. (1993). Numerical simulation of the flow field near an axial flow fan operating under distorted inflow conditions. *Journal of Wind Engineering and Industrial Aerodynamics*, vol. 45, no. 2, pp. 189–214.

Van der Spuy, S.J. (1997). *The design of a low-noise rotor-only axial flow fan series.* Master's thesis, Department of Mechanical Engineering, Stellenbosch University.

Van der Spuy, S.J. (2011). *Perimeter fan performance in forced draught air-cooled steam condensers.* Ph.D. thesis, Department of Mechanical and Mechatronic Engineering, Stellenbosch University.

Van Rooyen, J.A. and Kröger, D.G. (2008). Performance trends of an air-cooled steam condenser under windy conditions. *Journal of Engineering for Gas Turbines and Power*, vol. 130, no. 2.

Versteeg, H.K. and Malalasekera, W. (2007). *An introduction to computational fluid dynamics: The finite volume method.* 2nd edn. Pearson Education Limited. ISBN 978-0-13-127498-3.

Von Backström, T.W., Buys, J.D. and Stinnes, W.H. (1996). Minimization of the exit loss of a rotor-only axial fan. *Engineering Optimization*, vol. 26, no. 1, pp. 25–33.

Wallin, S. and Johansson, A. (2000). An explicit algebraic Reynolds stress model for incompressible and compressible turbulent flows. *Journal of Fluid Mechanics*, vol. 403, pp. 89–132.

Wallis, R.A. (1975). Annular diffusers of radius ratio 0.5 for axial flow fans. Internal report 4, CSIRO Division of Mechanical Engineering.

Wallis, R.A. (1983). *Axial flow fans and ducts.* John Wiley & Sons, Inc. ISBN 0-471-87086-2.

Walter, J., Caglar, S. and Gabi, M. (2018). Investigation of the maximum static efficiency of axial fans. In: *International Conference of Fan Noise, Aerodynamics, Applications and Systems, Darmstadt, Germany.*

Wilcox, D.C. (1988). Reassessment of the scale-determining equation for advanced turbulence models. *AIAA Journal*, vol. 26, no. 11, pp. 1299–1310.

Wilcox, D.C. (1993). Comparison of two-equation turbulence models for boundary layers with pressure gradient. *AIAA Journal*, vol. 31, no. 8, pp. 1414–1421.

Wilcox, D.C. (1998). *Turbulence Modeling for CFD.* 2nd edn. DCW Industries. ISBN 0-9636051-5-1.

Wilkinson, M.B. (2017). *The design of an axial flow fan for air-cooled heat exchanger applications.* Master's thesis, Department of Mechanical and Mechatronic Engineering, Stellenbosch University.

Wilkinson, M.B., Van der Spuy, S.J. and Von Backström, T.W. (2017). The design of a large diameter axial flow fan for air-cooled heat exchanger applications. In: *ASME Turbo Expo 2017: Turbomachinery Technical Conference and Exposition*, pp. V001T09A002–V001T09A002. American Society of Mechanical Engineers.

Wilkinson, M.B., Van der Spuy, S.J. and Von Backström, T.W. (2018). Performance testing of an axial flow fan designed for air-cooled heat exchanger applications. In: *ASME Turbo Expo 2018: Turbomachinery Technical Conference and Exposition*, pp. V001T09A005–V001T09A005. American Society of Mechanical Engineers.

Wolfshtein, M. (1969). The velocity and temperature distribution in one-dimensional flow with turbulence augmentation and pressure gradient. *International Journal of Heat and Mass Transfer*, vol. 12, no. 3, pp. 301–318.

Wright, J.R., Russell, B.A. and Wallis, R.A. (1970). Annular diffuser studies with 36 in. axial flow fan rig in exhaust configuration, (boss ratio 0.5, area ratios 3.5 and 1.33). Internal report 71, CSIRO Division of Mechanical Engineering.

Yakhot, V., Orszag, S.A., Thangam, S., Gatski, T.B. and Speziale, C.G. (1992). Development of turbulence models for shear flows by a double expansion technique. *Physics of Fluids A: Fluid Dynamics*, vol. 4, no. 7, pp. 1510–1520.